NAVAL POSTGRADUATE SCHOOL

MONTEREY, CALIFORNIA

THESIS

MODELING AND SIMULATION OF A DUAL-JUNCTION CIGS SOLAR CELL USING SILVACO ATLAS

by

Konstantinos Fotis

December 2012

Thesis Advisor:	Sherif Michael
Second Reader:	Todd Weatherford

Approved for public release; distribution is unlimited

THIS PAGE INTENTIONALLY LEFT BLANK

REPORT DOCUMENTATION PAGE			Form Approved OMB No. 0704–0188

1. AGENCY USE ONLY *(Leave blank)*	2. REPORT DATE December 2012	3. REPORT TYPE AND DATES COVERED Master's Thesis

4. TITLE AND SUBTITLE MODELING AND SIMULATION OF A DUAL-JUNCTION CIGS SOLAR CELL USING SILVACO ATLAS	5. FUNDING NUMBERS
6. AUTHOR(S) Konstantinos Fotis	
7. PERFORMING ORGANIZATION NAME(S) AND ADDRESS(ES) Naval Postgraduate School Monterey, CA 93943–5000	8. PERFORMING ORGANIZATION REPORT NUMBER
9. SPONSORING /MONITORING AGENCY NAME(S) AND ADDRESS(ES) N/A	10. SPONSORING/MONITORING AGENCY REPORT NUMBER

11. SUPPLEMENTARY NOTES The views expressed in this thesis are those of the author and do not reflect the official policy or position of the Department of Defense or the U.S. Government. IRB Protocol number ____N/A____.

12a. DISTRIBUTION / AVAILABILITY STATEMENT Approved for public release; distribution is unlimited	12b. DISTRIBUTION CODE

13. ABSTRACT (maximum 200 words)

The potential of designing a dual-junction Copper Indium Gallium Selenide (CIGS) photovoltaic cell is investigated in this thesis. Research into implementing a dual-junction solar cell, using a CIGS bottom cell and different thin-film designs as a top cell, was conducted in order to increase the current record efficiency of 20.3% for a single CIGS cell. This was accomplished through modeling and simulation using Silvaco ATLAS™, an advanced virtual wafer-fabrication tool. A Silvaco ATLAS™ model of a single CIGS cell was created by utilizing actual solar cell parameters (such as layer thicknesses, gallium ratio, doping levels and materials properties) documented in different papers, and work from previous NPS theses provided the background for modeling with Silvaco ATLAS™. After the individual CIGS solar cells were built, a dual-junction cell was created by adding the layers of another CIGS solar cell whose parameters (layers thicknesses, Ga ratio) were varied to produce an optimum efficiency of 24%. This approach is promising to produce a multi-junction CIGS cell with record efficiency.

14. SUBJECT TERMS Solar Cell, CIGS, Photovoltaic, Multi-junction, Silvaco, Atlas, I-V Curve, Modeling, Simulation, Development.	15. NUMBER OF PAGES 118
	16. PRICE CODE

17. SECURITY CLASSIFICATION OF REPORT	18. SECURITY CLASSIFICATION OF THIS PAGE	19. SECURITY CLASSIFICATION OF ABSTRACT	20. LIMITATION OF ABSTRACT
Unclassified	Unclassified	Unclassified	UU

THIS PAGE INTENTIONALLY LEFT BLANK

Approved for public release; distribution is unlimited

MODELING AND SIMULATION OF A DUAL-JUNCTION CIGS SOLAR CELL USING SILVACO ATLAS

Konstantinos Fotis
Lieutenant, Hellenic Navy
B.S., Hellenic Naval Academy, 2003

Submitted in partial fulfillment of the
requirements for the degree of

ELECTRICAL ENGINEER
and
MASTER OF SCIENCE IN ELECTRICAL ENGINEERING

from the

NAVAL POSTGRADUATE SCHOOL
December 2012

Author: Konstantinos Fotis

Approved by: Sherif Michael
Thesis Advisor

Todd Weatherford
Second Reader

Clark Robertson
Chair, Department of Electrical and Computer Engineering

THIS PAGE INTENTIONALLY LEFT BLANK

ABSTRACT

The potential of designing a dual-junction Copper Indium Gallium Selenide (CIGS) photovoltaic cell is investigated in this thesis. Research into implementing a dual-junction solar cell, using a CIGS bottom cell and different thin-film designs as a top cell, was conducted in order to increase the current record efficiency of 20.3% for a single CIGS cell. This was accomplished through modeling and simulation using Silvaco ATLAS™, an advanced virtual wafer-fabrication tool. A Silvaco ATLAS™ model of a single CIGS cell was created by utilizing actual solar cell parameters (such as layer thicknesses, gallium ratio, doping levels and materials properties) documented in different papers, and work from previous NPS theses provided the background for modeling with Silvaco ATLAS™. After the individual CIGS solar cells were built, a dual-junction cell was created by adding the layers of another CIGS solar cell whose parameters (layers thicknesses, Ga ratio) were varied to produce an optimum efficiency of 24%. This approach is promising to produce a multi-junction CIGS cell with record efficiency.

THIS PAGE INTENTIONALLY LEFT BLANK

TABLE OF CONTENTS

LIST OF FIGURES

LIST OF TABLES

THIS PAGE INTENTIONALLY LEFT BLANK

LIST OF ACRONYMS AND ABBREVIATIONS

CGS	Copper Gallium Selenide, $CuGaSe_2$
CIGS	Copper Indium Gallium Selenide, $Cu(In,Ga)Se_2$
CIS	Copper Indium Selenide, $CuInSe_2$
CVD	Chemical Vapor Deposition
IGO	Indium-Gallium Oxide
ITO	Indium-Tin Oxide
PECVD	Plasma-Enhanced Chemical Vapor Deposition
PLD	Pulsed Laser Deposition
PV	Photovoltaic
PVD	Physical Vapor Deposition
TCO	Transparent Conducting Oxide
TFSC	Thin-Film Solar Cell

THIS PAGE INTENTIONALLY LEFT BLANK

EXECUTIVE SUMMARY

The intensive use of fossil fuels and nuclear power in recent years is largely responsible for the serious environmental problems facing our planet, which have a direct impact on climate change, and generally, on living conditions. The only answer for the moment that seems able to reduce environmental problems drastically is the use of renewable energy sources which represent energies friendly to the environment, with little or no impact. Among the various renewable-energy sources, the most promising and rapidly growing is based on the conversion of solar energy into electricity through the photovoltaic effect.

Photovoltaic systems have no pollution, are easy to install, and are long lasting while the cost of maintenance and operation are minimal. Therefore, they can be adapted and used in a wide range of applications. An important factor in solar cell evolution is to reduce production costs and increase efficiency, which can be achieved with the use of new materials and technologies.

Thin-film solar cell (TFSC) technology is expected to dramatically reduce the cost of solar cell production, having already achieved performance comparable to that of conventional silicon technology. All thin-film photovoltaic (PV) technologies, regardless of the material used, have important advantages such as low consumption of the active medium, low production cost, and independence from dwindling sources of silicon, fewer material-processing steps, and the flexibility to meet special demands.

Among TFSC, the Copper Indium Gallium Selenide, $Cu(In,Ga)Se_2$, (CIGS) photovoltaic cell has a preeminent pace both in the current PV industry and at the research level. Such cells have already achieved high efficiencies of 20% and are attractive for use in PV technology because of their band gap, which has a value near optimal and the broad choice of heterojunctive partners available, allowing additional degrees of freedom for optimizing performance. The extensive study of CIGS to date has revealed many of their properties and characteristics. The most important are the thickness of the cell, which is flexible, resulting in cost reduction because of the use of less material and their tunable energy-gap, which enables the efficient exploitation of

different parts of the solar spectrum. A thorough study and understanding of their properties and function promises their use in denominated tandem, triple, and multi-junction solar cells, in which layers with different band gaps exploit different energy regions of the solar spectrum, yielding the highest record efficiencies among PV cells to date.

In this context, various efforts have been made to study and simulate experimental and actual cells. Modeling and simulation of a cupper gallium selenide (CGS)/CIGS tandem solar cell has shown an efficiency of 25% and for a CdZnTe/CIGS cell, 26%. Modeling of a low-cost, organic–inorganic hybrid tandem PV cell to achieve efficiencies exceeding 20% has also been proposed. A CIGS-based material developed by doping CIGS with a moderate amount of aluminum (CIAGS) is shown to increase band gap up to 1.5 eV. The development of mechanically stacked and monolithically integrated tandem cells, using a bottom CIGS cell and a top dye-sensitizer solar cell (DSC), as well different methods to increase the transmittivity of the top cell, have also been studied. Moreover, an open-circuit voltage of 1.5 V was achieved with the fabrication of a mechanical stacked tandem device with an $Ag(In,Ga)Se_2$ (AIGS) top cell and a CIGS bottom cell. The potential of designing and simulating a dual-junction CIGS photovoltaic cell using Silvaco ATLAS was investigated in this thesis.

Different CIGS cell typical parameters documented in various papers were utilized to create a Silvaco ATLAS model of a single CIGS cell. Modifications were then made to the thickness and $Ga/(In+Ga)$ mole fraction to simulate two different CIGS cells in order to achieve those characteristics that would allow their use as a dual-junction PV cell. After the individual CIGS solar cells were built and the current matching between them was confirmed and tested, a dual-junction cell was created by adding the layers of these two CIGS solar cells. The overall efficiency of this device was found to be 24%.

ACKNOWLEDGMENTS

I would like to express my gratitude and sincere appreciation to Professor Sherif Michael for his guidance, encouragement and support in order to complete this work. I would like to thank Professor Todd Weatherford for his time spent serving as the second reader of this thesis. I would also like to thank Research Associate Matthew Porter for his expertise with Silvaco ATLAS and his help to troubleshooting the program.

I would like to thank a former graduate student of the Naval Postgraduate School, LT Charalampo Katsaro, Hellenic Navy, for the final push he gave me to become a graduate student and live one of the best experiences of my life so far. Finally, I would like to thank my family for their support and encouragement during my studies.

THIS PAGE INTENTIONALLY LEFT BLANK

I. INTRODUCTION

One of the major problems of today is the limited availability of fossil fuels and hydrocarbons and the consequences of increasing consumption on the environment, quality of life, and human health. For these reasons, it is imperative to shift to other energy sources. Renewable energy is one answer to this problem, and one of the most prevalent forms is solar. Through photovoltaic (PV) technology, solar energy becomes available and widely exploitable.

Today PV technology is experiencing significant growth and development and, as a source of electric energy, is considered sufficiently reliable. The operation and maintenance of PV power plants has a very low cost, and the operation of these systems is silent since they have no moving parts. Most important, PV technology does not produce air pollution. These plants can be installed quickly and adjusted easily to direct the power supply to the necessary points without the need for transmission lines. There are many applications in various installations already, often supplying energy in places where it would be impossible to provide power otherwise. The social, economic and environmental benefits are evident for a number of local communities.

The current market in PV panels is dominated by Si cells that, despite their high efficiency, are costly to construct because of the large thickness of the cell that is required and because Si crystals are expensive and slow growing. It is assumed that PV technology will continue to improve in efficiency and economic issues, and in this direction lies the effort of all manufacturers today. One promising alternative is the use of thin-film solar cells (TFSC) such as the Copper Indium Gallium Selenide, $Cu(In,Ga)Se_2$, (CIGS). Despite their lower cost of production, due to reduced thickness, (up to a hundred times thinner than Si cells), generally TFSC lack in performance and have a much less developed knowledge and technology base as compared to Si. CIGS solar cells with a band gap of 1.2~1.3 eV have reached the performance of polycrystalline Si with a record efficiency of 20.3%. An increase in efficiency is expected mainly using denominated tandem, triple, and multi-junction solar cells, consisting of layers with different band gaps in order to utilize different energy regions of the solar spectrum. In

this context, several researches are trying to fabricate reliable cells with wide band gaps in order to use them as a top cell. A CIGS-based material developed by doping CIGS with moderate amount of aluminum (CIAGS) is shown to increase the band gap to 1.5 eV [1]. Synthesis and physical properties of CIGS nanoparticles and $CuGaSe_2$ (CGS) thin-films for tandem cell PV applications show that the optical band gap of the nanoparticles is increased when they grow at high temperature [2]. Furthermore, modeling and simulation of a CGS/CIGS tandem solar cell has shown an efficiency of 25% [3] and for a CdZnTe/CIGS cell, 26% [4]. Modeling of a low-cost organic–inorganic hybrid tandem PV cell to achieve efficiencies exceeding 20% have also been proposed [5]. The development of mechanically stacked and monolithically integrated tandem cells, using a bottom CIGS cell and a top dye-sensitizer solar cell (DSC), as well different methods to increase the transmittivity of the top cell, have also been studied [6]. Moreover, the fabrication of mechanical stacked tandem device with an $Ag(In,Ga)Se_2$ (AIGS) top cell and a CIGS bottom cell show an open-circuit voltage of 1.5 V [7]. Within this context, the potential of designing a dual-junction CIGS cell to improve and boost the efficiency of a single CIGS cell is the aim of this thesis.

A background of semiconductor physics and p-n junctions is discussed in Chapter II. An overview on solar cells is provided in Chapter III. An introduction of thin CIGS films is given in Chapter IV. An outline of the Silvaco ATLAS modeling and simulation software used to model a dual-junction CIGS solar cell is provided in Chapter V. The approach used for this thesis and the results obtained are shown and discussed in Chapter VI. Conclusions and an outline for future work are noted in Chapter VII. The ATLAS source code used to simulate the CIGS solar cells and the dual-junction CIGS solar cells are provided in Appendix A. The MATLAB code used to generate the overall current-voltage characteristics of the dual-junction CIGS cell is given in Appendix B.

II. SEMICONDUCTOR PHYSICS

A. ENERGY BANDS AND ENERGY GAP

Electrons in the atoms of crystalline solids can exist only in well-defined energy bands. If a semiconductor absorbs a significant amount of energy in the form of heat or radiation for example, when at ordinary environmental temperature, thermal energy is transferred to the atoms and causes the release of electrons from their bonds. The freed electrons are removed from the area of the bond by means of the kinetic energy obtained from the heat and become agile bodies of electricity, giving the semiconductor a remarkable electrical conductivity. The weakening of the bonds in the grid does not imply the collapse of the body's cohesion, since the remaining chemical bonds with the imperfect bond are sufficient to retain the atoms in position. The conduction electrons, the free electrons, move irregularly into the body as long as they maintain their increased energy. If this energy is significantly reduced, they return to the vacant position of an incomplete bond. The coverage of the vacancy can also be done by an adjacent electron, which leaves a vacancy in its initial atom. The shifting of these vacancies can be represented by a virtual particle, a "hole," which theoretically has the same mass and opposite charge of the electron. In terms of energy, the electrons are divided into three categories. The electrons of internal layers, which are less active and not involved in the formation of chemical bonds; valence electrons, which form the bonds; and free conduction band electrons. The energy levels of valence electrons form an energy band, the valence band, and correspondingly, the conduction electrons' energy levels form the conduction band. The energy distance between the two bands, that is, the difference between the energy of the lowest energy conduction band electrons and the highest energy valence band electrons is called the band gap and signifies the minimum energy required to excite a valence electron to turn into a conduction electron while creating a hole. Schematically, this phenomenon is shown in Figure 1.

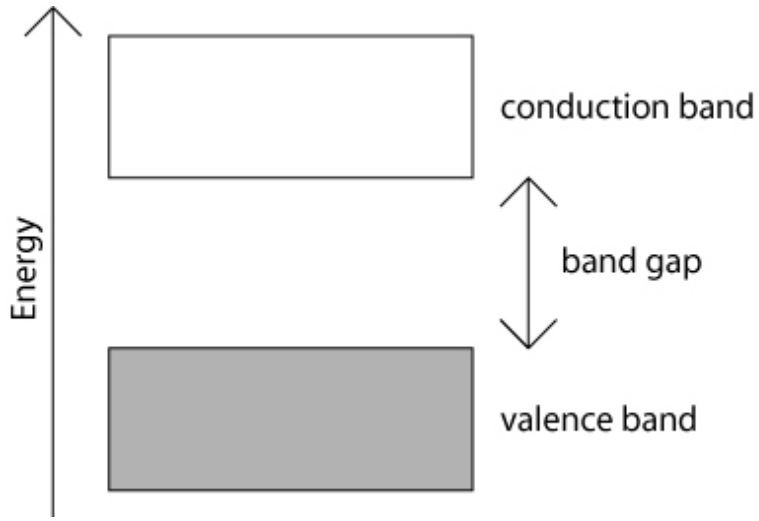

Figure 1. Simplified representation of semiconductor energy levels.

In a completely pure semiconductor, with no impurities and a perfect crystal lattice, there are no energy levels in the gap between the valence band E_V and conduction band E_C, and this region forms a forbidden energy band. The energy required for an electron to transition from the valence band to the conduction band is defined as the band gap energy E_g and has units of electron volts (eV). The excitation of a valence electron can be achieved when an amount of energy is offered, as in a beam of irradiation with photons of energy

$$E = hv \tag{2.1}$$

where h is Planck's constant ($4.135 \cdot 10^{-15}$ eVs) and v is the frequency of its associated electromagnetic wave (Hz).

If the photons' energy is less than the element's band gap energy, the excited electron cannot attain the higher state. If the incident photons have energy greater than the band gap energy, the electron leaves the covalent bond, and the energy is converted into kinetic energy, which is perceived as an increase in the temperature of the material. The probability of the valence electrons' obtaining enough energy from the environment to be stimulated sufficiently to overcome the band gap energy depends on the element's absolute temperature and has a value proportional to $e^{E_g/2kT}$, where k is Boltzmann's

constant ($8.617 \cdot 10^{-5}$ eV/K) and T is temperature in Kelvin (K). The energy bands are regions of many discrete levels so closely spaced that they may be considered a continuum, while the forbidden-energy gap is a region in which there are no available energy levels at all. This band structure arises because of the close, periodic arrangement of the atoms in the crystal, which causes an overlapping of the electron-wave functions.

Since the Pauli principle forbids more than one electron in the same state, the degeneracy in the outer atomic-shell energy levels breaks to form many discrete levels only slightly separated from each other. As two electrons of opposite spin may reside in the same level, there are as many levels as there are pairs of electrons in the crystal. This degeneracy breaking does not affect the inner atomic levels, however, which are more tightly bound. The highest energy band is the conduction band. Electrons in this region are detached from their parent atoms and are free to roam about the entire crystal. The electrons in the valence band levels, however, are more tightly bound and remain associated with their respective lattice atoms.

The width of the gap and the bands is determined by the lattice spacing between the atoms. These parameters are dependent on temperature and the pressure. In conductors, the energy gap is nonexistent, while in insulators the gap is large. At normal temperatures, the electrons in an insulator are all in the valence band, the thermal energy being insufficient to excite electrons across this gap. When an external electric field is applied, there is no movement of conduction band electrons through the crystal and, thus, no current. For a conductor, on the other hand, the absence of a band gap makes it very easy for thermally excited electrons to jump into the conduction band where they are free to move around the crystal. A current will, therefore, flow when an electric field is applied. In a semiconductor, the energy gap is intermediate in size, such that only a few electrons are excited into the conduction band through thermal excitation. When an electric field is applied, a small current is observed. However, if the semiconductor is in low temperatures, almost all electrons will fall into the valence band, and the conductivity of the semiconductor will decrease. An illustration of the three types of materials with their respective band gap diagrams is shown in Figure 2, and the band gap energy for several semiconductors can be seen in Figure 3.

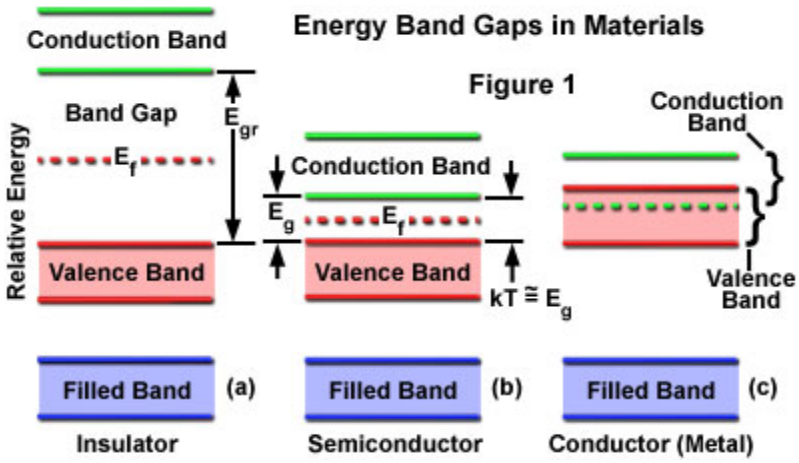

Figure 2. Representation of materials' energy bands and gaps. From [8]

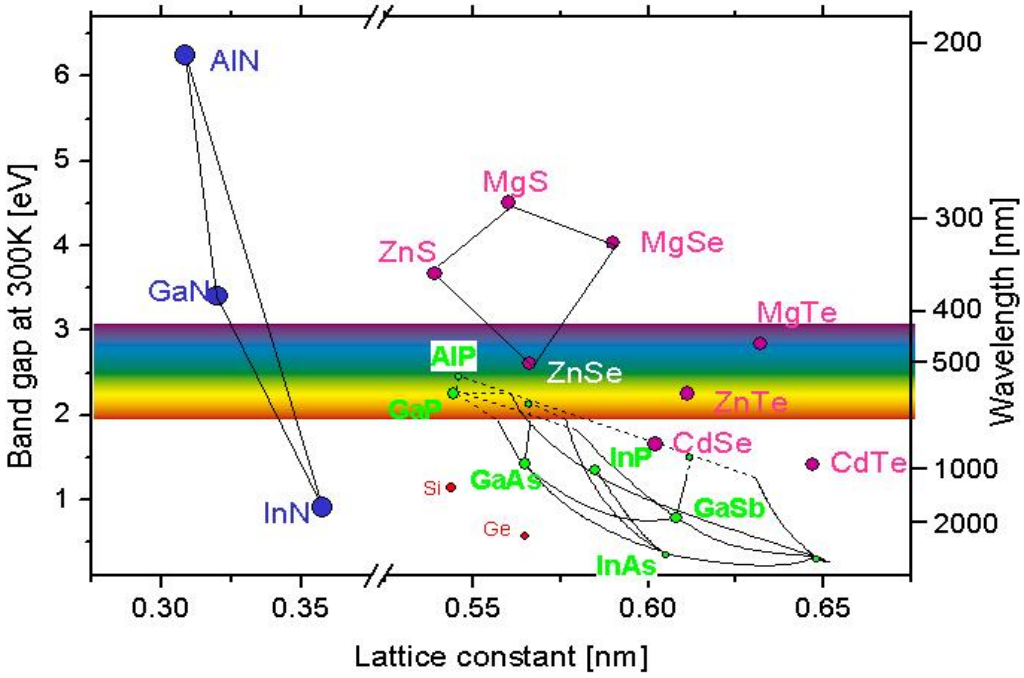

Figure 3. Band gap vs. lattice constant for many semiconductor compounds. Form [9]

From Table 1, it can be seen that some values for the band gap energy is 0.66 eV for Ge, 1.12 eV for Si and 1.42 eV for GaAs, at room temperature and normal pressure. These are typical values for the above elements when they are in a very pure form. In

materials with high impurities, band gap energy is smaller. Experimental data show that in most semiconductors, the band gap energy decreases with increasing temperature.

Table 1. Semiconducting elements and compounds together with their band gaps. From [10]

	Material	Band gap Transition	Band Gap Energy (eV)	
			0 K	300 K
Elements	C (diamond)	Indirect	5.48	5.47
	Ge	Indirect	0.74	0.66
	Si	Indirect	1.17	1.12
	Sn (grey)	Direct	0.09	0.08
Groups III-V compounds	GaAs	Direct	1.52	1.42
	InAs	Direct	0.42	0.36
	InSb	Direct	0.23	0.17
	GaP	Indirect	2.34	2.26
	GaN	Direct	3.50	3.36
	InN	Direct		0.70
	InP	Direct	1.42	1.35
Groups IV-IV compounds	α-SiC	Indirect	3.03	2.99
Groups II-VI compounds	ZnO	Direct	3.42	3.35
	CdSe	Direct	1.85	1.70
	ZnS	Direct	3.84	3.68
Groups IV-VI compounds	PbS	Indirect	0.28	0.41

B. DIRECT AND INDIRECT BAND GAP

Optical absorption in semiconductors can be understood in terms of the behavior of the electron energy E with the electron momentum $\vec{p}$ in the crystal, called the crystal momentum. In a direct band gap semiconductor such as III-V semiconductors (e.g., GaAs, InAs, InP, GaP) and in many of their alloys (e.g., InGaAs, GaAsSb), the photon-absorption process requires no assistance from lattice vibrations. Upon photon absorption, the electron is excited directly from the valence band into the conduction band without changing in its $\vec{p}$ vector. This process corresponds to a vertical transition in

the E - p diagram. The absorption coefficient of direct band gap materials rises sharply with decreasing wavelength λ_g, where λ_g is the corresponding wavelength of the band gap energy.

In indirect band gap semiconductors such as Si or Ge, photon absorption requires the absorption or emission of a phonon. When an electron in the valence band is excited to the conduction band, there is a change in its momentum in the crystal lattice, and this momentum change cannot be supplied by the very small momentum of the incident photon. Thus, the momentum difference must be balanced by a phonon momentum. The absorption process is said to be indirect, as it depends on lattice vibrations (phonons), which in turn depend on temperature. Since the interaction of a photon with a valence electron needs a third body, a phonon, the probability of photon absorption is lower than in a direct transition. Furthermore, the cut-off wavelength is not as sharp as in the latter case. Photon absorption in a direct band gap semiconductor for an incident photon with energy $h\nu = E_2 - E_1 > E_g$ and in an indirect band gap semiconductor for a photon with energy $h\nu < E_2 - E_1$ and a photon with energy $h\nu > E_2 - E_1$ are shown in Figure 4, where E_1 is the electron energy in the initial state and E_2 the electron energy in the final state.

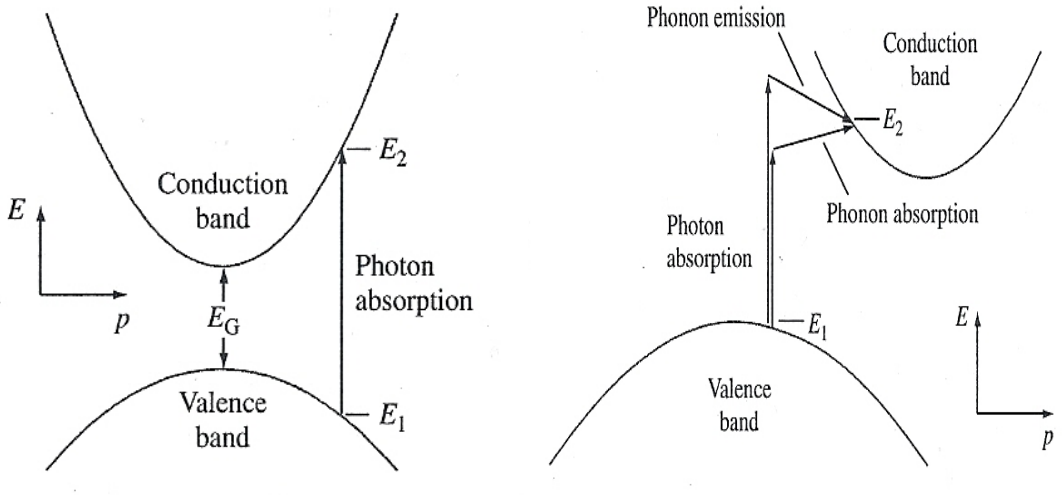

Figure 4. Photon absorption in a direct (left) and an indirect (right) band gap semiconductor. From [11]

C. CHARGE CARRIERS

At normal temperatures all the electrons in the valence band participate in covalent bonding between the lattice atoms. However, the action of thermal energy can excite a valence electron into the conduction band, leaving a hole in its original position. In this state, it is easy for a neighboring valence electron to jump from its bond to fill the hole. This now leaves a hole in the neighboring position. If the next neighboring electron repeats the sequence, and so on, the hole appears to move through the crystal. The hole acts, therefore, like a positive charge carrier, and its movement through the crystal constitutes an electric current with direction opposite to the direction of the electrons. In a semiconductor, the electric current, thus, arises from two sources: the movement of free electrons in the conduction band and the movement of holes in the valence band.

D. FERMI LEVELS

At zero Kelvin (K), electrons of a conductive solid are placed at the lowest energy levels of the zone, and the average electron energy is called the Fermi level. In imposing an electric field, the electrons in or near this level are excited and move to higher empty levels. The freed electron carriers, under the influence of the external electric field, can move, and when the direction is oriented, are construed as an electric current; we,

therefore, characterize the element as electrically conductive. The distribution function that describes the probability of occupancy of an energy level E of electrical carriers at a temperature T is given by the Fermi-Dirac function as

$$f(E) = \frac{1}{e^{(E-E_F)/kT} + 1} \tag{2.2}$$

where E_F is the Fermi energy or Fermi level. For energy values equal to the Fermi level, the function describes the Fermi level as a state with 50% chance of being occupied by an electron for the given temperature of the solid.

Accordingly, at absolute temperature, the Fermi energy level is shown as the upper level that is occupied by electron carriers. The probability of occupation of the Fermi level tends to be equal to one for energy values lower than the Fermi level and zero for the higher energy values. In semiconductors, the relative magnitudes of the Fermi–Dirac function are simplified based on the Boltzmann approach:

$$f(E) = e^{(E-E_F)/kT} \quad . \tag{2.3}$$

If we have a container that resembles the electron band, the specified quantity of a liquid that is inside the container resembles the electrons, and the liquid's surface resembles the Fermi energy. The more liquid (i.e., electrons) is added to the container, the more it will raise the surface of the liquid (i.e., Fermi energy) [12]. The Fermi level E_F depends on the concentration of holes in the valence band and the concentration of electrons in the conduction band and can shift inside the band gap close to these bands, a phenomenon we will analyze.

E. INTRINSIC, EXTRINSIC, AND DOPED SEMICONDUCTORS

Intrinsic conductivity comes from the switch over of excited electrons from a full valence band into the empty conduction band, and, more specifically, into the allowed energy levels of this band. Any solid that shows intrinsic conductivity is called an intrinsic semiconductor, and such semiconductors are usually composed of pure crystalline materials. Intrinsic semiconductors contain negligible numbers of impurities

compared to the number of thermally generated electrons and holes. In this case, the concentration of free electrons is equal to the concentration of free holes.

Strictly intrinsic semiconductors—pure materials without impurity atoms, donors, acceptors or crystal defects—are rare. Most constructive applications are based on introducing additional energy levels within the forbidden zone to increase the conductivity of the so called exogenous-extrinsic semiconductors. The most significant of the extrinsic semiconductors are the impurity or doped semiconductors, where extra atoms are adding, i.e., pentavalent atoms (donors) or trivalent atoms (acceptors) in tetravalent semiconducting elements, resulting in the rescission of the concentrations equality of the conductive electrons and holes. These two types of carriers are characterized according to the type of semiconductor impurities involved, as majority carriers and minority carriers, with the concentration of the former dominant over the latter.

In particular, the addition of donor atoms in the crystal lattice of the semiconductor implies enrichment of the lattice with conduction electrons. This structure leaves unaccompanied the extra donor's electron, which is loosely connected with the parent atom and, thus, detached by the thermal energy addition roaming freely in the solid, requiring minimal energy for the transition to the conductive band. Finally, the density of negative carriers is greater than the corresponding holes density, and the semiconductor is called an n-type semiconductor. That is, an n-type semiconductor is created when a pentavalent donor atom with approximately the same atomic dimensions as the parent crystal atom is placed in lattice position and provides electrons to the conduction band of the semiconductor, resulting in electrons majority over the holes. In this case, at zero K, the Fermi level shifts toward the conduction band of the semiconductor while remaining within the energy band gap, provided that the percentage of impurities is kept low so that the semiconductor is not degenerated.

Otherwise, when a semiconductor is doped with trivalent acceptor atoms, it uses an extra electron from the semiconductor's tetravalent atom in order to construct the

bond. Incomplete covalent bonding occurs through the hole and is moved freely in the crystal lattice, leading to holes conduction. As a result, the positive carriers outnumber the electrons, and the semiconductor is called a p-type semiconductor. Therefore, p-type semiconductors are created by adding acceptor electrons, while the Fermi level at zero K remains within the energy band gap, near the valence band—provided that the percentage of impurities is maintained at low levels so that the semiconductor is not degenerated. A visual representation of the shifting of Fermi's level can be found in Figure 5.

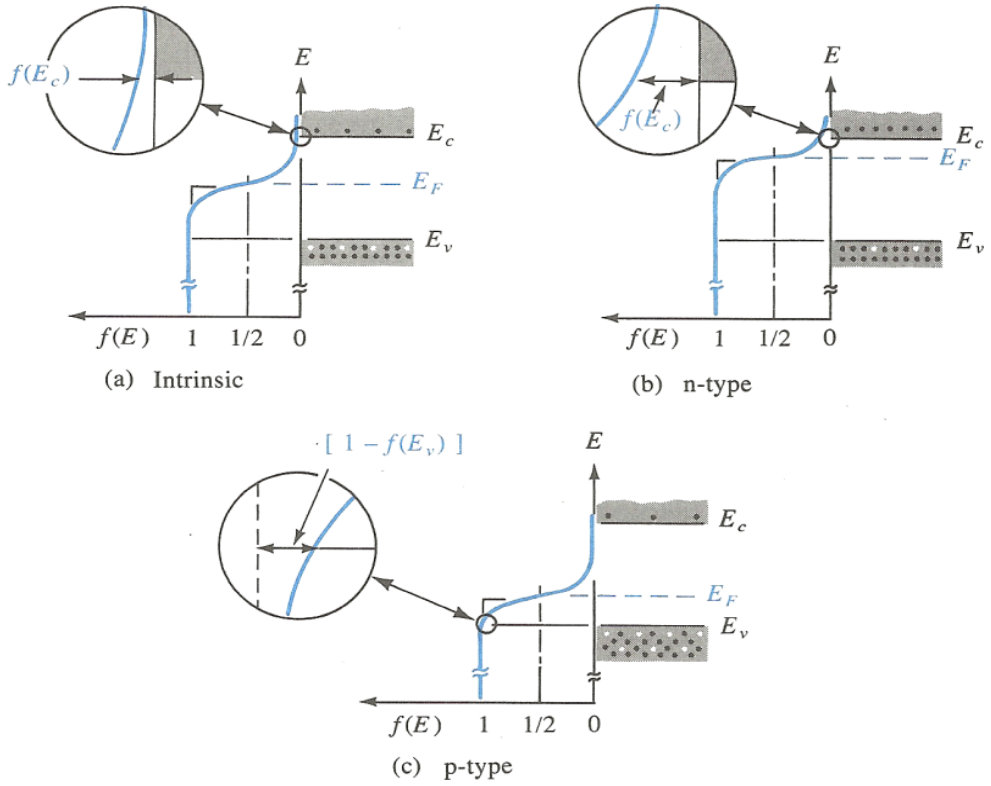

Figure 5. Fermi level for intrinsic, n-type, and p-type material. From [13]

F. P-N JUNCTION

A p–n junction is formed by joining together extrinsic semiconductors of opposite doping, a p-type semiconductor doped with acceptor impurity atoms and an n-type semiconductor doped with donor impurity atoms in full contact. Majority carriers in p-type semiconductors are holes and in n-type semiconductors are electrons. Due to their mutual repulsion, the free electrons of an n side are diffused in all directions, and some of

them can traverse the junction, ionizing an atom with a positive charge on the n side. Entering the p side, they recombine with a hole generating a negative ion. In other words, a part of the p-type majority carriers (holes) are diffused to the n-type section where the holes are fewer, leaving behind ionized, shallow acceptor levels, while n-type majority carriers (free electrons) are diffused to the p-section, leaving behind ionized, shallow donor levels. This process, and the increasing of the minority carriers' concentration near the interface of the two regions, subverts the equilibrium, which is restored after some time when almost all electrons and holes recombine around the junction (carriers' reunion) creating a negative zone on the p-side and a positive zone on the n-side.

The junction term refers to where the two types of semiconductor are in contact. The p–n junction exhibits properties that are highly interesting in modern electronics. The contact that is formed between them does not conduct current. The electro-charge carriers in the doped p-region and n-region are removed by the electric field. In this insulating layer, called the depletion region, the positive ions of the n-section and the negative ions of the p-section remain unchanged in the grid. Thus, the material loses locally its electrical neutrality, and the shaped electrostatic field prevents the further diffusion of majority carriers to the opposite part of the union. In this way, we observe two phenomena that evolve simultaneously. The diffusion process that tends to increase the charge area in the diffusion region and the electric field developed in the region tend to retain the carriers' diffusion. These phenomena are shown schematically in Figure 6, which also depicts the carriers' concentration at equilibrium.

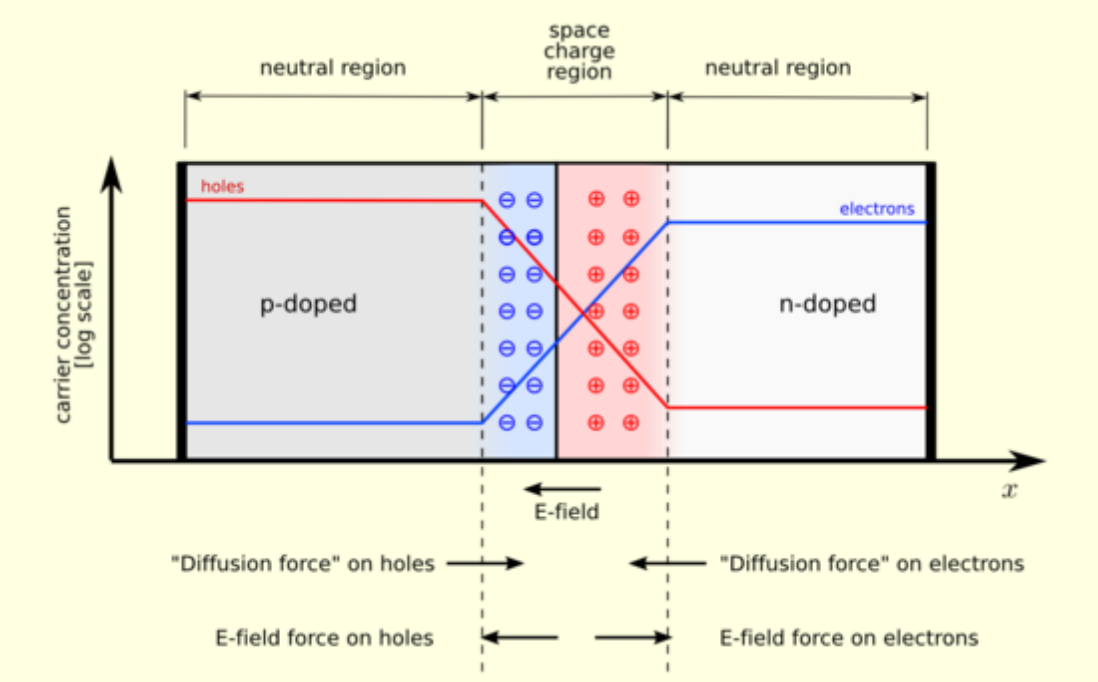

Figure 6. A p–n junction in thermal equilibrium with zero-bias voltage applied. From [14]

The two aforementioned zones create a potential barrier that counteracts the diffusion of the electrons from the n-side to the p-side. This potential barrier, the so-called built-in voltage V_{bi}, is obtained using the band model and the requirement that the Fermi levels line up in thermal equilibrium. This principle is illustrated in Figure 7.

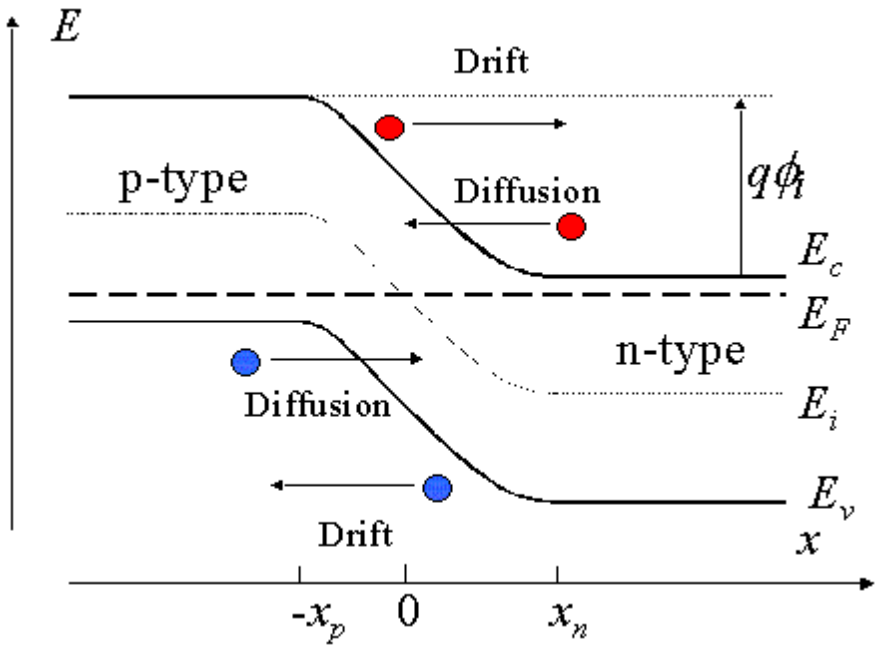

Figure 7. Energy-band diagram of a p-n junction. From [15]

Using this insulating level, we find that p–n junctions are often used as diodes, namely, as circuit elements that allow current flow only in one direction and not in the reverse. This property can be explained by the terms forward and reverse applied polarization, where the term polarization refers to the voltage applied to the p–n junction.

III. SOLAR CELLS

A. P–N JUNCTIONS IN SOLAR CELLS

We assume a p–n junction with a very thin and highly doped n-region and that irradiation is done from the side of this region. In the depletion region W, which extends mainly in the p-region, there is an electric field. Electrodes on the side of the irradiation (i.e., the n-region) must enable the irradiation to reach the device. They must have a low series resistance, and for this reason, when placed in the n-region, create an array of branched electrodes on the surface.

Since the n-region is very thin, most of the photons pass through it. They are absorbed within the depletion region of the p-region, and in these regions, electron-hole pairs are created. Because of the existence of the electrical field, the electron-hole pairs created by the photo generation are separated immediately. Electrons move in the neutral n-region, creating a negative-charge excess, and holes move to the neutral p-region, making it positively charged. This creates an open-circuit voltage to the terminals of the device. Thus, the p-region is positively charged with respect to the n-region. Connecting an external load, the extra electrons can move via the external circuit and reach the p-region, where they recombine with the extra holes located in this region.

Photons with large wavelengths penetrate deeper and reach the p-region, where they are diffused, since in this region there is no electric field. Each pair's electron generated has a mean recombination time and is spread over the diffusion length L_e. Thus, the electrons lying at a distance less than average diffuse relatively easily up there and under the influence of the electric field are transferred to the n-region. Consequently, only the carriers in a distance less than the diffusion length provide current and are involved in creating the photovoltaic effect. By this process, the electron moving to the n-region under the influence of the field adds an additional negative charge in this region. Correspondingly, the hole left in the p-region adds a positive charge there. Pairs located at a distance greater than the diffusion length L_e of the depletion region are lost due to recombination. The same applies in the n-region for short wavelength photons. Thus,

holes which are in a distance less than the diffusion length L_h from the depletion region move in the same manner to the p-region. Therefore, we can say that stimulation of electron-hole pairs contributing to the photovoltaic effect occurs within a zone of width $L_h + W + L_e$. This process is illustrated in Figure 8.

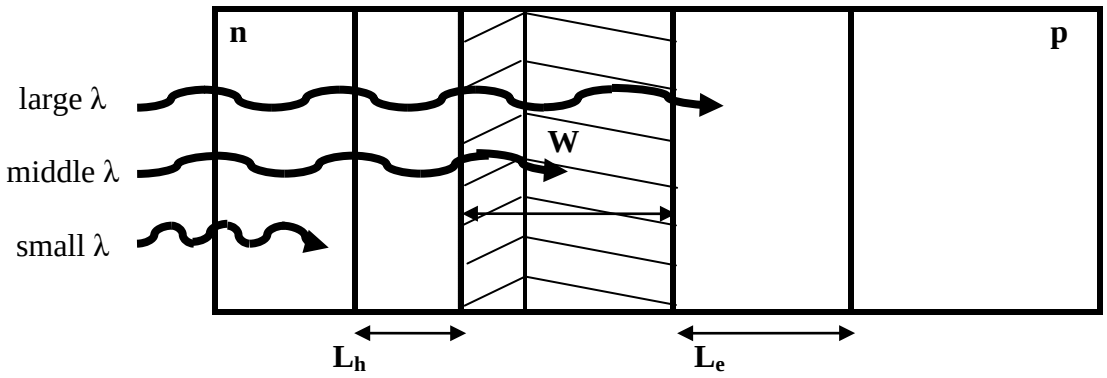

Figure 8. Photons absorption in a PV cell under illumination.

B. HOW SOLAR CELL WORKS

When the cell is illuminated, the photons having energy greater or equal to the energy band gap of the semiconductor may be absorbed by the bound electrons and cause the formation of an electron-hole pair, which is immediately separated due to the internal electrostatic field. A solar cell cannot convert the entire amount of solar radiation received on its surface into electrical energy. A part of the radiation is reflected from the surface of the cell and diffused back into the environment. Afterwards, from the radiation that penetrates the semiconductor, those photons having energy smaller than the energy band gap cannot be absorbed. For these photons, the cell behaves like a transparent body. This pattern is shown in Figure 9.

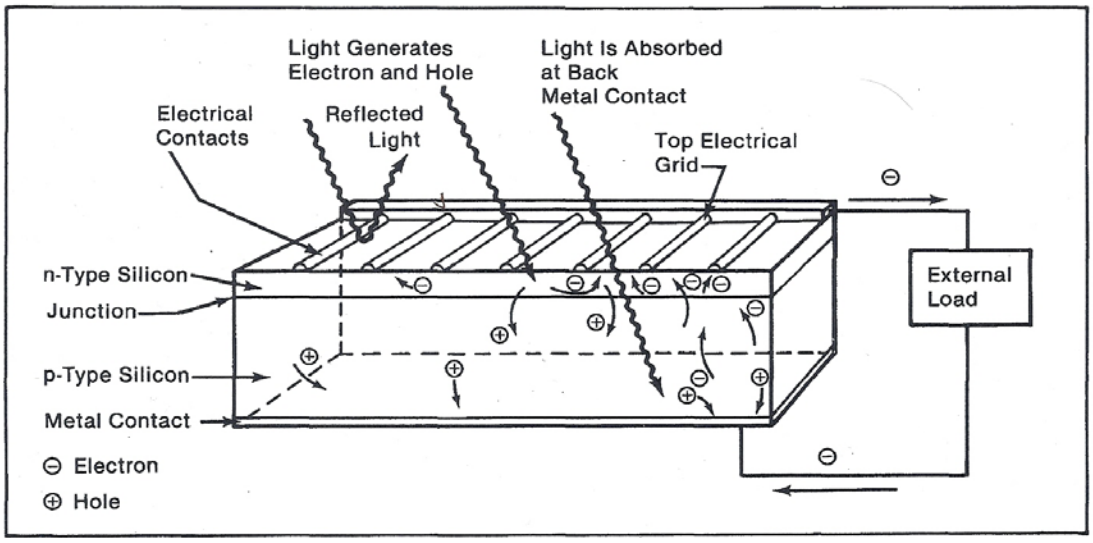

Figure 9. Light incident on a cell. From [16]

Shorting the terminals of the device, the extra electrons of the n-region move through the external circuit to counteract the additional holes in the p-region. The current due to this flow of excited carriers is called photocurrent I_L, (where L stands for light) depicted in Figure 10.

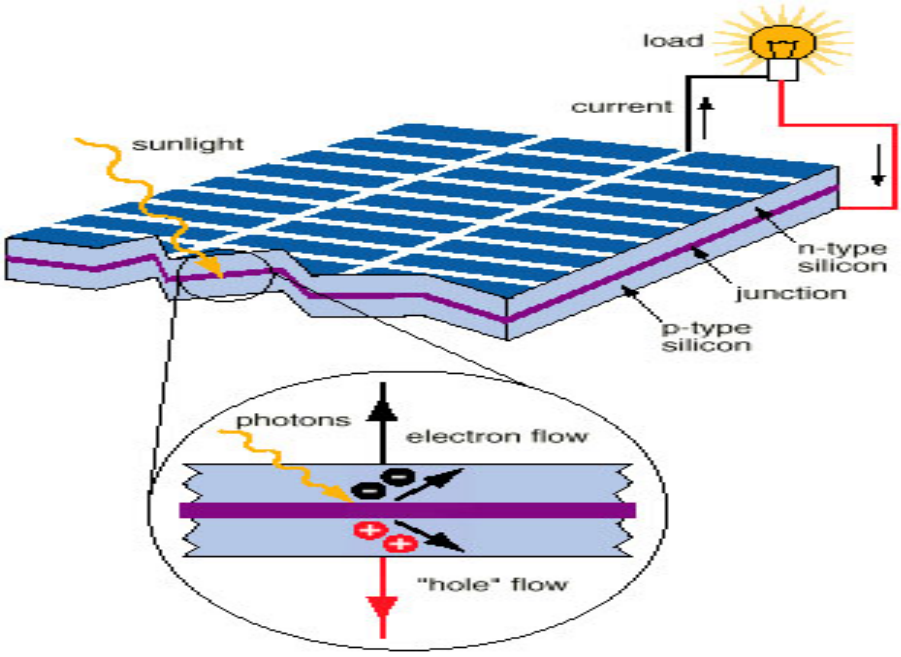

Figure 10. The PV effect in a solar cell. From [17]

In an ideal PV cell under illumination, the short-circuit current I_{SC} is equal to the produced photocurrent since the load resistance R is zero, causing the voltage to also be zero. If a load resistance is connected to the circuit, the photocurrent causes the creation of a voltage V in the cell, which forward-biases the p–n junction and reduces its potential as well as the infusion of minority carriers and their diffusion, just as would happen in a normal diode. Therefore, due to the forward-bias voltage, a forward-bias current I_F, which opposes the photocurrent, will be present. This is given by

$$I_F = I_0(e^{eV/\eta kT} - 1) \tag{3.1}$$

where I_0 is the reverse saturation current and η the quality factor which ranges from one to two. The resulting net p-n junction current I is

$$I = I_L - I_F = I_{SC} - I_0(e^{eV/\eta kT} - 1) \quad . \tag{3.2}$$

C. SOLAR CELL I-V CHARACTERISTICS (BASELINE PARAMETERS)

Much can be learned about solar cell operation by examining the basic form of Equation (3.2). Using the equality of the two produced currents in the open-circuit state, we have the resulting open-circuit voltage

$$V_{OC} = V_t \ln\left(1 + \frac{I_L}{I_S}\right) \tag{3.3}$$

where I_S is the reverse saturation current, and V_t is the thermal voltage.

The graph between the output current and output voltage of a solar cell is called the I-V curve and describes its energy conversion capability at the existing conditions of irradiance and temperature. A representative I-V curve of a typical solar cell is plotted in Figure 11.

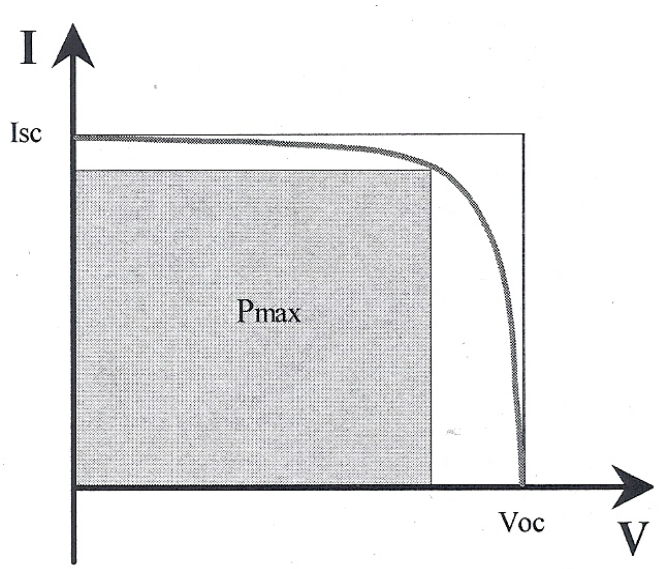

Figure 11. I-V curve for a photovoltaic cell showing its maximum power rectangle. From [18]

Referring to Figure 11, the span of the I-V curve ranges from the maximum possible current, where the voltage is zero, to zero current and the maximum possible voltage in the circuit. That is, the span is from the short-circuit current I_{SC} at zero volts to the open-circuit voltage V_{OC} at zero current. The calculation of these points is done by the intersection of the characteristic of the solar cell with the respective axes. The output power produced by a solar cell is given by

$$P = VI \ . \tag{3.4}$$

The maximum output power point $P_{\max}$ is at the knee of the curve, resulting from the corresponding points of maximum current $I_{\max}$ and maximum voltage $V_{\max}$ and is equal to the area of the rectangle. The maximum current and maximum voltage can be calculated either by solving the equations of the solar cell characteristic and the load characteristic or graphically, by drawing vertical lines outward from these points to the corresponding axis.

The fill factor FF is an indication of how close the characteristic of the solar cell is to the ideal rectangular shape. The I-V curve is close to this shape, and the fill factor's value is close enough to one. But the properties of the p–n junction make this impossible;

the normal value for the fill factor is between 0.70 and 0.85 depending on the material and structure of the device. Fill factor is defined as the quotient of the product of the voltage multiplied by the current for the point of maximum output power to the power that the open-circuit voltage and short-circuit current would make if they were multiplied together. The fill factor is given by

$$FF = \frac{P_{\max}}{V_{OC} I_{SC}} \ . \tag{3.5}$$

Schematically, the fill factor arises from the I-V curve as the ratio of area bounded by the voltage and current values that maximize the power to the area, defined by the open-circuit voltage and short-circuit current.

The most basic parameters for evaluating the conduct and operation of a PV cell are the fill factor, the short-circuit current, and the open-circuit voltage. These parameters determine the efficiency of the cell, which equals the ratio of the maximum creditable power of the cell to the incident light power per unit area, which is the input power from the sun P_{in} . Thus, the efficiency is calculated from

$$\eta = \frac{P_{\max}}{P_{in}} \ . \tag{3.6}$$

The input power from the sun is based on the air mass number where the cell is located in relation to the sun. The efficiency of a solar cell is sensitive to variations in both the power and spectrum of incident light. To facilitate an accurate comparison between solar cells measured at different times and locations, a standard spectrum and power density has been defined for radiations outside the earth's atmosphere and surface. The standard spectrum at the earth's surface is called AM1.5 to describe the dissipation of the energy put out by the sun due to atmospheric intercession, compared to the AM0 spectrum for space where we do not have any power losses. For this thesis, the light source used was the sun, and the solar cells were illuminated assuming an AM1.5 solar spectrum, which is used for terrestrial applications. The AM1.5 and AM0 spectrums are shown in Figure 12.

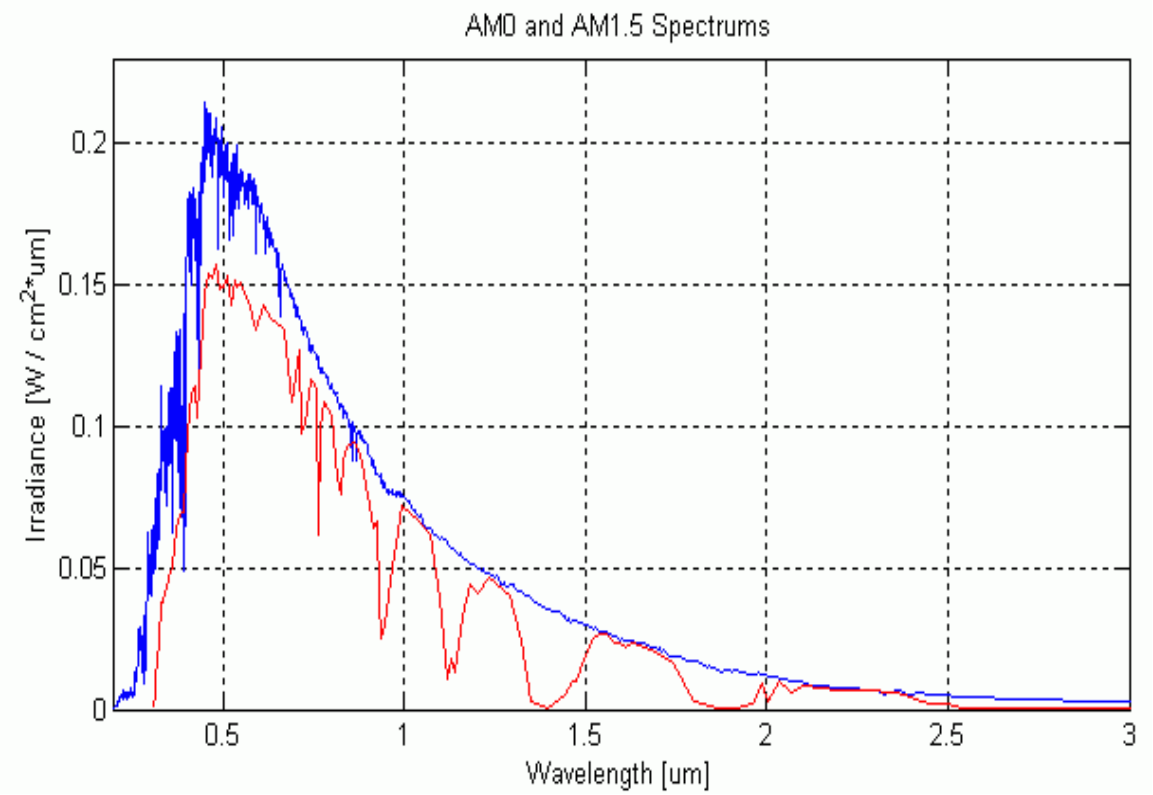

Figure 12. AM0 (in blue) and AM1.5 (in red) spectrum. From [19]

D. MULTI-JUNCTION SOLAR CELLS

Use of the full range of radiation in PV cells cannot be done, as photons with energy less than the band gap energy of the semiconductor material permeate without any absorption. Multi-junction PV cell is a technique used in solar cells for higher efficiency. The multi-junction PV cells, called multi-layered or tandem cells, are cells consisting of different material layers, wherein the unused photons of the first layer continue their drift towards the second layer, which has a lower band gap energy than the first and so forth, to stimulate their carriers. The band gap energies of a number of semiconductor materials are shown in Figure 13.

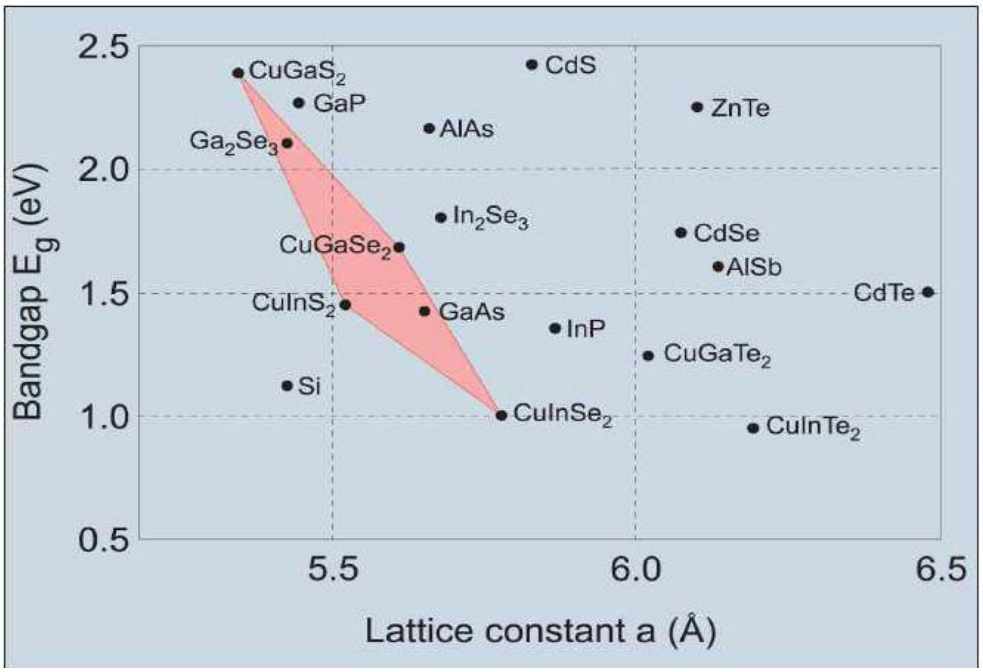

Figure 13. Band gap energies as a function of lattice constants for different semiconductor materials. From [20]

Each type of semiconductor has specific band gap energy and absorbs effectively only a portion of the electromagnetic radiation. The semiconductors are selected so as to absorb almost the entire solar spectrum, and the purpose is to produce electrical energy primarily by solar radiation. In multi-junction structures, different levels are used to absorb the largest possible part of the sunlight passing the semiconductor and convert it to electrical energy. In a simple solar cell, efficiency is quite limited. This happens because the semiconductor does not have the ability to absorb the entire spectrum of solar radiation impinging on it. That is, photons with energy less than the band gap energy of the semiconductor are lost in the passage through the semiconductor without interacting with it, or bumping into the crystal lattice, converting part of their energy to heat. In any case, they are not involved in converting solar energy into electrical energy, and this happens because they do not have sufficient energy to excite electrons from the valence band into the conduction band. Moreover, in photons with energy higher than the band gap energy, the extra energy is lost. Since part of the energy required to excite an electron from the valence band to the conduction band, creating one electron hole pair, is

absorbed, the excess photon energy is converted into heat. From Figure 14, it can be seen that the range of photon energies that the cell can transform into electric power is determined by the band gap.

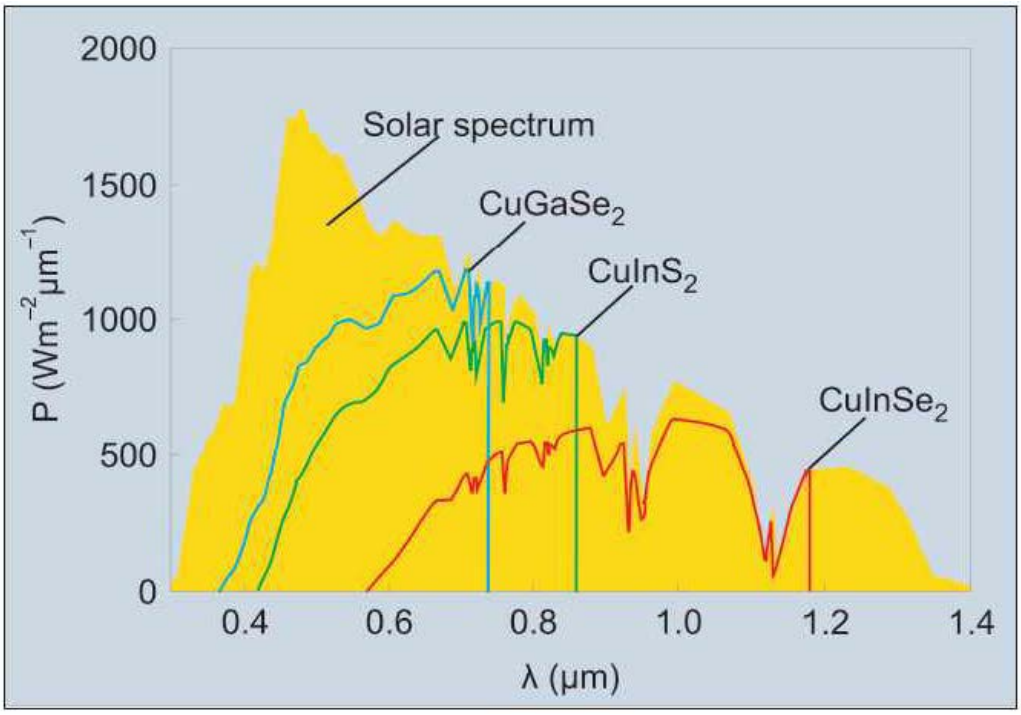

Figure 14. Solar spectrum and response of CIGS materials. From [20]

The current produced by an individual layer must have the same value as the current produced by each of the other layers (current match), resulting in the final current of the multi-junction. The need for current match is related to the fact that layers connected one above the other form the multi-junction, operating as current sources connected in series. Therefore, the total current will be determined by the layer with the lower output current, while the voltage from each is added together to give the overall voltage. If a layer producing lower current is added to a multi-junction consisting of layers producing higher current, then the current of the resulting multi-junction will be limited to the current of lower current layer.

An important advantage of multi-junction cells is that each layer can be assigned to a specific range of the solar spectrum using elements with different band gap energies

from the several categories of the Periodic Table. From Figure 15, it can be seen that the front layer absorbs high-energy photons, the next layer, photons with slightly less energy, and so on.

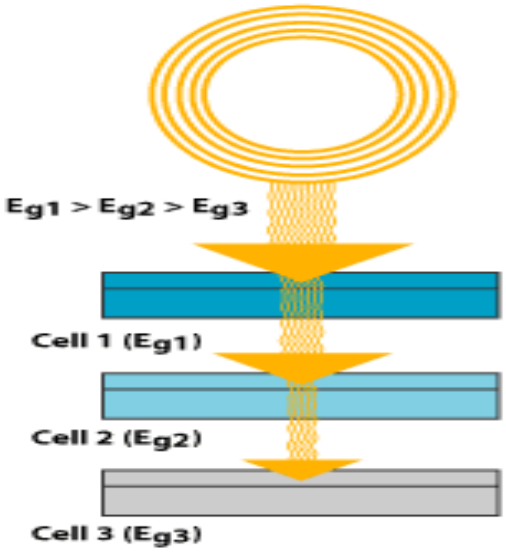

Figure 15. Schematic of a triple-junction solar cell. From [21]

IV. CIGS SOLAR CELLS

A. THIN-FILM SOLAR CELLS

The need for new, advanced materials and systems having new properties led to thin-film technology. The process and the mechanisms of molecule deposition from the gas phase to the surface of the solid material is the basis of this technology. This new technology is coming to replace the conventional one as more efficient and more cost-effective. Thin-film solar cells are the latest development in the field of photovoltaic cells, and there is considerable hope for wide spread use in the production of electricity.

The thin-film is the microstructure created by the individual layers of a material-objective on the surface of a solid (bulk) material, where one dimension is orders of magnitude smaller than the other two. Thin-films, with thicknesses ranging from a few nanometers (nm) up to a few microns (μm), have properties that are significantly different from those of solid materials and surfaces. Alterations are especially important when the thickness is very small or in the early stages of development. These differences are mainly due to microstructure and the creation of incorporations that are generated during the course of the transformation of the free atoms of a gas phase directly into a solid phase. In most deposition techniques, thin-films are deposited on the surface of a material at temperatures much lower than the melting temperature of the given material, and the growth of the film takes place under non-equilibrium thermodynamic conditions. These conditions are responsible for forming various metastable phases of unformed and nanostructured materials. The development of single-layered or multi-layered thin-film structures gives to the overall system the desired physical and chemical properties required for the specific use as well as new, exceptional properties to extend their scope of application and lifetime duration.

In general, construction consists of depositing a semiconductor that absorbs light onto a substrate, which may be coated glass, metal, or plastic. These semiconductor materials are not required to be thick, because they absorb light very efficiently, resulting in generated solar cells that are very thin, lightweight, durable, and easy to use.

Regardless of the applied deposition technique in thin-films, there is a set of fundamental parameters to control, the most significant of which are the substrate temperature, deposition rate, pressure of the ambient gas within the deposition chamber, and the energy of the flow of deposited particles. In thermal deposition, the contribution of the energy of the flow of deposited particles to the dynamics of the surface energy is insignificant, considering the fact that it is one to two sizes smaller than the bond forces of the surface components. In non-thermal deposition techniques, however, the energy of the flow of deposited particles strongly influences the film's properties. Of course, there are other factors, such as the thermodynamic properties of the system, the crystallinity, the orientation, the chemical properties, and the substrate lattice constants to influence the film's properties. These properties are not independent and optimizing one affects the others. The interdependence of these parameters contributes to the selection of the most suitable deposition technique.

In the industrial production of thin-film and layered materials, there are two major categories of development techniques: chemical vapor deposition (CVD) such as plasma-enhanced CVD (PECVD) and physical vapor deposition (PVD) such as sputtering and pulsed laser deposition (PLD). The common element of these techniques is deposition from the gas phase, and they are often supported by sputtering procedures since it is though bombardment with ions that helps optimize the properties of the deposited films. Their main difference is in how the deposition process of thin-films is started; in the case of PVD, it is done by physical transfer of atoms, ions, or molecules, and in CVD, via a chemical reaction.

From the semiconductor materials that exhibit the photovoltaic phenomenon, only some conform to the conditions for widespread use in high-efficiency solar cells. The ideal material for use in photovoltaic technology must be a direct band gap semiconductor with a band gap between 1.1 and 1.7 eV, high solar optical absorption, high quantum efficiency of excited carriers, long diffusion length, low recombination velocity, and ability to form a good electronic junction (homo/hetero/Schottky) with suitably compatible materials. Given that the most important requirement is high

efficiency, the most appropriate material for PV technology is thin-films [22], [23]. The aforementioned dependence of the conversion efficiency on the semiconductor band gap is shown in Figure 16.

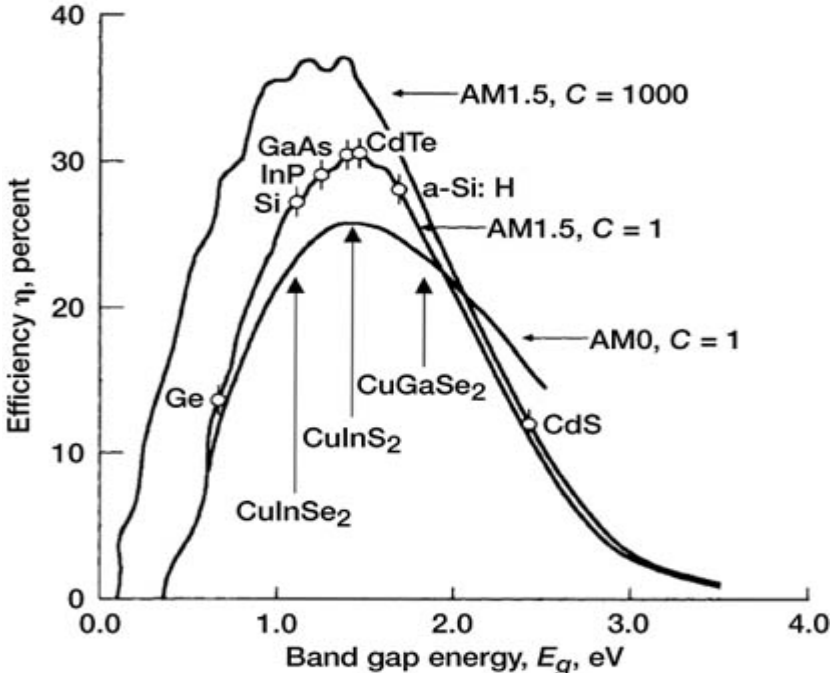

Figure 16. Dependence of the conversion efficiency on the semiconductor band gap. From [24]

The dominant semiconductor material used in the current PV market is undoubtedly silicon. In physical terms, Si is not among the most suitable materials to be used in the PV conversion of solar irradiation. From Figure 17, it can be seen that it is an indirect band gap semiconductor with a relatively small band gap energy of the order of 1.1 eV and a low absorption coefficient. For example, for 90% of solar irradiation to be absorbed requires 100 μm thickness of Si, while for GaAs, which is a direct band gap semiconductor, only 1 μm thickness is needed [16]. An inevitable consequence of such a large thickness is that Si used in solar cells must be of very high purity so as to avoid recombination of carriers and contribute actively to the generation of photocurrent.

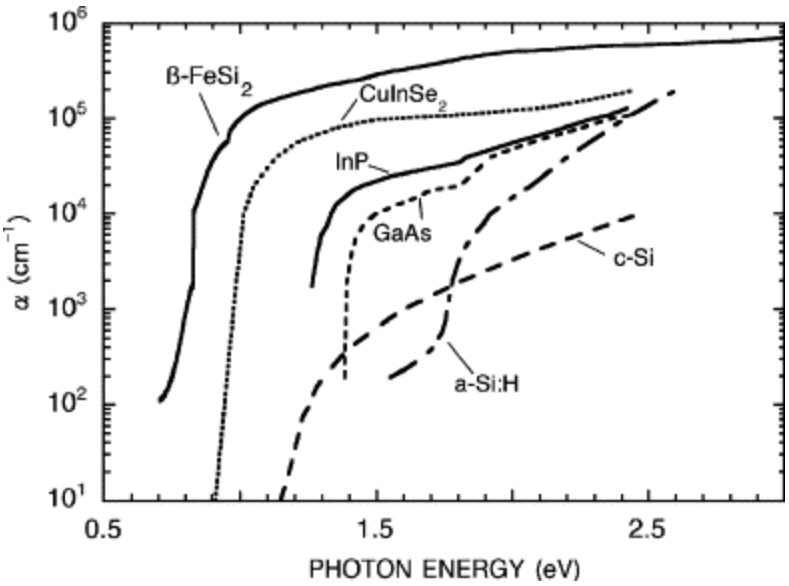

Figure 17. Absorption coefficient of various semiconductors as a function of photon energy. From [25]

Since high efficiency is the most important requirement, the best material for PV technology is thin-film elements, which have many advantages over crystalline Si. The consumption of materials is less because the required thickness of the active layer is only a few micrometers; therefore, impurities and crystalline defects are acceptable to a much greater degree than in crystallized Si. Thin-films can be deposited on cheap substrates such as glass by various methods under vacuum, while bent and flexible substrates such as polymeric sheets can be used, making the device particularly lightweight. Candidate materials for the manufacture of low-cost TFSC are amorphous Si (a-Si), the CdTe, chalcopyrite materials CuInSe2 (CIS), and their alloys made by adding Ga or S. Of these materials, a-Si currently holds the largest share of the PV market, having an absorption coefficient sufficiently greater than that of crystalline Si and a direct band gap of 1.5eV, which is close to ideal. The main disadvantage is the decrease in performance with relation to the exposure time to solar irradiation.

The semiconductor materials CdTe, tripartite CIS, and quadripartite CIGS, used in fabrication of TFSCs, do not exhibit similar problems of instability and degradation upon exposure to sun light. However, solar cells based on CIS materials have shown improvement during exposure to light under normal operating conditions. These

materials are direct band gap semiconductors and have high absorption coefficients. With regard to CdTe, although the band gap is 1.4 eV, close enough to its optimal values, efficiencies of 17.3% only have been recorded for the corresponding solar cells. Solar cell efficiencies at the research level for almost all the existing technologies from 1975 to today are shown in Figure 18. It is apparent that chalcopyrite solar cells have reached the performance of polycrystalline Si.

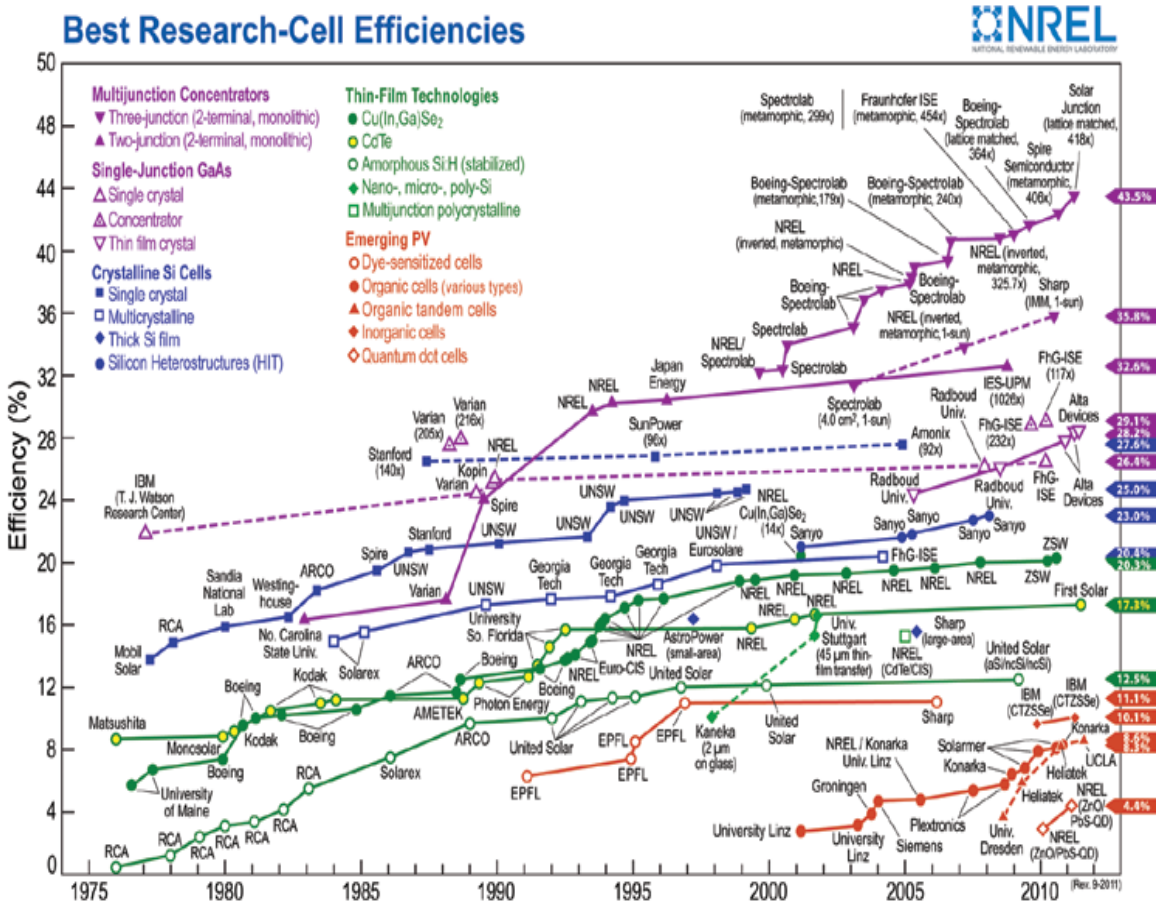

Figure 18. The best research-cell efficiencies. From [26]

It should be noted that an impressive increase in efficiency is expected, mainly using denominated tandem, triple, and multi-junction solar cells, which consist of multiple thin-film layers that utilize different energy regions of the solar spectrum. The

tandem junction cell that is investigated in this thesis consists of two CIGS thin-film layers with different band gap energies, as will be discussed later.

B. CHALCOPYRITE BASED TFSC

The most important problem for the scientific community is that before the fabrication of commercial systems using the Si technologies currently prevailing, an in-depth investigation of absorption mechanisms and the conversion of solar energy must be made. Chalcopyrite is a possible substitute for Si as an absorber for PV systems, and research and development for the optimization of the absorber's properties is called for.

A vertical cross section of the basic structure of chalcopyrite TFSCs is depicted in Figure 19. The p–n heterojunction is formed between a chalcopyrite p-type semiconductor, which is the absorber of the solar cell, and a doped ZnO n-type semiconductor.

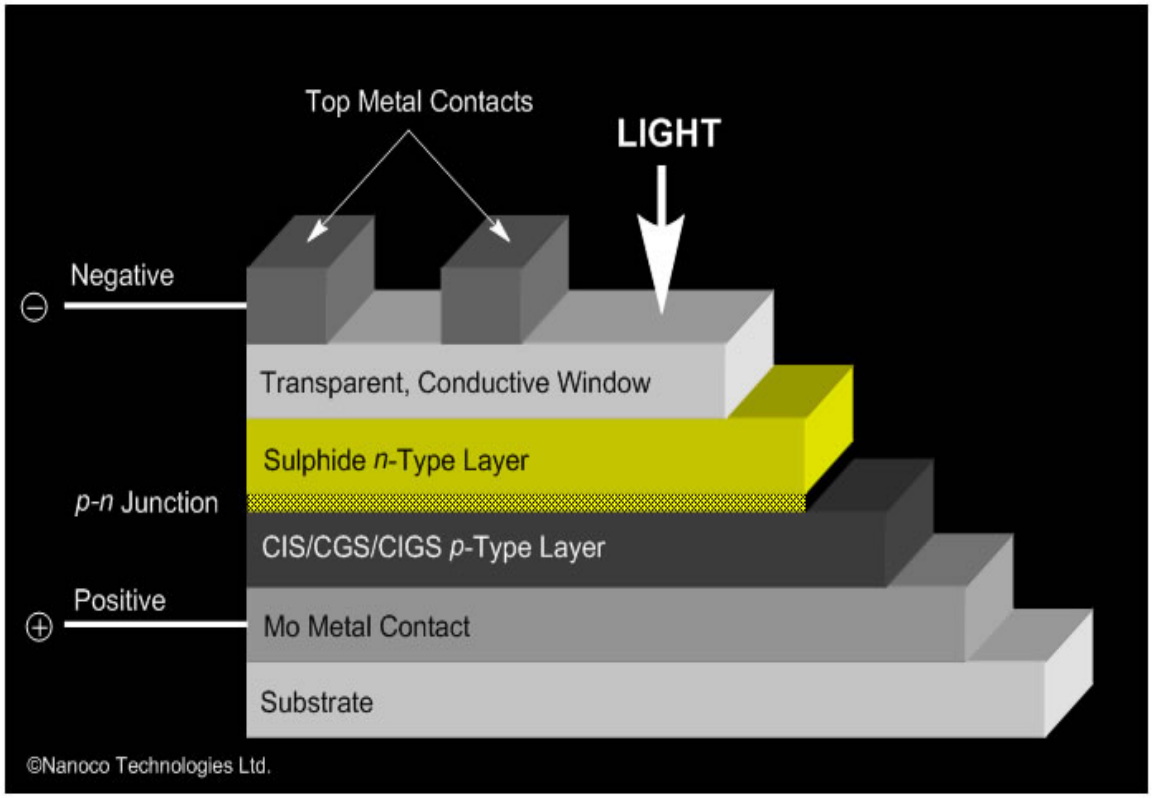

Figure 19. TFSC with chalcopyrite absorber layer. From [27]

Part of the incident radiation on the surface of the collector penetrates the cell, and photons with energies greater than the band gap energy reach the absorber layer, where the creation of electron-hole pairs is taking place. The quality of the heterojunction is improved by introducing an intermediate layer adjusting the band gaps between the absorber and the window layer, with the predominant material for this buffer layer CdS. On top of the buffer layer the ZnO/ZnO:Al bilayer is deposited as a transparent conducting oxide (TCO) which is considered the window of the solar cell since it is opaque to most of the solar spectrum.

1. Substrate

The substrate used in these arrangements is usually a common soda-lime glass. The introduction of Na from the glass soda-lime substrate during the growth of the absorber contributes to the quality of the absorber. Although the diffusion mechanism function of Na is not fully understood, its presence in the growth of the absorber is necessary for high efficiency devices. The general specifications that the substrate should meet are mechanical stability and thermal-expansion coefficient congruence with the next deposited layer. The deposition of the absorber requires a substrate temperature of at least 350 C, while the elements with the highest efficiencies have been deposited at the maximum temperature of 550 C, which the glass substrate can withstand without becoming particularly soft. Because the glass composition usually contains various acids, which provide the necessary defects to be diffused into subsequent layers during processing, a process that allows a controlled Na flow it is often preferred. Because of various other defects that the glass substrate may have, experiments with other types of substrates have been done; however, the cost and the wide variation in thermal-expansion coefficients are prohibitive factors for their wide use.

2. Back Contact

To be able to form an ohmic contact between a metal and semiconductor, the metal should have a higher work function than that of the semiconductor. Mo is usually used as a back contact in chalcopyrite devices since it is highly anticorrosive and creates a contact with the absorber due to the $MoSe_2$ interlayer formed during its deposition. The

back-contract thickness is determined by the resistance requirements of each solar cell. The properties of the Mo layer and the selection of the glass substrate are of critical importance to the quality of the cell because of the role of Na, which diffuses from the glass substrate to the growing layer of the absorber through the Mo layer. This trend has been found to improve crystallographic properties and doping in CIGS thin-films. By depositing various compounds prior to the deposition of the absorber, the diffusion of Na is controlled and homogeneous, allowing the use of other types of substrates as a back contact without any significant change in the cell's performance, given that a sufficient amount of Na is provided.

3. CIS/CGS/CIGS Absorber Layer

$Cu(In,Ga)(Se,S)_2$ alloys from the I–III–VI group of the periodic table are used as absorber layers that crystallize in the quadratic structure of chalcopyrite. This system of $Cu(In,Ga)(Se,S)_2$ type chalcopyrites includes a wide range of band gaps. $CuInSe_2$ has a relatively low band gap of 1.04 eV but can adjust better to the solar spectrum by replacing part of In with Ga and part of Se with S. Chemical and percentage composition of the chalcopyrite can vary the band gap from 1.04 eV for $CuInSe_2$ to 1.53 eV for $CuInS_2$ to 1.7 eV for $CuGaSe_2$ (CGS), up to 2.5 eV for $CuGaS_2$. The current laboratory record for efficiency of a CIGS chalcopyrite solar cell is 20.3%, as illustrated in Figure 18. One major advantage for absorbers in this category is the fact that they exhibit non-toxicity, in contrast with CdTe absorbers (which makes them unacceptable). Moreover, they exhibit excellent stability in electrical properties in all stoichiometric ratios in which they are manufactured. However, the use of rare materials such as In and Ga increases the production cost of the entire device.

4. Buffer Layer

The deposition of a thin, transition layer between the absorber and the window layer is required, the role of which is to adapt the band gaps of these layers. Additionally, it improves the lattice matching at the interface and protects the surface of the absorber from damage that can be caused by the deposition of the next layer. Due to the toxic nature of cadmium, it is preferable not to use it in solar cells, despite the fact that the

amount present is very low and safety rules are respected during production. For a solar cell not containing cadmium, it should be replaced by another element, or if possible, the window layer may be deposited directly to the absorber layer. Therefore, efforts are made to replace it with the less toxic ZnSe and ZnS.

5. Window Layer

A TCO is used as a front contact in order to create the heterojunction with the absorber and to gain as much photocurrent as possible from the solar panel with increasing the energy gap of the window layer. This layer should allow the largest possible percentage of photons to reach the absorber layer and is required for good conductivity and high transmittance in visible light. Conductivity depends on the concentration and mobility of charge carriers, and its increase is usually achieved after mixing with elements such as Al. However, increasing the concentration of impurities using alloys leads to the reduction of the permeability of films at long wavelengths. Therefore, an increase in the mobility of carriers should be performed primarily by improvement of the film's crystallinity. In PV technology, except from ZnO many different TCOs have been used as transparent windows of the cell. These are the indium–tin oxide (ITO), the indium–gallium oxide (IGO) and SnO_2. However, ZnO is considered the most competitive in cost and properties.

6. Collector

At the top of the solar cell, a metal grid is placed, which, together with the window layer, represents the front contact of the cell. This grid shape is used so that most of the solar radiation can penetrate and reach the absorber layer without being significantly reflected. In this section, the collection of the current carriers is done and the contact between the metal and the underlying ZnO layer must be ohmic with low resistivity in order to avoid carriers' losses in their interface. In most of the high efficiency solar cells, a ZnO front contact is used with an Al/Ni metal grid.

C. CIGS FORMATION

Ternary semiconductor compounds from the I–III–VI group of the periodic table are characterized by the fact that they are crystallized to the structure of chalcopyrite in a relatively wide range of variation in their percentage composition. Their active part consists mainly of two ternary alloys, CIS and CGS, and both have similar structures. CIS's crystal structure is similar sphalerite. The difference is that the elements of the II group of the periodic table are replaced with elements of the I group as copper, and the III group as indium or gallium. Each copper and indium atom joins two selenium atoms with two covalent bonds, and each selenium atom creates two bonds with one copper and one indium atom. The bonds between atoms are characterized by the fact that each atom can receive or provide as many electrons as needed to maintain an average of four valence electrons. Their structure is considered to assist the suppression of device degradation due to Cu migration.

The possible phases of the CIS system, distinguished in the ternary phase diagram in Figure 20, are shown below.

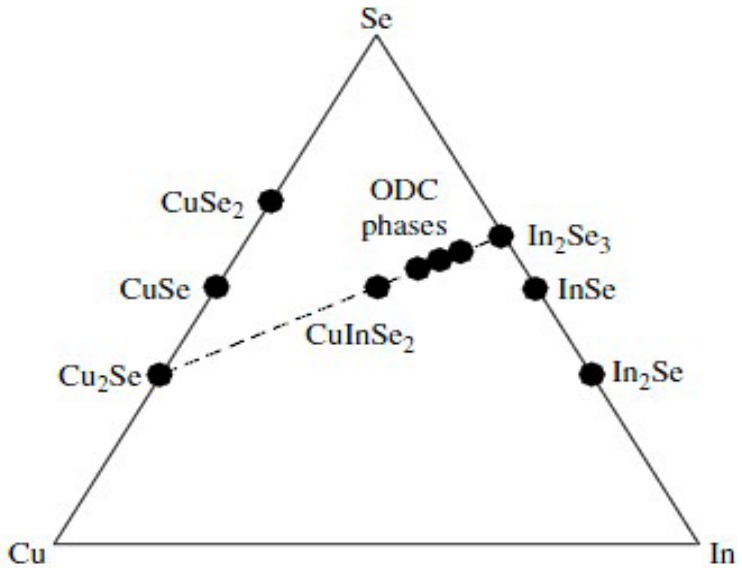

Figure 20. Ternary phase diagram of the Cu–In–Se system. From [28]

PV CIS cells produced in an excess selenium environment, i.e., under normal thin- films growth conditions, have elements concision located near or on the line connecting Cu_2Se and In_2Se_3. Various other phases occur close to the desired CIS state, such as ordered defect compounds, which have a lattice structure similar to that of chalcopyrite, wherein intrinsic defects are also arranged.

Auger electron spectroscopy in CIS films prepared in conditions of excess copper (Cu-rich films) show additional phases, different from that of chalcopyrite, and one of them is the Cu–Se phase. Cu-rich compositions are avoided in solar cell fabrication due to the formation of Cu–Se shunt paths along CIS grain boundaries, which reduce cell performance. Similarly, Cu-rich CGS films consist of a near-stoichiometric ternary CGS phase and Cu–Se segregating due to the copper excess. In the case of quadripartite CIGS, copper-excess conditions during the compound process have been found to improve the morphology of polycrystalline films since they enhance the size of the grains. The arrangement and coexistence of different phases in a material and the separation of those phases impact decisively the optical properties of the material, i.e., the absorption of radiation.

During the first research and development years of CIS PV technology, the production process consisted of the vacuum evaporation of the elements. It soon became clear that maintaining the stoichiometry of the reaction was dependent notably on the correct ratio of copper–indium flow with a gas selenium existence above the surface of the growing film. Positive progress for their commercial development followed, resolving around the deposition of indium and copper in the molybdenum metal contact, and a subsequent ‘selinization’ achieved by a hydrogen–selenium supply over the surface at 400 C. This selinization process gives very high quality materials and can even produce uniform films on large surfaces. Selenium fusion in copper and indium levels causes significant increase in volume and, consequently, high stresses in the film. These problems are solved by careful control of the substrate preparation details, the molybdenum deposition, establishing the copper and indium levels, and control of the selinization process.

The major drawback faced by CIS cells is a low open-circuit voltage and, thus, a limited performance due to the small 1.02 eV band gap that they have. The addition of gallium at the Mo, Cu-In interface gives an actual copper-indium-gallium-selenium (CIGS) alloy with significantly improved performance. CIGS cell has a band gap that increases with the gallium percentage addition, symbolized in literature as the composition ratio $Ga/(In+Ga)$, or otherwise, the x value in the chemical formula $CuIn_{(1-x)}Ga_xSe_2$. This ratio, or x value, can vary from one, resulting in pure copper indium selenide (CIS), to zero, resulting in pure copper gallium selenide (CGS). The quaternary CIGS system has an adjustable band gap that varies with the Ga content over a range of 1.04–1.68 eV [29]. Utilizing this wide band gap range, we can manufacture PV cells to better exploit the solar spectrum in the region that will be used. For instance, Greece and Denmark have fluctuations in the AM1.5 solar spectrum since it is a function of the angle relative to normal on the Earth's surface. Using the same materials and changing the Ga content in CIGS cells, we manage to adjust a cell's band gap to the specific region's spectrum.

Another basic characteristic of CIGS is high tolerance of differences in the composition without significant changes in the optical and electronic properties. This property is related with the very low energy required for the formation of various defects and to their electrical neutrality. Such complexes of imperfections create structures poor in copper and indium-rich but with no significant impacts on PV conversion. CIGS has the property of not being easily distorted by external factors. On the contrary, distortion is controlled by the intrinsic defects of the material. The p-type samples are manufactured if the material is poor in copper and heated to a high vapor pressure of selenium, while materials with copper excess and selenium ellipse, tend to be n-type.

Chalcopyrite PV cells use mainly the principle of heterojunction in the interface that occurs between two layers, or regions, of dissimilar crystalline semiconductors. Under this principle, semiconductors have unequal band gaps, as opposed to a homojunction; and for accuracy, the n-type semiconductor has a greater band gap than the p-type semiconductor. A typical PV cell based on quadripartite chalcopyrite polycrystalline films is shown in Figure 21.

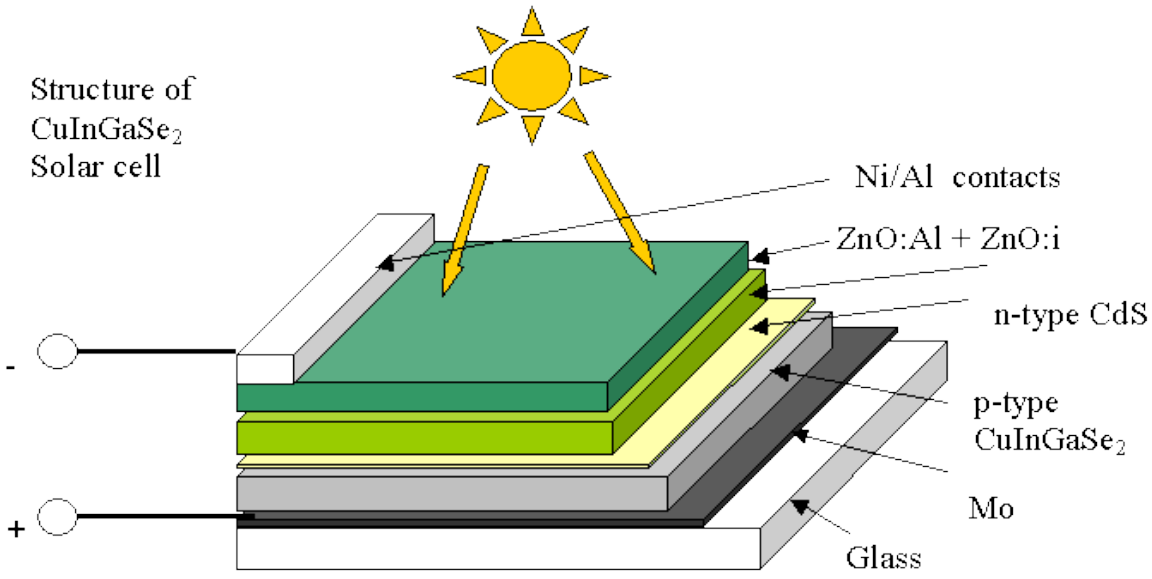

Figure 21. Typical layout of a CIGS-based PV cell. From [30]

A ZnO layer, with a band gap of 3.3 eV, is typically used as the n-type semiconductor, the transparent window layer that facilitates solar radiation's passing through the cell. The absorption of solar radiation and creation of electron-hole pairs take place in the p-type semiconductor, namely the chalcopyrite characterized as the absorber. High absorption coefficients allow the use of thin layers of a few microns thickness with high impurities concentration and intrinsic defects. On the other hand, during the heterojunction formation, the generated interlayers have also high defects percentage, and the carriers' recombination in the interlayer is very likely.

The ZnO/CIGS heterojunction is not considered propitious for carriers shift, because ions created during the ZnO preparation reinforce the electron-hole pairs recombination in the interlayer and can damage the surface of the absorber. For this reason, a very thin CdS layer with a band gap of 2.4 eV is used between the ZnO and the absorber layer, and it is usually prepared with the chemical-bath deposition method. Using a buffer layer, we achieve a better band gap adjustment between the window and absorber layer.

1. Ga Content

It has already been discussed that the efficiency of a solar cell is determined by recording the I–V curve of the cell. Along with the open-circuit voltage, the short-circuit current and the fill factor constitute the quality factors of the cell. An increase of the band gap of the absorber, thus increasing the Ga content $x = Ga/(In + Ga)$, leads to a proportional increase of V_{OC}. The band gap increase results in an increase of the band bending and an increase in the open-circuit voltage and creates a larger fill factor with fewer cells required per PV array. The frequency response of a CIGS cell for variations in Ga composition is shown in Figure 22. The consequent reduction in performance with an increased Ga ratio may be justified by the fact that the wider the band gap of the absorber, the lower the contribution of photons, which penetrate deeper, to photocurrent generation.

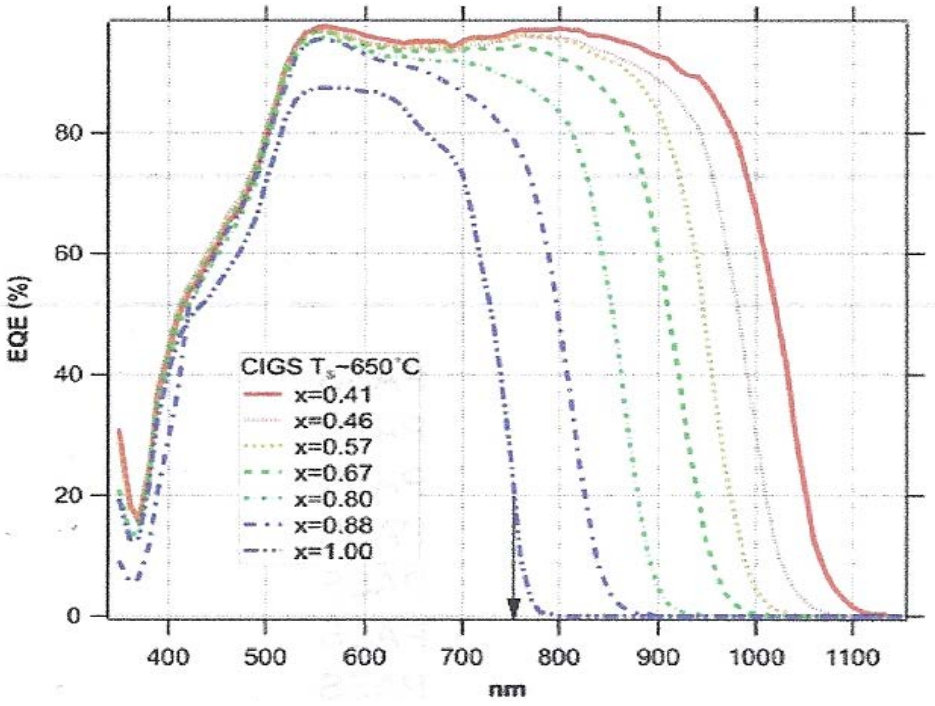

Figure 22. CIGS frequency response for different Ga content. From [31]

A photocurrent decrease is observed despite the voltage increase because a material absorbs photons of energy greater than the band gap energy of the material, and

a band gap increase results in fewer photons' absorption. Different researches have shown the relationship that governs the band gap and the value x of Ga composition. CIGS band gap dependence on Ga content has been found empirically to be [32]

$$E_g = 1.010 + 0.626x - 0.167x(1-x) \ . \tag{4.1}$$

Another equation describing the band gap and CIGS composition relationship, using optical absorption measurements, is given by [33]

$$E_g = 1.011 + 0.664x - 0.249x(1-x) \ . \tag{4.2}$$

The different equations arise from the different growth processes followed, such as the three stage process, thermal evaporation, electrodeposition, deposition temperatures, content, stoichiometry and composition range on CIGS, inducing in different performances of the test specimens.

Regardless of the relationship followed, studies and experiments show that despite the voltage-current trade-off, Ga addition is beneficial for cell performance and efficiency by achieving a better matching of the solar spectrum. From Figure 23 it can be seen that this trade-off, maximized for a Ga content with a value roughly 0.3, resulted in absorber energy band gap values of roughly 1.1–1.2 eV.

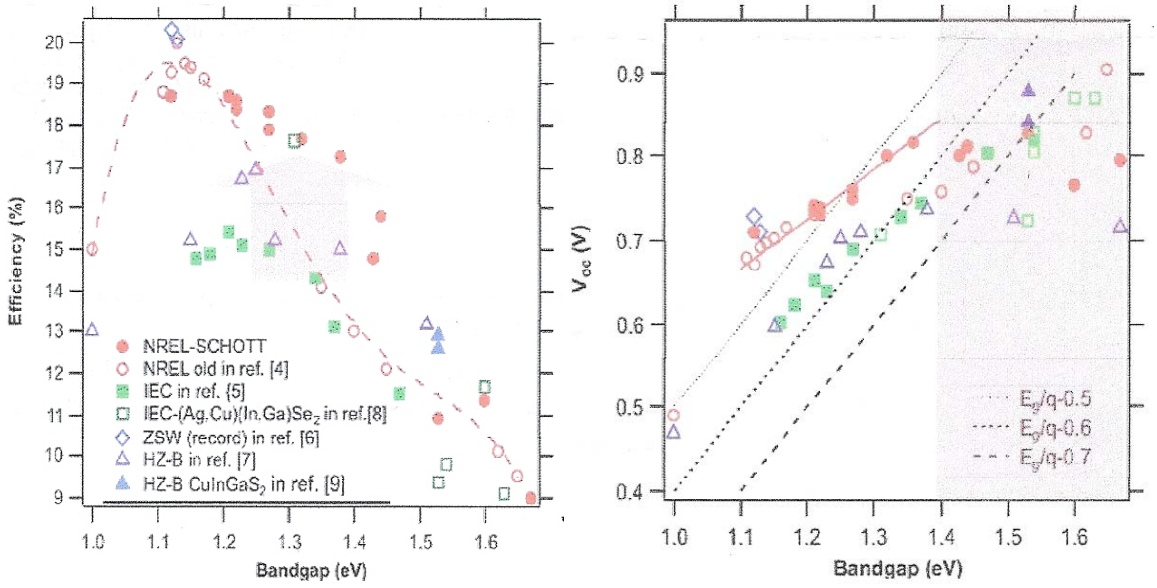

Figure 23. CIGS absorber band gap vs. solar cell efficiency and V_{OC} . From [31]

2. Band Alignment

An important parameter in a heterojunction is the pattern of alignment of valance and conduction bands on either side of the contact's layers because this has a strong influence on the current transport across the heterojunction and the performance of solar cells. Extensive research of this band's adaptation in PV cells led to the achievement of high efficiencies in cells of this type. Valance band adaptation in CIGS/CdS heterojunction is almost independent of the gallium rate content and approximately equal to one eV. In contrast, the energy difference of the conduction bands altered by Ga content variation, even changing sign, taking positive or negative values depends on the size of the absorber's band gap. Favorable alignment between the conduction bands in the CIGS/CdS interlayer, considered the one corresponding in energy difference greater than zero, is called band alignment. A visual representation of this alignment can be found in Figure 24.

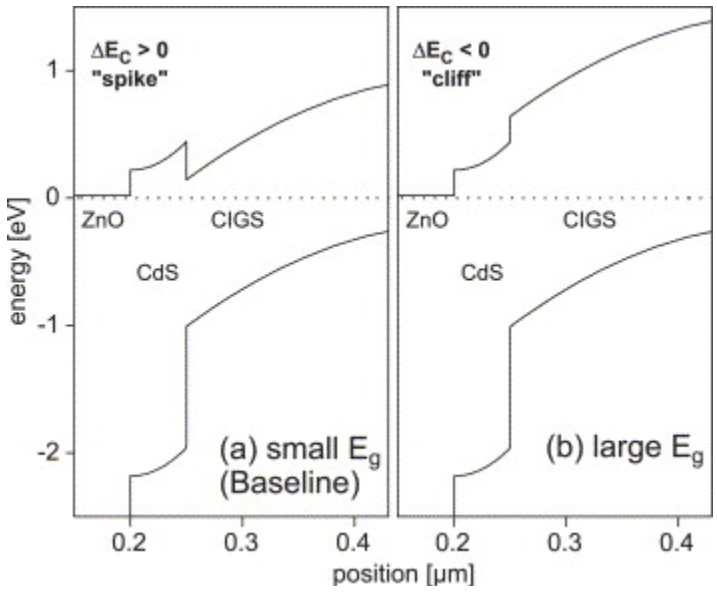

Figure 24. Conduction and valence band for a small (a) and a large (b) band gap CIGS cell. From [34]

With an increase in Ga composition ratio, the conduction bands alignment in the interlayer lead from a spike for CIGS absorbers with low band gap to a cliff for those with a large band gap. For both conduction and valance band offsets smaller than the

band gap difference, the conduction band offset is positive, a spike, and for valance band offset larger than band gap difference, the conduction band offset is negative, a cliff.

3. CIGS Absorber Thickness

One of the main goals of today's PV research and development is making the cells thinner by using less semiconductor material in order to lower production time and reduce the cost due to increased indium prices and composited elements expenses.

The thickness of a solar cell is a very important parameter, and choosing the optimal thickness is often a function of many conflicting factors. The standard thickness of the CIGS absorber layer in CIGS thin-film solar cells is presently 1.5–2μm. If this thickness could be reduced with no, or only minor, loss in performance, it would lead to even more effective PV cells and in boosting efficiencies to new record levels. Making thinner absorber layer has been associated with recombination losses due to smaller grains and larger grain boundaries. It has been also associated with high probability of back contact recombination due to carrier generation close to the back contact and increased tunneling recombination close to the interface. The question of how thin the absorber thickness should be arises. Using more material unduly increases the cost of the cell, while on the other hand, with too little, part of the important properties of these materials are lost, since, for example, less light is absorbed.

Recent efforts have focused on manufacturing increasingly thinner films without compromising performance and reducing the efficiency of the cell. Properties of these reduced thickness PV cell are grouped in Table 2.

Table 2. Properties of thin CIGS solar cells. From [35]

Thickness (μm)	V_{OC} (V)	J_{SC} (mA/cm2)	Fill factor (%)	Eff (%)
1.0 (3-stg)	0.654	31.6	78.3	16.2
1.0 (codep)	0.699	30.6	75.4	16.1
0.75 (codep)	0.652	26.0	74.0	12.5
0.5 (codep)	0.607	23.9	60.0	8.7
0.4 (3-stg)	0.565	21.3	75.7	9.1

Devices with 17.1% efficiency at 1.0 μm CIGS absorber thickness have been fabricated [36]. CIGS devices consisting of absorber layers thicknesses down to 0.8–1 μm were fabricated and shown to maintain high performances. Specifically, device results of 16.1% efficiency at 1.8 μm CIGS absorber thickness, 15.0% at 1.0 μm and 12.1% at 0.6 μm were achieved [37].

V. SILVACO ATLAS™ MODELING SOFTWARE

A. OVERVIEW

The construction of experimental specimens is the process followed by most research centers and manufacturers of PV cells. Although it is the most reliable procedure for evaluating the performance of a cell, it is still costly and time consuming. On the other hand, modeling using software provides a fast, consistent, and relatively inexpensive way to design solar cells. Modeling and simulation allowed for thousands of combinations to be investigated before the fabrication of actual examples.

The use of Silvaco ATLAS™ simulation software to model a tandem CIGS cell and evaluate the performance for different variations of cell parameters is the focus of this thesis. Design optimization was accomplished by separately altering the thickness and Ga ratio of both CIGS layers of the tandem cell.

B. SILVACO SIMULATION ENVIRONMENT

Simulation of a PV cell in ATLAS™ is made through a text input deck called DeckBuild, a run-time environment in which many different parameters of cell structure and composition must be defined.

The structure definition comprises a cornerstone for the simulation since it not only bears the physical dimensions and thicknesses of the different layers constituting the cell but also builds a mesh for the cell through its fine division. Its significance is that at the grid points, called nodes, a set of differential equations are solved with a view to simulating the transport of the cell's carriers and enabling a study of the behavior of the cell.

The composition definition it is also important since ATLAS™ is a physically-based device simulator. Once the physical structures are specified, composition and bias conditions statements lead ATLAS™ to make predictions of the electrical characteristics of the cell.

The buildup consists of a well-defined mesh on which the cell is constructed. The simulation's resolution is determined by the density of the mesh's numerous triangles and designates the time needed for program iterations and the accuracy of cell representation. This triangulate mesh is then divided into regions, and different materials are assigned in each of those regions. Then, the electrodes to obtain the electrical characteristics for the device or for any region required are assigned. Next, every defined material must be associated with a doping, and, as much as possible, material properties must be declared for the most accurate simulation. The next step for the user is to choose among different models, finding that which is most the suitable for evaluating the structure, and achieving a better outline for the specific cell simulation. A specification of a light beam illuminates the cell as in real conditions, simulating different regions of the solar spectrum, depending on the beam chosen. Also, the selection of a method, among the different offered by the ATLAS™ library, is needed for solving the differential equations through which the cell's operating characteristics arise. These characteristics from the simulation can be saved in a log file and used to create plots using TONYPLOT, the interactive graphics and analysis package included in the program. The preceding analysis of cell buildup is illustrated in Figure 25.

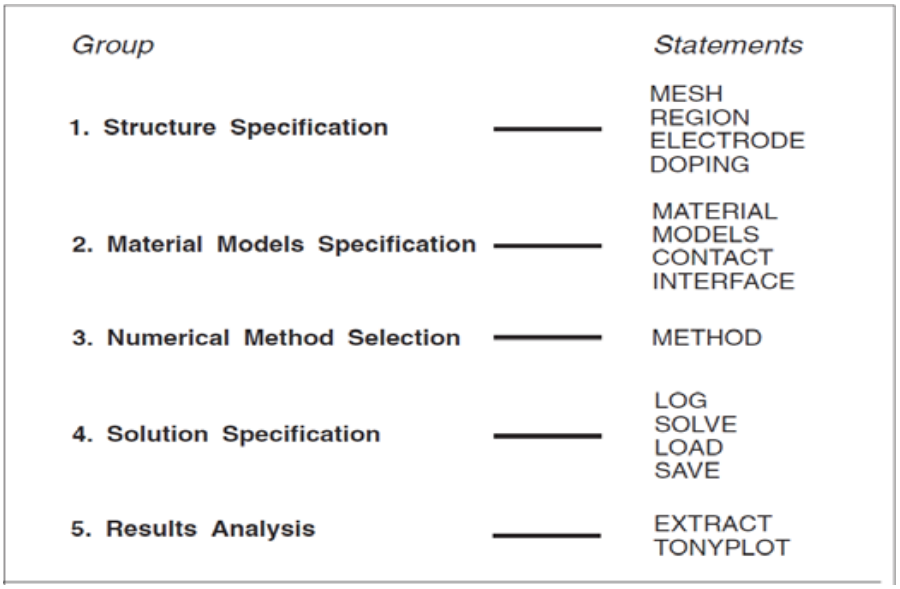

Figure 25. Command group and statements layout for a Silvaco ATLAS™ file. From [38]

C. DEVICE BASIC CONSTRUCTION LAYOUT

The first line to be read by the program when running ATLAS™ using DeckBuild is the GO ATLAS command. After that, the statements structure should be followed in the sequence depicted in Figure 25. An ATLAS™ statement is comprised of a keyword and a set of parameters, which are not case sensitive, in the following format:

<STATEMENT> <PARAMETER>=<VALUE>.

An example of the ATLAS™ syntax for defining the material properties is given by:

MATERIAL MATERIAL=CdS EG300=2.4 PERMITTIVITY=10 \
AFFINITY=3.75 MUN=10 MUP=1 NC300=2.2e18 NV300=1.8e19.

The statement is 'MATERIAL' and is used to set basic material parameters related to band structure and parameters for certain mobility, recombination, or carrier statistics models. The parameters are MATERIAL, EG300 PERMITIVITY, AFFINITY, MUN, MUP, NC, NV. There are four groups of parameters: real, integer, character, and logical. The 'MATERIAL' parameter is of type 'character', which is any character string. All the other parameters used in this example are of type 'real', meaning they must be real, not imaginary, values. Integer parameters can take on integer values, while logical parameters imply a true or false condition.

An interesting observation can be made on the use of the backslash '\' at the end of a line of code. The program is informed that the following line of code should be considered a continuation of the line of code in which this symbol has been introduced [38].

1. Mesh

The grid consists of horizontal and vertical lines with a user-defined distance between them. It bounds the physical area of the cell by creating a number of triangles in which the simulation will take place. Mesh specification also involves a tradeoff between accuracy and numerical efficiency. A fine defined mesh will lead to more accurate

results, and on the other hand, a coarse mesh that minimizes the total number of grid points will lead to a larger numerical efficiency.

The mesh is created with the following statements:

MESH SPACE.MULT=<VALUE>;

X.MESH LOCATION=<VALUE> SPACING=<VALUE>;

Y.MESH LOCATION=<VALUE> SPACING=<VALUE>.

The default value for the mesh scaling factor is one but can be changed at will. Values smaller than the default create a finer grid, containing enough points to be accurate. In contrast, larger values create a crude grid, especially in material boundaries and junctions, leading to less accurate results. Vertical and horizontal mesh division, in microns, is specified with X.MESH and Y.MESH commands and their associated spacing.

An example of both fine and coarse meshes designed in ATLAS™ is depicted in Figure 26.

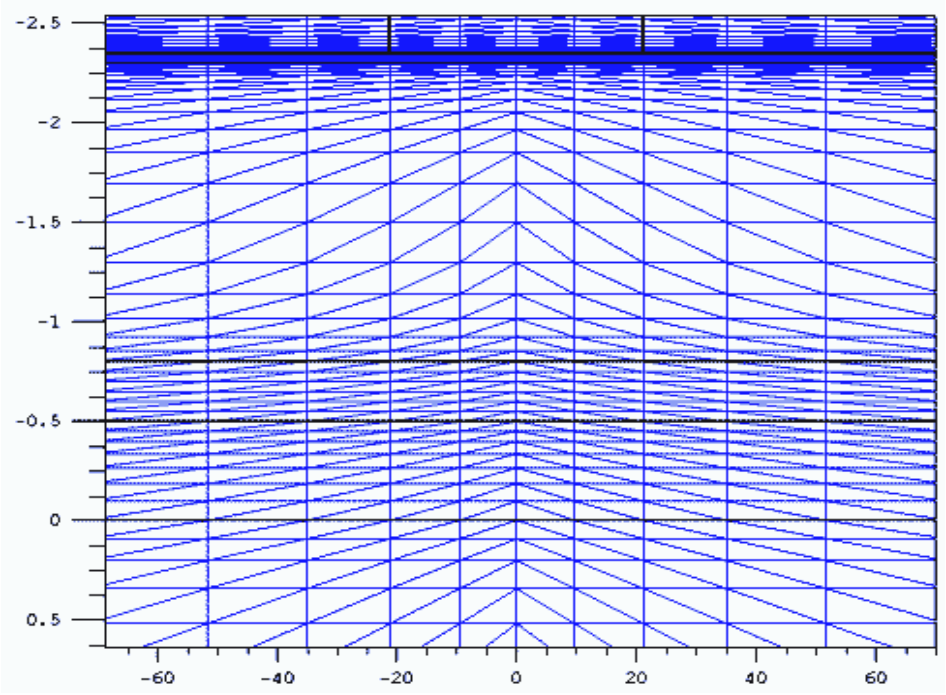

Figure 26. Typical mesh in ATLAS™.

2. Regions

In defining a region, all locations of the mesh are divided into numbered areas, where each is associated with a specific material from the ATLAS™ library. Regions are created with the following statements:

REGION number=<integer> <material type> <position>.

The number assigned to each region is representative of this area, which now can be called and stated by this number. Determining the position of each region attests that the region's limits will not exceed the limits of the grid, which are the physical bounds of the cell.

3. Electrodes

Electrodes specify the locations and names of electrodes in the previously defined mesh. This location can be any specific region, and for the purposes of this thesis, a pair of cathode, and anode electrodes was assigned in the two individual cells that form the tandem CIGS cell. The format to define the electrodes is:

ELECTRODE NAME = <electrode name> <position>.

BOTTOM and TOP statements specify that the electrode is positioned along the bottom or the top of the device, respectively. Otherwise, minimum and maximum position boundaries must be specified, using the X.MIN, X.MAX, Y.MIN, Y.MAX statements.

4. Doping

DOPING specifies doping profiles in the device structure, either analytically or from an input file. The DOPING statement is:

DOPING <distribution type> <dopant type> <position parameters>.

Uniform, Gaussian or non-standard (user defined from a custom file) distributions can be used to generate the doping profile. The type and concentration of doping must be defined next as well as the region to be doped.

5. Material

The previously defined and doped region must be associated with specific materials. These materials, their properties, and physical parameters can be selected from the ATLAS^{TM} database, among a number of elements, compounds, and alloys. The user specifies the material and its properties using the general statement form:

MATERIAL <localization> <material definition>.

A specific example used in this thesis is:

MATERIAL MATERIAL=CdS EG300=2.4 PERMITTIVITY=10 \
AFFINITY=3.75 MUN=10 MUP=1 NC300=2.2e18 NV300=1.8e19.

In this example, the material used is the CdS with band gap equal to 2.4 eV, dielectric permittivity equal to 10 F/m, and electron affinity equal to 3.75 eV. More properties include low-field electron and hole mobility, in cm^2/Vs units, equal to ten and one, respectively. Also, the conduction and valance band densities at 300 K are equal to $2.2 \cdot 10^{18}$ cm^{-3} and $1.8 \cdot 10^{19}$ cm^{-3}, respectively.

These material properties and physical parameters are defined for every region consisting of the specific material. The user can change the material properties only in a region by replacing the second MATERIAL from the above example with a REGION statement describing this specific region.

6. Models

Once we define the mesh, geometry, and doping profiles, we can modify the characteristics of electrodes, change the default material parameters, and choose which physical models ATLAS^{TM} will use during the device simulation. The physical models are grouped into five classes: mobility, recombination, carrier statistics, impact ionization, and tunneling, and details for each model are contained in the ATLAS^{TM} user manual. [38]. The general MODELS statement is:

MODELS <model name>.

Physical models can be enabled on a material-by-material basis. This is useful for heterojunction device simulation and other simulations where multiple semiconductor regions are defined and may have different characteristics.

7. Solution Method

The numerical methods to be used for solving the equations and parameters associated with these algorithms are determined by the METHOD statement. Several numerical methods are contained in the ATLAS^{TM} library, but there are three main types. The GUMMEL method is used for weakly coupled system equations, with only linear convergence. The NEWTON method is used for strongly coupled system equations, with quadratic convergence, requiring ATLAS^{TM} to spend more time solving for quantities which are essentially constant or weakly coupled. To obtain and ensure convergence, a more accurate approximation is needed from the system. Finally, the BLOCK method provides faster simulations when the NEWTON method is unable to provide a reliable solution [38].

8. Light Beam

An optical beam is modeled as a collimated source using the BEAM statement of the form:

BEAM <parameters>.

The origin of the beam is defined by parameters X.ORIGIN and Y.ORIGIN, the ANGLE parameter specifies the direction of propagation of the beam relative to the x-axis, while ANGLE=90 describes a vertical illumination from the top of the device.

The beam is automatically split into a series of rays so that the sum of the rays covers the entire width of the illumination window. When the beam is split, ATLAS^{TM} automatically resolves discontinuities along the region boundaries of the device. Rays are also split at interfaces between regions into a transmitted ray and a reflected ray [38].

For the purposes of this thesis, the source is the sun, and the AM1.5 spectrum is used to simulate the energy received by a solar cell in a terrestrial application.

9. Solution Specification

ATLAS™ can calculate DC, AC small signal, and transient solutions. Obtaining solutions is similar to setting up parametric test equipment for device tests. The user usually defines the voltages on each electrode in the device. ATLAS™ then calculates the current through each electrode and the internal quantities, such as carrier concentrations and electric fields throughout the device.

In all simulations, the device starts with zero bias on all electrodes. Solutions are obtained by stepping the biases on electrodes from this initial equilibrium condition. To obtain convergence for the equations used, the user should supply a good initial guess for the variables to be evaluated at each bias point. The ATLAS™ solver uses this initial guess and iterates to a converged solution. Solution specification can be divided up into four parts: LOG, SOLVE, LOAD, and SAVE.

Log files store the terminal characteristics calculated by ATLAS™. These are the currents and voltages for each electrode in DC simulations. For example, the statement:

LOG OUTF=<FILENAME>

is used to open a log file, and terminal characteristics from all SOLVE statements after the LOG statement are then saved to this file. Log files contain only the terminal characteristics and are typically viewed in TONYPLOT.

The SOLVE statement follows a LOG statement and instructs ATLAS™ to perform a solution for one or more specified bias points.

The LOAD and SAVE statements are used together to help create better initial guesses for bias points. The SAVE statement saves simulation results into files for visualization or for future use as an initial guess, and after that the LOAD statement loads a solution file whenever required to assist in the solution.

10. Data Extraction and Plotting

Extracting the data and plotting it is the final section of the input deck. The EXTRACT statement is provided within the DeckBuild environment. It has a flexible syntax that allows the user to extract device parameters and construct specific EXTRACT

routines. By default, EXTRACT statements work on the currently open log file, are generally case sensitive, and operate on the previous solved curve or structure file. All graphics in ATLAS™ are performed by saving a file and loading the file into TONYPLOT. The log files produced by ATLAS™ and the current-voltage cell characteristic can be plotted and observed in TONYPLOT.

D. CONCLUSION

The significance and function of Silvaco's ATLAS™ was analyzed in this section. Also presented was a quick look at the operating principle and means to input different parameters for the best possible simulation of a cell. Using the simulation capabilities of the program, we built single and tandem CIGS solar cells for the purposes of this thesis.

THIS PAGE INTENTIONALLY LEFT BLANK

VI. RESULTS OF SIMULATION

A. THE CONCEPT

The reliability and validity of simulation results must be performed by comparing these results with those obtained in experimental studies. Otherwise, obtained simulation results are undermined and called into question, and it is neither possible nor feasible to re-use them in constructing real cells. Additionally, when using real parameters in a simulation and computer modeling, it is a necessary and useful benchmark.

Naturally, competition for pioneering and innovation in specialized research areas is large. At the current status of PV technology, accessibility in all the different aspects related to the construction of real cells, from manufacturers and many research institutes, is difficult or impossible due to proprietary restrictions.

The building of solar cell device structure as simulation models for this thesis and the confirmation of the results was performed using published data from different research efforts. Numerical modeling and simulation for a variety of CIGS cell performance-based parameters, using different simulation software and analysis tools was reported in [39], [40], [41].

1. Software Validation

The different basic parameters of the CIGS cell function have identical or almost identical values in each of these researches. Those used in this thesis to simulate a CIGS cell are the relative permittivity ε_r, the electron affinity χ_e, the electron band mobility μ_n, the hole band mobility μ_p, the acceptor concentration N_A, the donor concentration N_D, the effective density of states in conduction band NC, the effective density of states in valance band NV, and the band gaps E_g and thicknesses for the ZnO and CdS layers.

The Silvaco ATLAS^{TM} software was first used to model a single CIGS cell using the aforementioned published required cell parameters. The Silvaco ATLAS^{TM} simulated

cell displayed output characteristics, which were compared to the published results from the different modeling and simulation researches.

2. Cell Optimization

After the validity of the ATLAS^{TM} code was verified, two different CIGS cell were created using the same code to be used as a tandem cell. Current matching in those cells was achieved by varying the band gap and absorber thickness of the individual cells.

The final tandem cell consisted of two separate cells, where the top cell had a small thickness and a large band gap in contrast to the bottom cell, which had a usual thickness for a CIGS cell and a band gap value close to the optimal values of best cells, as discussed in Chapter IV.

B. INITIAL CIGS CELL

The first cell modeled and simulated using Silvaco ATLAS^{TM} was a single CIGS cell. The ATLAS^{TM} code to create it can be found in Appendix A. The layers that constitute it are of the form ZnO/CdS/CIGS/Mo, and the parameters used are tabulated in Table 3.

Table 3. Base parameters for CIGS.

	ZnO	CdS	CIGS
ε_r	9	10	13.6
χ_e (eV)	4	3.75	3.89
μ_n (cm^2/Vs)	50	10	300
μ_p (cm^2/Vs)	5	1	30
N_A ($1/cm^3$)	0	0	8E+16
N_D ($1/cm^3$)	$5 \cdot 10^{17}$	$5 \cdot 10^{17}$	$5 \cdot 10^{17}$
NC ($1/cm^3$)	$2.2 \cdot 10^{18}$	$2.2 \cdot 10^{18}$	$2.2 \cdot 10^{18}$
NV ($1/cm^3$)	$1.8 \cdot 10^{19}$	$1.8 \cdot 10^{19}$	$1.8 \cdot 10^{19}$
E_g (eV)	3.3	2.4	1.2
Thickness (nm)	55	50	2000

The I–V curve and the cell's structure, obtained using ATLAS^{TM}, are shown in Figure 27 and Figure 28, respectively.

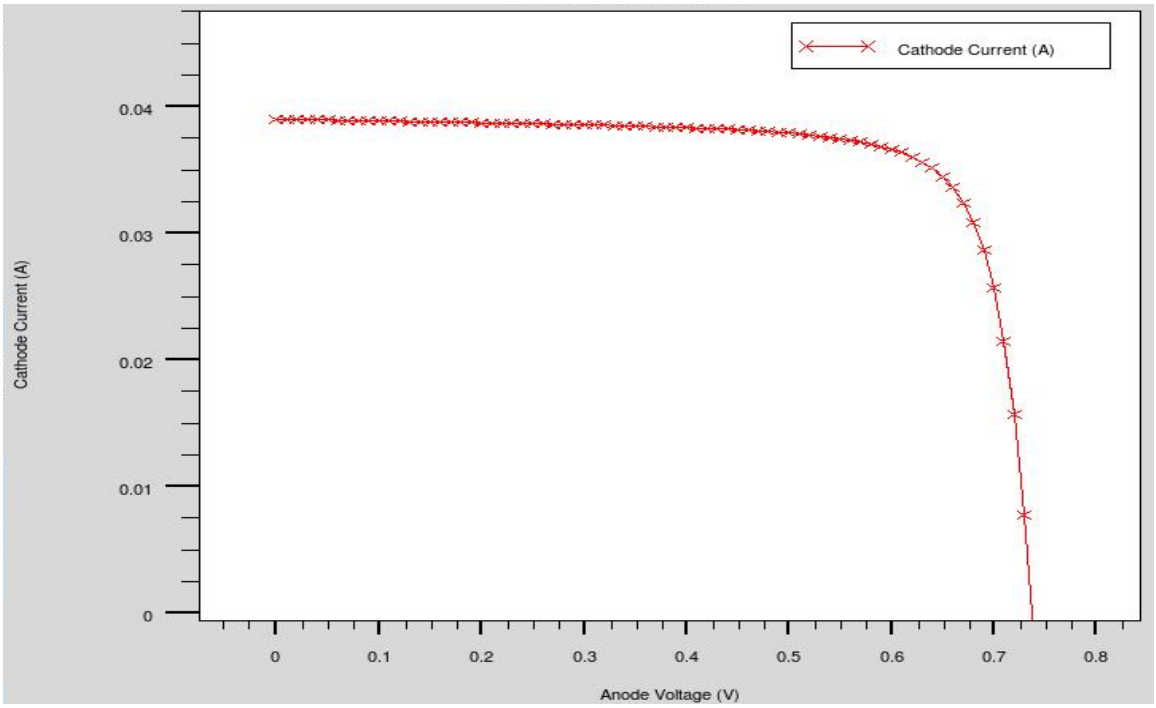

Figure 27. I–V curve for a CIGS solar cell.

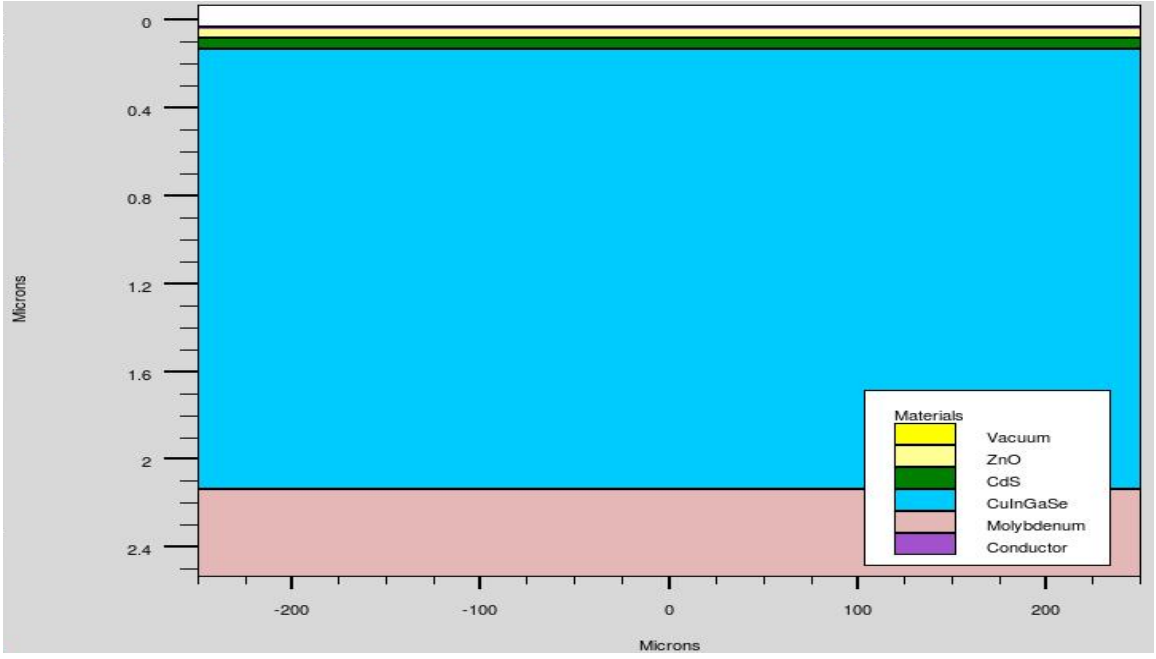

Figure 28. Silvaco ATLAS^{TM} structure file of the CIGS solar cell.

The model's performance parameters at AM1.5 and their comparison with experimental results are shown in Table 4.

Table 4. CIGS cell parameters and characteristics.

	Simulation	Experimental [24]
Absorber thickness (nm)	2000	-
$Ga/(In+Ga)$	0.3	~0.3
E_g (eV)	1.27257	1.27
V_{OC} (V)	0.737013	0.752
I_{SC} (mA/cm^2)	38.9607	31.2
FF	78.2126	77.73
Efficiency (%)	22.4584	18.3

Differences are due to different values of the base parameters, absorber thickness, and different device areas. The difference in the short-circuit current is because ATLAS^{TM} uses the whole surface of the top layer as a contact, in contrast with actual cells where a grid of contacts is used at the top of the cell, shadowing the subsequent layers. The difference in efficiencies is due to the large difference in the short-circuit current.

The voltage–current trade-off characteristic of this type of cells for different absorber-layer thicknesses can be seen in Figures 29, 30, and 31. This feature, due to variations in the $Ga/(In+Ga)$ content, results in a change in the cell's band gap. The corresponding model performance parameters and characteristics are shown in Tables 5, 6, and 7.

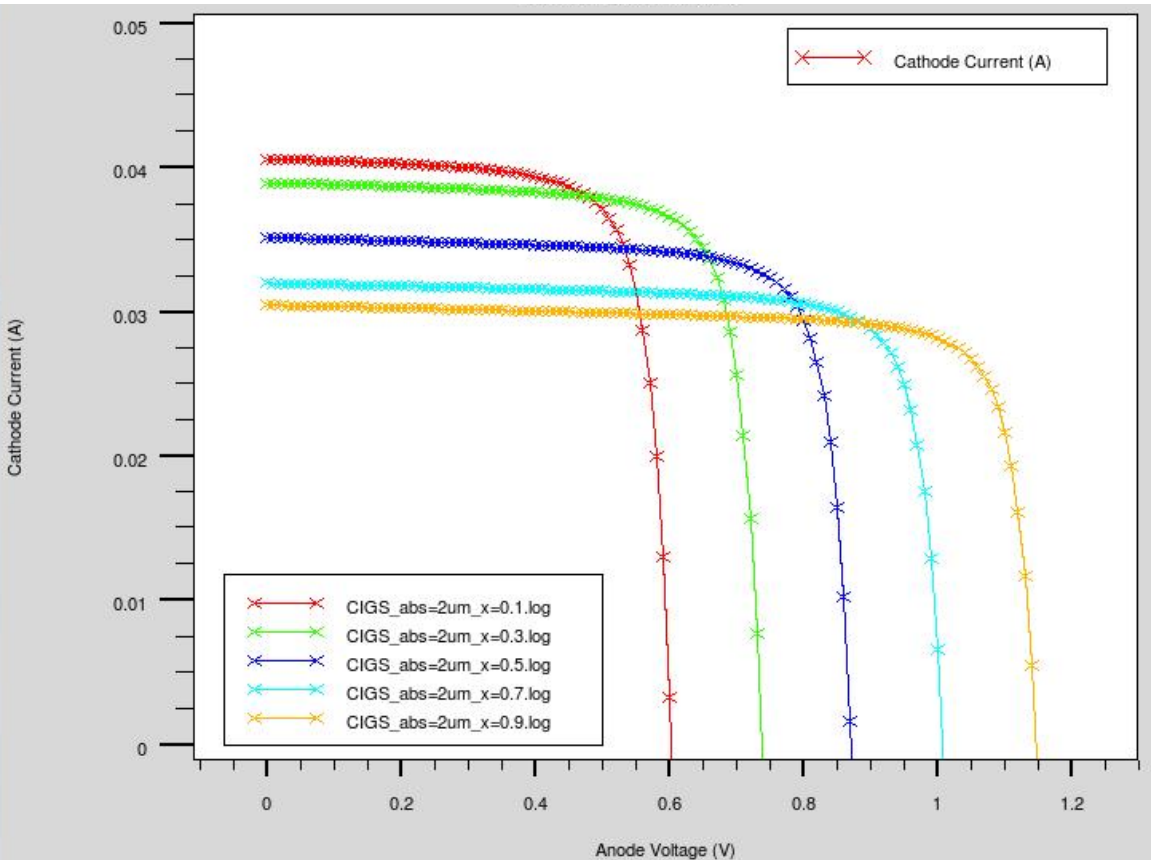

Figure 29. I–V characteristics of CIGS cells with absorber layer of 2 μm for variable CIGS band gap values.

Table 5. Characteristics of CIGS cells with absorber layer of 2 μm for variable CIGS band gap values.

	CIGS absorber=2μm				
$Ga/(In+Ga)$	0.1	0.3	0.5	0.7	0.9
V_{OC} (V)	0.602431	0.737013	0.871404	1.0075	1.14649
I_{SC} (mA/cm^2)	40.6128	38.9607	35.1504	31.9956	30.4708
FF	76.0696	78.2126	79.4624	80.4686	81.0747
Efficiency (%)	18.6115	22.4584	24.3395	25.9395	28.323

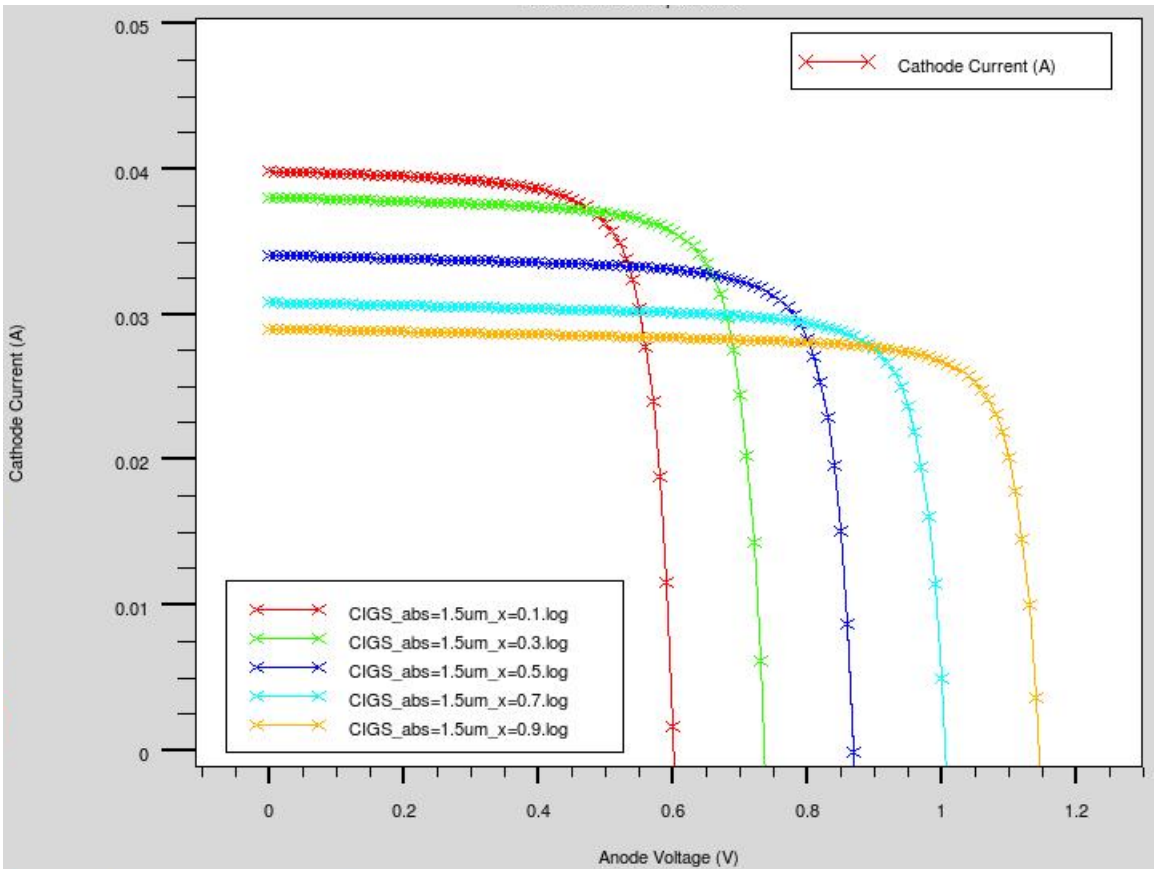

Figure 30. I–V characteristics of CIGS cells with absorber layer of 1.5 μm for variable CIGS band gap values.

Table 6. Characteristics of CIGS cells with absorber layer of 1.5 μm for variable CIGS band gap values.

	CIGS absorber=1.5μm				
$Ga/(In+Ga)$	0.1	0.3	0.5	0.7	0.9
V_{OC} (V)	0.601186	0.735435	0.869573	1.00546	1.14417
I_{SC} (mA/cm^2)	39.8573	38.0647	34.0725	30.8142	29.0136
FF	75.9943	78.1389	79.3831	80.401	80.9926
Efficiency (%)	18.2095	21.8743	23.5276	24.9102	26.8867

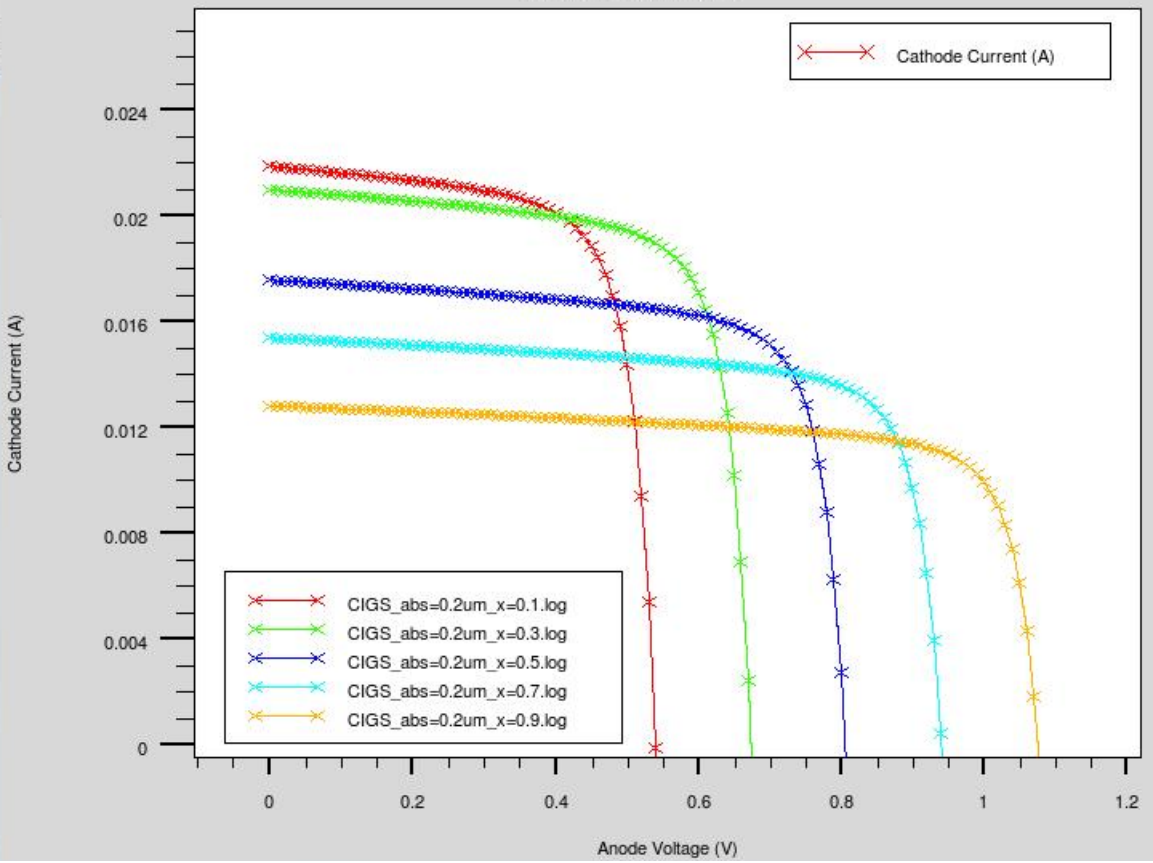

Figure 31. I–V characteristics of CIGS cells with absorber layer of 0.2 μm for variable CIGS band gap values.

Table 7. Characteristics of CIGS cells with absorber layer of 0.2 μm for variable CIGS band gap values.

	CIGS absorber=1.5μm				
$Ga/(In+Ga)$	0.1	0.3	0.5	0.7	0.9
V_{OC} (V)	0.539864	0.673892	0.805743	0.940846	1.07544
I_{SC} (mA/cm^2)	21.8576	20.9844	17.567	15.3803	12.8148
FF	71.9995	73.9936	74.8766	78.495	75.617
Efficiency (%)	8.49603	10.4636	10.5984	10.9245	10.4212

C. DUAL-JUNCTION'S INDIVIDUAL TOP LAYER

The I–V curve of the top layer of the dual-junction CIGS cell, obtained using ATLAS^{TM}, is shown in Figure 32, and the model performance parameters and characteristics are shown in Table 8.

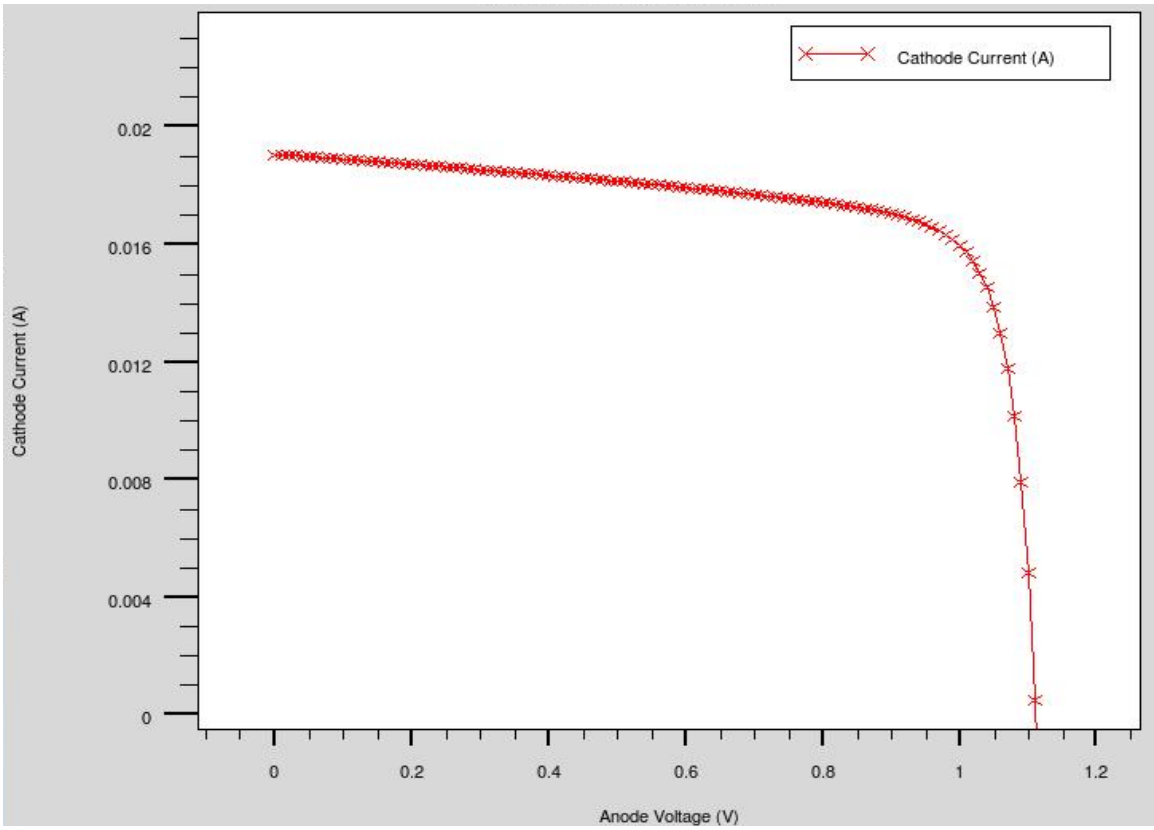

Figure 32. I–V curve of the top layer of the dual-junction CIGS cell.

Table 8. Parameters and characteristics of the top layer of the dual-junction CIGS cell.

Simulation	
Absorber thickness (nm)	180
$Ga/(In+Ga)$	0.94
E_g (eV)	1.71834
V_{OC} (V)	1.11086
I_{SC} (mA/cm^2)	19.045
FF	75.6346
Efficiency (%)	16.0015

D. DUAL-JUNCTION'S INDIVIDUAL BOTTOM LAYER

The I–V curve of the bottom layer of the dual-junction CIGS cell, obtained using ATLAS^{TM}, is shown in Figure 33, and the model performance parameters and characteristics are shown in Table 9.

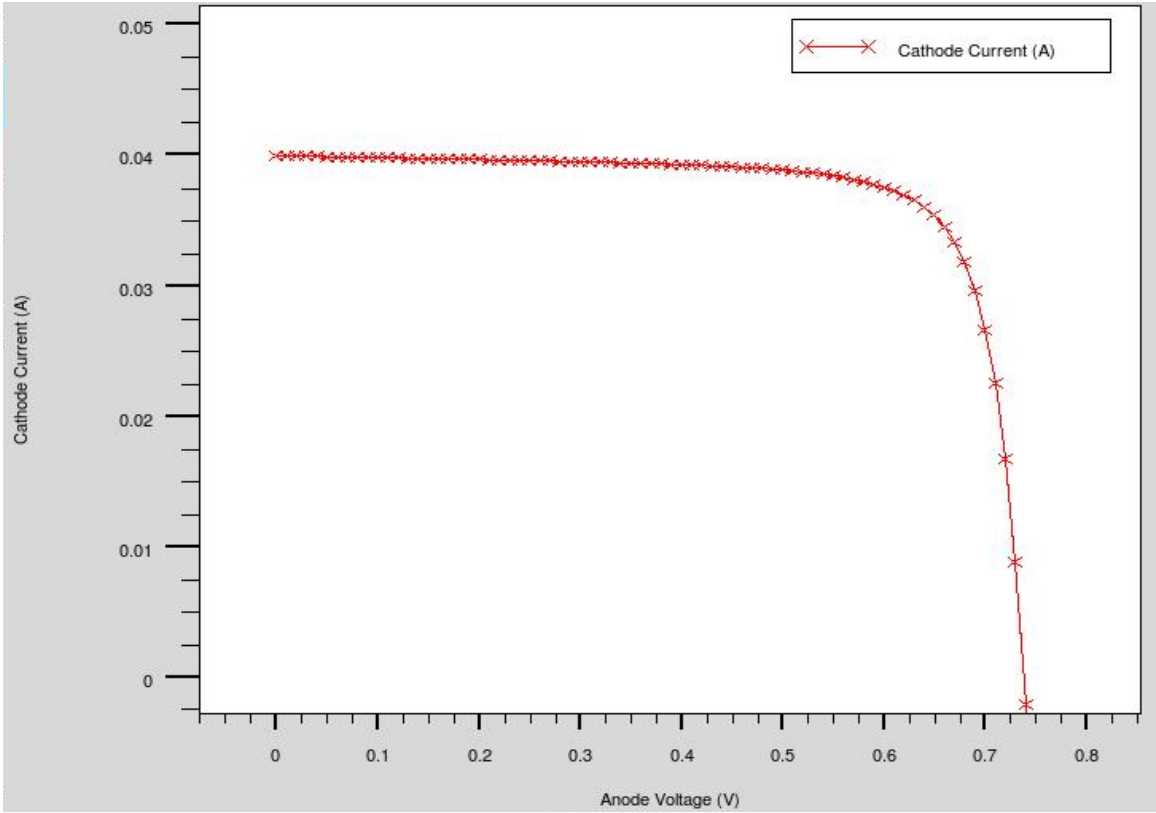

Figure 33. I–V curve of the bottom layer of the dual-junction CIGS cell.

Table 9. Parameters and characteristics of the bottom layer of the dual-junction CIGS cell.

Simulation	
Absorber thickness (nm)	4000
$Ga/(In+Ga)$	0.3
E_g (eV)	1.27257
V_{OC} (V)	0.738111
I_{SC} (mA/cm^2)	39.9168
FF	78.2462
Efficiency (%)	23.0537

E. DUAL-JUNCTION CIGS SOLAR CELL

Once the two individual cells were each built and modeled, a dual-junction CIGS cell was built. This was accomplished by starting with the layers of a CIGS cell on top and bottom. The corresponding absorber thickness and Ga content in these two cells were varied during the simulations. In order to simulate the tunnel junctions of the solar cell, a vacuum was placed between these layers. The ATLAS^{TM} structure file representation of the dual-junction cell is shown in Figure 34. Thicknesses and base parameters of the ZnO and CdS layers of the two CIGS cells were kept the same.

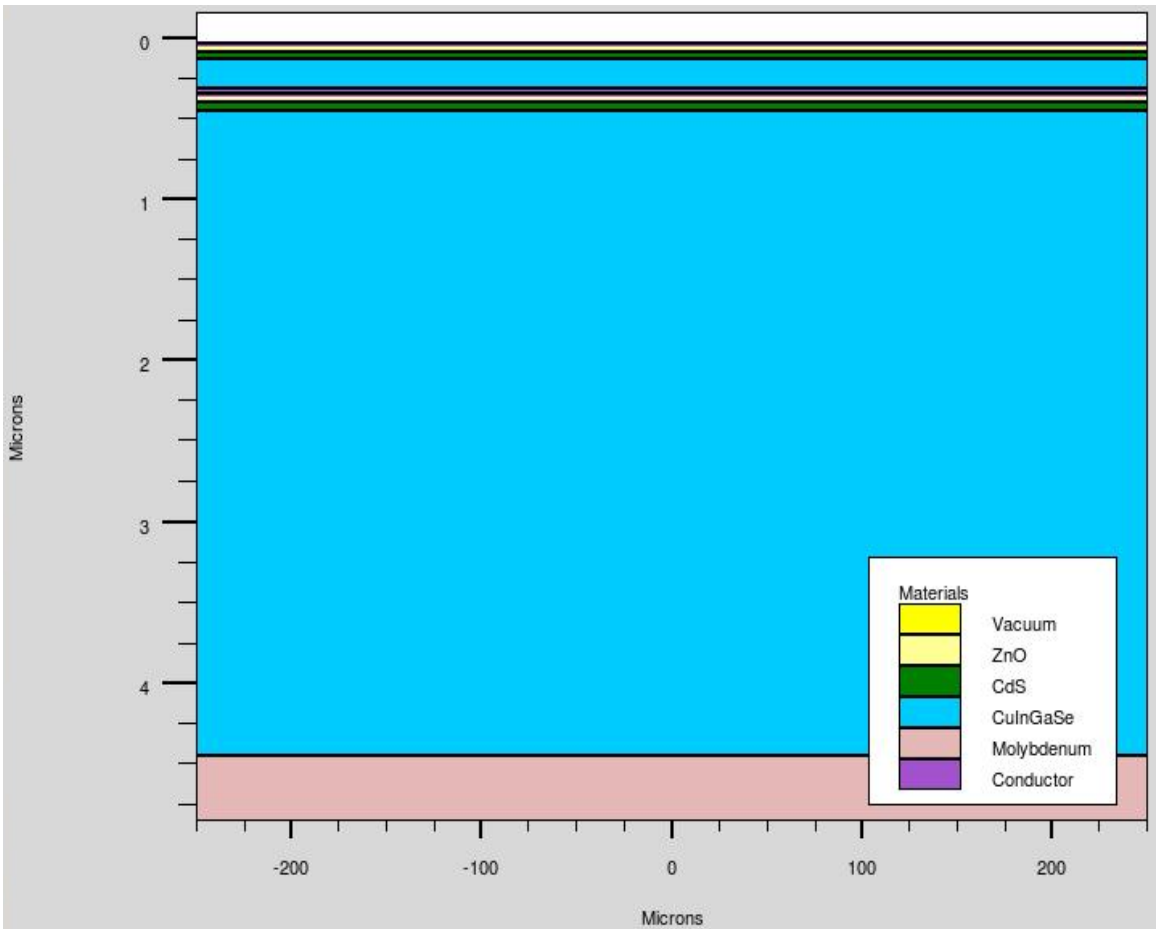

Figure 34. Silvaco ATLAS^{TM} structure file for the dual-junction CIGS cell.

In order to extract an overall I–V curve, two sets of anodes and cathodes were placed on the top, and bottom layers of the dual-junction cell and two I–V curves were

obtained. Before combining the data to achieve one overall curve, we compared the two curves to their respective individual cells to ensure that the bottom layers' I–V characteristics had degraded due to the top layer's absorbing some of the incident light. A comparison of the output of the dual-junction top layer and the individual top cell is shown in Figure 35. These two curves are identical because they have the same parameters and the same incident light shone on them. A comparison of the outputs of the dual-junction bottom layer to the individual bottom cell is found in Figure 36. In this comparison, the effect of placing a layer above it significantly reduces the characteristics of that cell; however, having this extra power absorption available is what makes the dual-junction cell more efficient than a single cell.

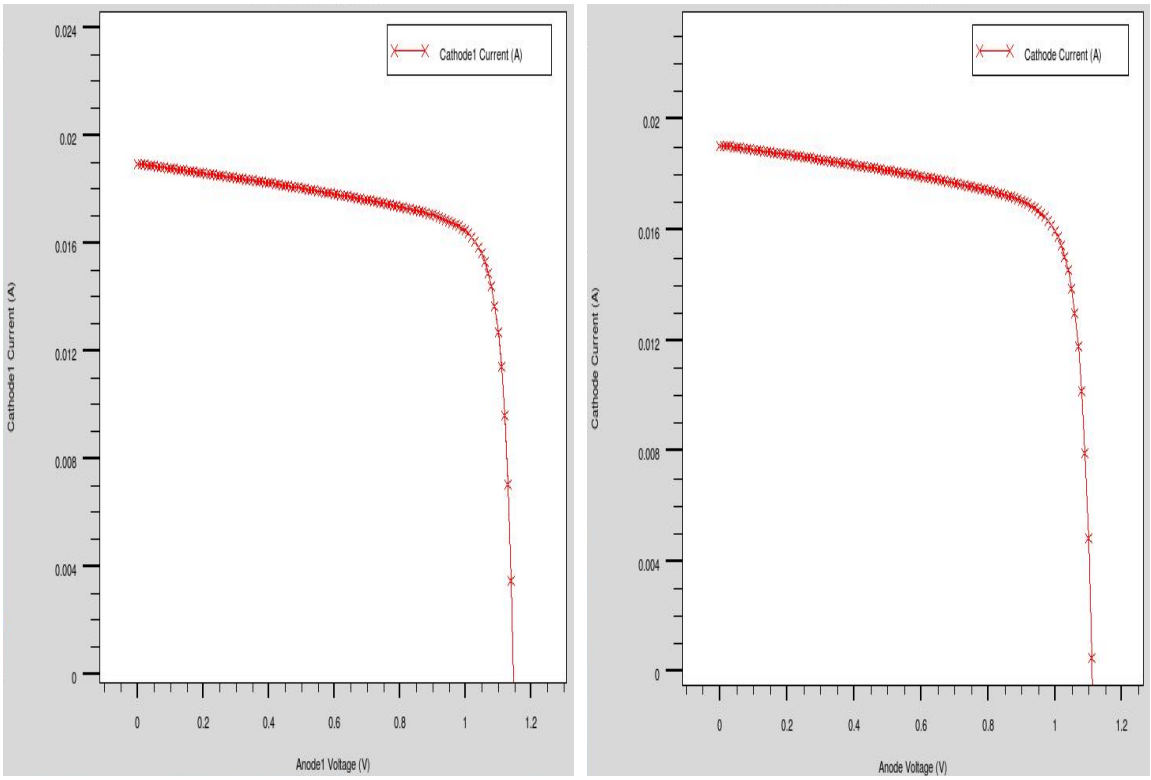

Figure 35. A comparison of the outputs of the top layer of the dual-junction and the individual top cell.

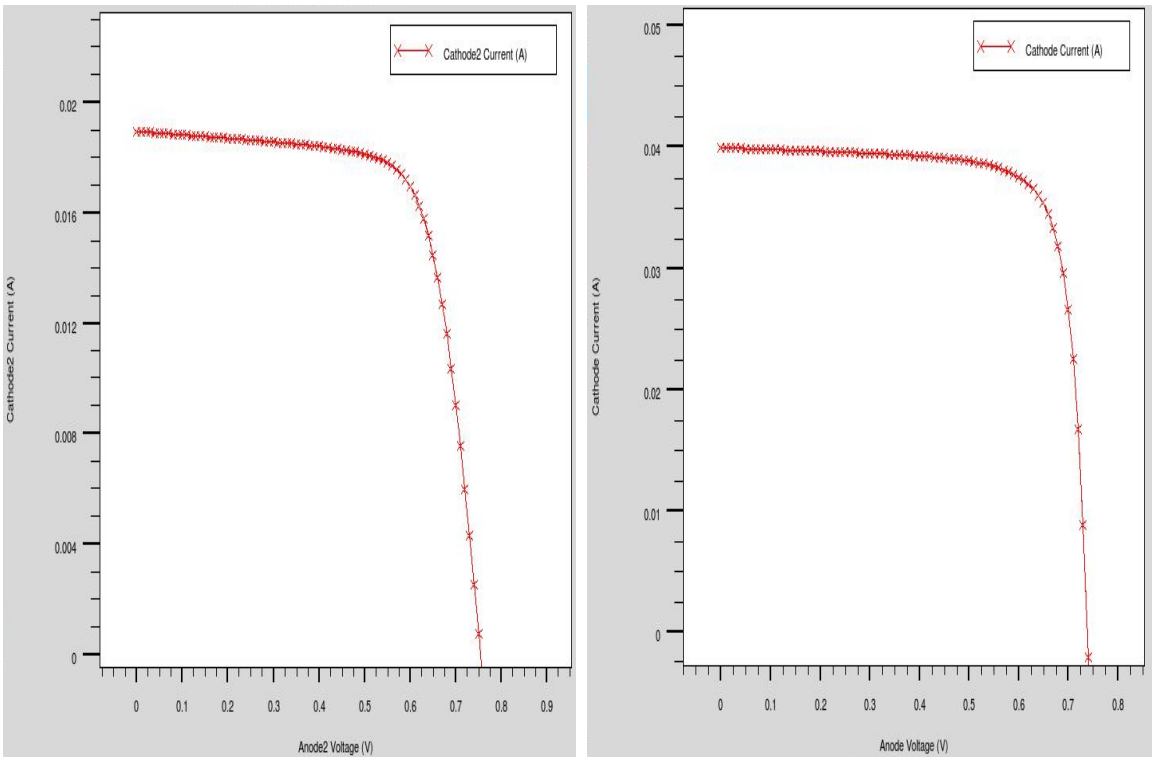

Figure 36. A comparison of the outputs of the bottom layer of the dual-junction and the individual bottom cell.

Performance parameters and characteristics of the dual-junction top and bottom cell are shown in Table 10, and an overlay plot of the I–V curves for the two layers can be seen in Figure 37.

Table 10. Parameters and characteristics of the bottom layer of the dual-junction CIGS cell.

	Dual-junction CIGS cell simulation	
	Top cell	Bottom cell
Absorber thickness (nm)	180	4000
$Ga/(In+Ga)$	0.94	0.3
E_g (eV)	1.71834	1.27257
V_{OC} (V)	1.14693	0.753904
I_{SC} (mA/cm^2)	18.9497	18.9576
FF	76.1411	71.2241
Efficiency (%)	16.5485	10.1795

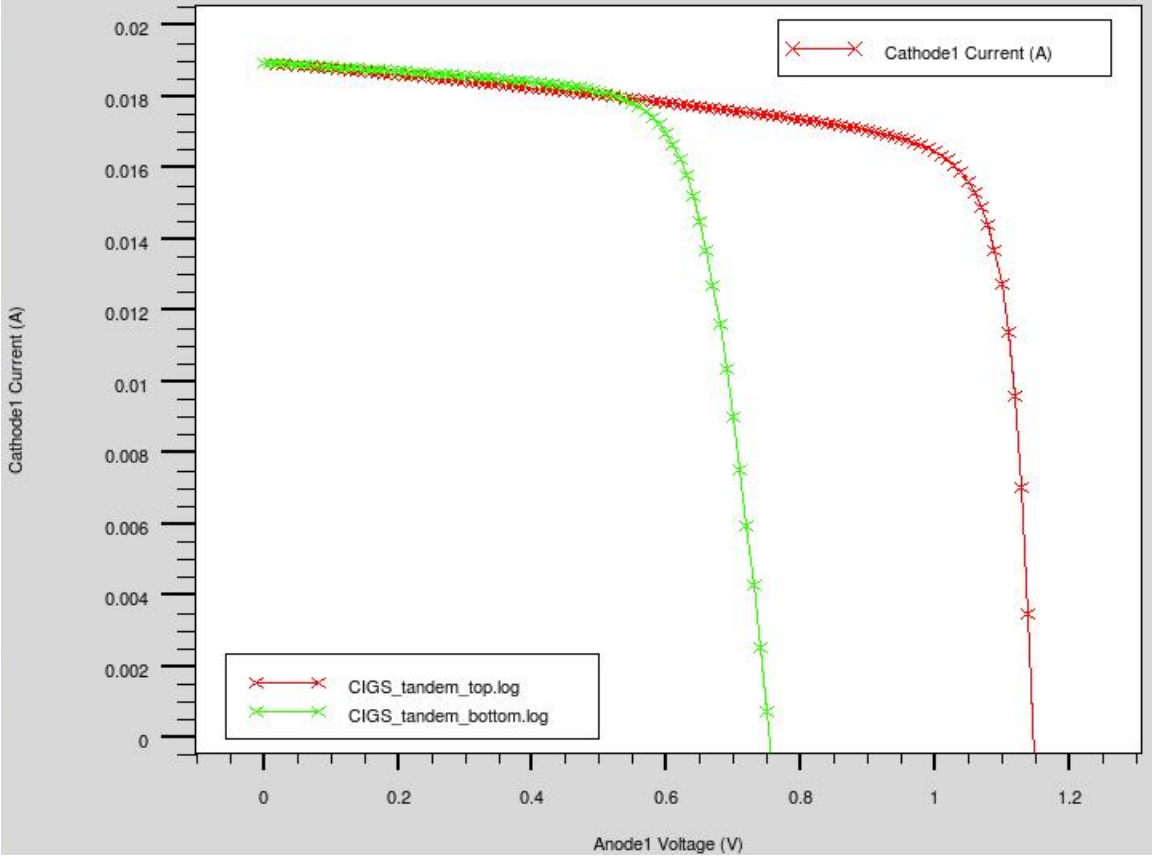

Figure 37. I–V curve overlay of the two layers.

The final performance parameters and characteristics of the model are shown in Table 11, and the final I–V curve of the dual-junction the CIGS cell, obtained using ATLAS™, is shown in Figure 38.

Table 11. Parameters and characteristics of the top layer of the dual-junction CIGS cell.

Tandem CIGS cell	
V_{OC} (V)	1.8950
I_{SC} (mA/cm^2)	18.9
FF	67.69
Efficiency (%)	24.31

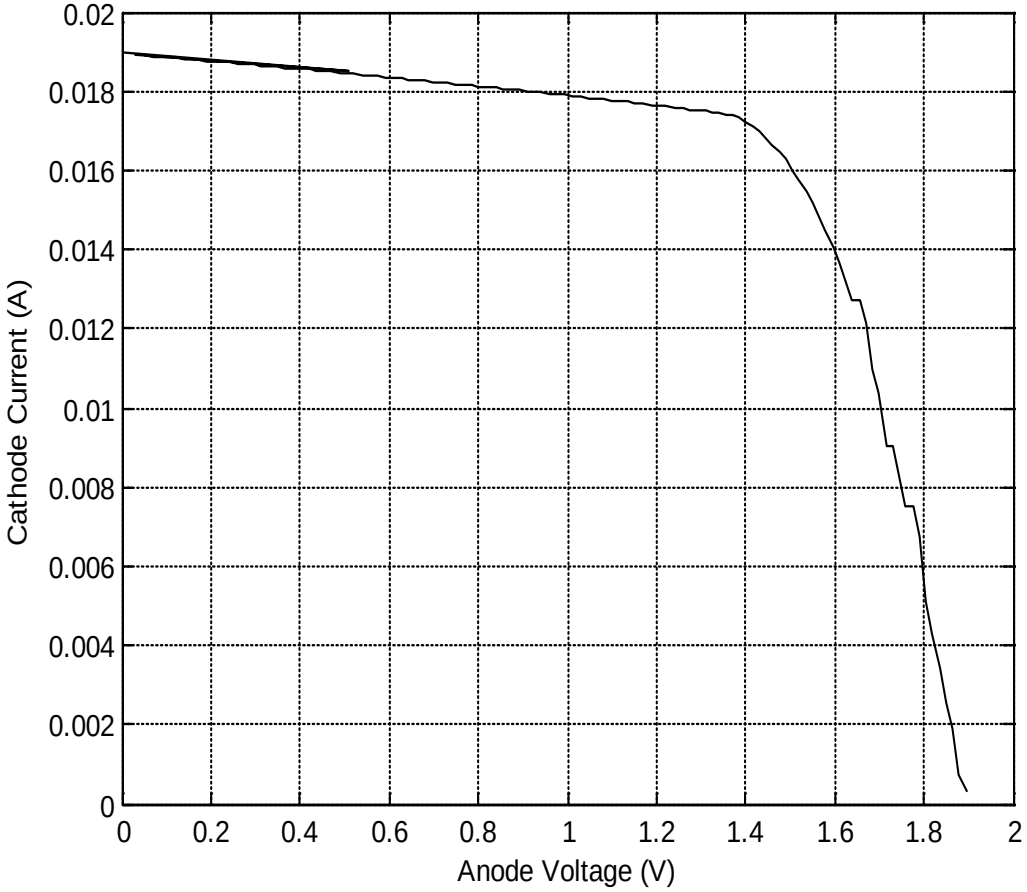

Figure 38. Final I–V curve of the tandem CIGS solar cell.

VII. CONCLUSIONS AND RECOMMENDATIONS

A. CONCLUSION

The objective of this thesis was to design a dual-junction CIGS solar cell and investigate the capabilities of this dual-junction cell in terms of PV cell electrical characteristics. That was accomplished using Silvaco ATLAS^{TM}, an advanced virtual wafer- fabrication tool. The user can enter parameters to the program using specific commands that correspond to the characteristics and properties of actual cells and simulate their operation to evaluate their potential.

First, layer thicknesses, Ga ratios, doping levels and materials properties of actual CIGS cell documented in different papers were used to create a Silvaco ATLAS^{TM} model of a single CIGS cell. Changes made to the composition ratio $Ga/(In+Ga)$ were aimed at validating the voltage–current trade-off principle in these cells.

This cell showed quite satisfactory functional behavior, and the code for its construction was used, and properly changed, to simulate two different CIGS cells. These modifications were made to the thickness and Ga content in order to achieve those characteristics that would allow their use as a dual-junction PV cell and, more specifically, to be able to respond to specific wavelengths of the solar spectrum.

After the individual CIGS solar cells were built and the current matching between them was confirmed and tested, a dual-junction cell was created by adding the layers of these two CIGS solar cells. The overall efficiency of this device was found to be 24.3%. This confirms that the same CIGS cell can be used to construct a dual-junction CIGS cell by exploiting the characteristics attributed to the change in thickness and $Ga/(In+Ga)$ composition.

This effective response of the dual-junction CIGS cell in different wavelengths confirms the promising use of CIGS cells in constructing a triple-junction CIGS cell and subsequent utilization of the whole solar spectrum, resulting in efficiencies that can

compete with, and even surpass, those of existing triple-junction cells. Moreover, this research affirms the use of Silvaco ATLAS™ as reliable program for numerical modeling, even for ultra-thin CIGS cells.

B. RECOMMENDATIONS FOR FUTURE STUDY

1. Tunnel Junction

New junctions could be created between cells that are simply connecting. Those junctions could be reverse-biased, and their depletion-region electrostatic field would oppose the flow of carriers towards the contacts. To contact current in a desirable way, the use of a proper heavily doped tunnel junction is compulsory. Their beneficial use has already been verified for different dual and triple-junction cells, but it remains to be validated for CIGS cells.

2. Triple Junction

For this type of cell to predominate and become competitive in the PV market, the construction of a triple-junction CIGS cell is imperative. Proper and careful selection of absorber thickness and Ga composition to tune up and exploit the entire solar spectrum with the construction of a triple-junction cell will boost their efficiencies to record levels.

3. Radiation Effects

For the purpose of this thesis, the performance of CIGS cells was studied using the AM1.5 spectrum to simulate the energy received by a PV cell for terrestrial application. The effectiveness and robustness of these cells enables their use in space applications. Therefore, before their selection, the effects of radiation under such use should be studied thoroughly.

4. Model Improvement

The use of CIGS cells has recently begun, and the study of experimental and actual specimens brings to light more data for their behavior, contributing to a better understanding of their properties. One area in which several research efforts are focusing is the study and better understanding of grain boundaries and hetero-junction behavior.

An introduction into ATLAS™ of more cell features and operating parameters, and the creation of a more accurate and sophisticated model, will improve existing results.

5. Real Data

This thesis lacked the data for an actual dual-junction CIGS cell. The best and most accurate verification of the results will be to obtain parameters used in real cells and data measured for these cells. This comparison of experimental and simulated results will lead to more accurate and confident results for new cell designs and performance.

THIS PAGE INTENTIONALLY LEFT BLANK

APPENDIX A. ATLAS SOURCE CODE

A. INITIAL CIGS CELL

```
### CIGS single ###
go atlas
# Definision of constants
set Vacuum_thk=0.03
set ZnO_thk=0.055
set CdS_thk=0.05
set CIGS_thk=2
set Mo_thk=0.04
set x_comp=0.3
set kelvin=318

# Bandgap of CIGS
mesh
x.mesh location=-0.1 spacing=0.01
x.mesh location=0    spacing=0.01
x.mesh location=0.1  spacing=0.01
y.mesh location=-0.1 spacing=0.01
y.mesh location=0    spacing=0.01
y.mesh location=0.1  spacing=0.01
region number=1 material=CIGS x.comp=$x_comp
electrode number=1 name=cathode top
electrode number=2 name=anode   bottom
doping p.type conc=8e16 uniform
models srh
output band.param
method climit=1e-4
solve init
solve previous
save outfile=bandgap.str
extract init infile="bandgap.str"
extract name="bandgap" 2d.max.conc impurity="Eg" material="CuInGaSe"
extract name="max_lambda" 1.23984/$bandgap
log off


go atlas
# Define the X-mesh.
```

```
mesh width=200000
# X-mesh: surface=500um2=1/200000 cm2
x.mesh loc=-250 spac=50
x.mesh loc=0    spac=10
x.mesh loc=250  spac=50

# Define the Y-mesh
# Vacuum (0.05um)
y.mesh loc=$Vacuum_thk spac=0.003
# Zno (0.055um)
y.mesh loc=$Vacuum_thk+$ZnO_thk spac=0.03
# CdS (0.05um)
y.mesh loc=$Vacuum_thk+$ZnO_thk+$CdS_thk spac=0.003
# CIGS (2um)
y.mesh loc=$Vacuum_thk+$ZnO_thk+$CdS_thk+$CIGS_thk spac=0.03
# Molibdinum (0.4um)
y.mesh loc=$Vacuum_thk+$ZnO_thk+$CdS_thk+$CIGS_thk+$Mo_thk spac=0.03

## REGIONS ##
# Vacuum (0.05um)
region num=1 material=Vacuum x.min=-250 x.max=250 y.min=0
y.max=$Vacuum_thk
# Zno (0.055um)
region num=2 material=ZnO x.min=-250 x.max=250 y.min=$Vacuum_thk \
                          y.max=$Vacuum_thk+$ZnO_thk conductor
# CdS (0.05um)
region num=3 material=CdS x.min=-250 x.max=250 \
                          y.min=$Vacuum_thk+$ZnO_thk
y.max=$Vacuum_thk+$ZnO_thk+$CdS_thk
# CIGS (2um)
region num=4 material=CIGS x.min=-250 x.max=250 \
       y.min=$Vacuum_thk+$ZnO_thk+$CdS_thk
y.max=$Vacuum_thk+$ZnO_thk+$CdS_thk+$CIGS_thk x.comp=$x_comp
# Molibdinum (0.4um)
region num=5 material=Molibdinum x.min=-250 x.max=250 \
       y.min=$Vacuum_thk+$ZnO_thk+$CdS_thk+$CIGS_thk
y.max=$Vacuum_thk+$ZnO_thk+$CdS_thk+$CIGS_thk+$Mo_thk  conductor

## ELECTRODES ##
electrode name=cathode top
electrode name=anode bottom
```

```
## DOPING ##
# Zno (0.055um)
#doping uniform region=2 n.type conc=5e17
# CdS (0.05um)
doping uniform region=3 n.type conc=1e17
# CIGS (2um)
doping uniform region=4 p.type conc=8e16

## MATERIAL PROPERTIES ##
material TAUN=1e-7 TAUP=1e-7 COPT=1.5e-10 AUGN=8.3e-32 AUGP=1.8e-31
# Vacuum
material material=Vacuum real.index=3.3 imag.index=0
# ZnO
material mat=ZnO EG300=3.3 PERMITTIVITY=9 AFFINITY=4 MUN=50 MUP=5 \
          NC300=2.2e18 NV300=1.8e19 resistivity=480
#material mat=ZnO sopra=Ito2.nk
# Cds
material mat=CdS EG300=2.4 PERMITTIVITY=10 AFFINITY=3.75 MUN=10 MUP=1 \
          NC300=2.2e18 NV300=1.8e19
material material=CdS indx.real=solarex05_0.n indx.imag=solarex05_0.k
out.index=solarex05_0
#material mat=CdS index.file=solarex10.nk
# CIGS
material mat=CIGS PERMITTIVITY=13.6 AFFINITY=3.89 MUN=300 MUP=30 \
          NC300=2.2e18 NV300=1.8e19
#material material=CIGS indx.real=solarex05_1.n indx.imag=solarex05_1.k
out.index=solarex05_1
# Molibdinum
material mat=Molibdinum resistivity=120

trap material=CIGS donor e.level=($bandgap)/2 sign=5e-13 sigp=1e-15
density=1e14 \
     y.max=$Vacuum_thk+$ZnO_thk+$CdS_thk+$CIGS_thk-0.03 degen.fac=1
trap material=CdS acceptor e.level=1.2 sign=1e-17 sigp=1e-12 density=1e18 \
     y.min=$Vacuum_thk+$ZnO_thk+0.03 degen.fac=1

## MODELS ##
models srh temperature=318 bound.trap print
#models BBT.KL
output opt.intens band.param con.band val.band
```

```
## LIGHT BEAMS ##
beam num=1 x.origin=0 y.origin=-5 angle=90 am1.5 wavel.start=0.27
wavel.end=1.65 wavel.num=50

## PLOTS
# Plot structure
struct outfile=CIGS_initial.str
tonyplot CIGS_initial.str -set str.set

## SOLVING I-V CURVE ##
solve init
solve previous
solve b1=1
log outfile=CIGS_initial.log
solve previous

extract name="Short Circuit Current" max(i."cathode")
solve vstep=0.01 vfinal=9 name=anode \
      compliance=$"Short Circuit Current" cname=anode

tonyplot CIGS_initial.log -set IV.set
extract name="Open Circuit Voltage" x.val from curve (v."anode," i."cathode") \
        where y.val=0
extract name="Max Power Current" \
        x.val from curve(i."cathode,"((v."anode")*(i."cathode"))) \
        where y.val=max((i."cathode")*(v."anode"))
extract name="Max Power Voltage" \
        x.val from curve(v."anode,"((v."anode")*(i."cathode"))) \
        where y.val=max((i."cathode")*(v."anode"))
extract name="Max Power" max((i."cathode")*(v."anode"))
extract name="FF1" $"Max Power"/($"Short Circuit Current"*$"Open Circuit
Voltage")
extract name="Eff1" $"Max Power"/0.100
```

B. DUAL–JUNCTION'S INDIVIDUAL TOP LAYER

```
### CIGS single ###
go atlas
# Definision of constants
set Vacuum_thk=0.03
set ZnO_thk=0.055
```

```
set CdS_thk=0.05
set CIGS_thk=0.18
set Mo_thk=0.04
set x_comp=0.94
set kelvin=318

# Bandgap of CIGS
mesh
x.mesh location=-0.1 spacing=0.01
x.mesh location=0    spacing=0.01
x.mesh location=0.1  spacing=0.01
y.mesh location=-0.1 spacing=0.01
y.mesh location=0    spacing=0.01
y.mesh location=0.1  spacing=0.01
region number=1 material=CIGS x.comp=$x_comp
electrode number=1 name=cathode top
electrode number=2 name=anode   bottom
doping p.type conc=8e16 uniform
models srh
output band.param
method climit=1e-4
solve init
solve previous
save outfile=bandgap.str
extract init infile="bandgap.str"
extract name="bandgap" 2d.max.conc impurity="Eg" material="CuInGaSe"
extract name="max_lambda" 1.23984/$bandgap
log off


go atlas
# Define the X-mesh.
mesh width=200000
# X-mesh: surface=500um2=1/200000 cm2
x.mesh loc=-250 spac=50
x.mesh loc=0    spac=10
x.mesh loc=250  spac=50

# Define the Y-mesh
# Vacuum (0.05um)
y.mesh loc=$Vacuum_thk spac=0.003
# Zno (0.055um)
```

```
y.mesh loc=$Vacuum_thk+$ZnO_thk spac=0.03
# CdS (0.05um)
y.mesh loc=$Vacuum_thk+$ZnO_thk+$CdS_thk spac=0.003
# CIGS (0.18um)
y.mesh loc=$Vacuum_thk+$ZnO_thk+$CdS_thk+$CIGS_thk spac=0.03
# Molibdinum (0.4um)
y.mesh loc=$Vacuum_thk+$ZnO_thk+$CdS_thk+$CIGS_thk+$Mo_thk spac=0.03

## REGIONS ##
# Vacuum (0.05um)
region num=1 material=Vacuum x.min=-250 x.max=250 y.min=0
y.max=$Vacuum_thk
# Zno (0.055um)
region num=2 material=ZnO x.min=-250 x.max=250 y.min=$Vacuum_thk \
                          y.max=$Vacuum_thk+$ZnO_thk conductor
# CdS (0.05um)
region num=3 material=CdS x.min=-250 x.max=250 \
                          y.min=$Vacuum_thk+$ZnO_thk
y.max=$Vacuum_thk+$ZnO_thk+$CdS_thk
# CIGS (0.18um)
region num=4 material=CIGS x.min=-250 x.max=250 \
       y.min=$Vacuum_thk+$ZnO_thk+$CdS_thk
y.max=$Vacuum_thk+$ZnO_thk+$CdS_thk+$CIGS_thk x.comp=$x_comp
# Molibdinum (0.4um)
region num=5 material=Molibdinum x.min=-250 x.max=250 \
       y.min=$Vacuum_thk+$ZnO_thk+$CdS_thk+$CIGS_thk
y.max=$Vacuum_thk+$ZnO_thk+$CdS_thk+$CIGS_thk+$Mo_thk  conductor

## ELECTRODES ##
electrode name=cathode top
electrode name=anode bottom

## DOPING ##
# Zno (0.055um)
#doping uniform region=2 n.type conc=5e17
# CdS (0.05um)
doping uniform region=3 n.type conc=1e17
# CIGS (2um)
doping uniform region=4 p.type conc=8e16

## MATERIAL PROPERTIES ##
```

```
material TAUN=1e-7 TAUP=1e-7 COPT=1.5e-10 AUGN=8.3e-32 AUGP=1.8e-31
# Vacuum
material material=Vacuum real.index=3.3 imag.index=0
# ZnO
material mat=ZnO EG300=3.3 PERMITTIVITY=9 AFFINITY=4 MUN=50 MUP=5 \
          NC300=2.2e18 NV300=1.8e19 resistivity=480
#material mat=ZnO sopra=Ito2.nk
# Cds
material mat=CdS EG300=2.4 PERMITTIVITY=10 AFFINITY=3.75 MUN=10 MUP=1 \
          NC300=2.2e18 NV300=1.8e19
material material=CdS indx.real=solarex05_0.n indx.imag=solarex05_0.k
out.index=solarex05_0
#material mat=CdS index.file=solarex10.nk
# CIGS
material mat=CIGS PERMITTIVITY=13.6 AFFINITY=3.89 MUN=300 MUP=30 \
          NC300=2.2e18 NV300=1.8e19
#material material=CIGS indx.real=solarex05_1.n indx.imag=solarex05_1.k
out.index=solarex05_1
# Molibdinum
material mat=Molibdinum resistivity=120

trap material=CIGS donor e.level=($bandgap)/2 sign=5e-13 sigp=1e-15
density=1e14 \
     y.max=$Vacuum_thk+$ZnO_thk+$CdS_thk+$CIGS_thk-0.03 degen.fac=1
trap material=CdS acceptor e.level=1.2 sign=1e-17 sigp=1e-12 density=1e18 \
     y.min=$Vacuum_thk+$ZnO_thk+0.03 degen.fac=1

## MODELS ##
models srh temperature=318 bound.trap print
#models BBT.KL
output opt.intens band.param con.band val.band

## LIGHT BEAMS ##
beam num=1 x.origin=0 y.origin=-5 angle=90 am1.5 wavel.start=0.27
wavel.end=1.65 wavel.num=50

## PLOTS
# Plot structure
struct outfile=CIGS_single_top.str
tonyplot CIGS_single_top.str -set str.set
```

```
## SOLVING I-V CURVE ##
solve init
solve previous
solve b1=1
log outfile=CIGS_single_top.log
solve previous

extract name=“Short Circuit Current” max(i.”cathode”)
solve vstep=0.01 vfinal=9 name=anode \
      compliance=$”Short Circuit Current” cname=anode

tonyplot CIGS_single_top.log -set IV.set
extract name=“Open Circuit Voltage” x.val from curve (v.”anode,” i.”cathode”) \
        where y.val=0
extract name=“Max Power Current” \
        x.val from curve(i.”cathode,”((v.”anode”)*(i.”cathode”))) \
        where y.val=max((i.”cathode”)*(v.”anode”))
extract name=“Max Power Voltage” \
        x.val from curve(v.”anode,”((v.”anode”)*(i.”cathode”))) \
        where y.val=max((i.”cathode”)*(v.”anode”))
extract name=“Max Power” max((i.”cathode”)*(v.”anode”))
extract name=“FF1” $”Max Power”/($”Short Circuit Current”*$”Open Circuit
Voltage”)
extract name=“Eff1” $”Max Power”/0.100
```

C. DUAL–JUNCTION’S INDIVIDUAL BOTTOM LAYER

```
### CIGS single ###
go atlas
# Definision of constants
set Vacuum_thk=0.03
set ZnO_thk=0.055
set CdS_thk=0.05
set CIGS_thk=4
set Mo_thk=0.04
set x_comp=0.3
set kelvin=318

# Bandgap of CIGS
mesh
x.mesh location=-0.1 spacing=0.01
x.mesh location=0    spacing=0.01
```

```
x.mesh location=0.1  spacing=0.01
y.mesh location=-0.1 spacing=0.01
y.mesh location=0    spacing=0.01
y.mesh location=0.1  spacing=0.01
region number=1 material=CIGS x.comp=$x_comp
electrode number=1 name=cathode top
electrode number=2 name=anode   bottom
doping p.type conc=8e16 uniform
models srh
output band.param
method climit=1e-4
solve init
solve previous
save outfile=bandgap.str
extract init infile="bandgap.str"
extract name="bandgap" 2d.max.conc impurity="Eg" material="CuInGaSe"
extract name="max_lambda" 1.23984/$bandgap
log off


go atlas
# Define the X-mesh.
mesh width=200000
# X-mesh: surface=500um2=1/200000 cm2
x.mesh loc=-250 spac=50
x.mesh loc=0    spac=10
x.mesh loc=250  spac=50

# Define the Y-mesh
# Vacuum (0.05um)
y.mesh loc=$Vacuum_thk spac=0.003
# Zno (0.055um)
y.mesh loc=$Vacuum_thk+$ZnO_thk spac=0.03
# CdS (0.05um)
y.mesh loc=$Vacuum_thk+$ZnO_thk+$CdS_thk spac=0.003
# CIGS (4um)
y.mesh loc=$Vacuum_thk+$ZnO_thk+$CdS_thk+$CIGS_thk spac=0.03
# Molibdinum (0.4um)
y.mesh loc=$Vacuum_thk+$ZnO_thk+$CdS_thk+$CIGS_thk+$Mo_thk spac=0.03

## REGIONS ##
# Vacuum (0.05um)
```

```
region num=1 material=Vacuum x.min=-250 x.max=250 y.min=0
y.max=$Vacuum_thk
# Zno (0.055um)
region num=2 material=ZnO x.min=-250 x.max=250 y.min=$Vacuum_thk \
                          y.max=$Vacuum_thk+$ZnO_thk conductor
# CdS (0.05um)
region num=3 material=CdS x.min=-250 x.max=250 \
                          y.min=$Vacuum_thk+$ZnO_thk
y.max=$Vacuum_thk+$ZnO_thk+$CdS_thk
# CIGS (4um)
region num=4 material=CIGS x.min=-250 x.max=250 \
       y.min=$Vacuum_thk+$ZnO_thk+$CdS_thk
y.max=$Vacuum_thk+$ZnO_thk+$CdS_thk+$CIGS_thk x.comp=$x_comp
# Molibdinum (0.4um)
region num=5 material=Molibdinum x.min=-250 x.max=250 \
       y.min=$Vacuum_thk+$ZnO_thk+$CdS_thk+$CIGS_thk
y.max=$Vacuum_thk+$ZnO_thk+$CdS_thk+$CIGS_thk+$Mo_thk  conductor

## ELECTRODES ##
electrode name=cathode top
electrode name=anode bottom

## DOPING ##
# Zno (0.055um)
#doping uniform region=2 n.type conc=5e17
# CdS (0.05um)
doping uniform region=3 n.type conc=1e17
# CIGS (4um)
doping uniform region=4 p.type conc=8e16

## MATERIAL PROPERTIES ##
material TAUN=1e-7 TAUP=1e-7 COPT=1.5e-10 AUGN=8.3e-32 AUGP=1.8e-31
# Vacuum
material material=Vacuum real.index=3.3 imag.index=0
# ZnO
material mat=ZnO EG300=3.3 PERMITTIVITY=9 AFFINITY=4 MUN=50 MUP=5 \
          NC300=2.2e18 NV300=1.8e19 resistivity=480
#material mat=ZnO sopra=Ito2.nk
# Cds
material mat=CdS EG300=2.4 PERMITTIVITY=10 AFFINITY=3.75 MUN=10 MUP=1 \
          NC300=2.2e18 NV300=1.8e19
```

```
material material=CdS indx.real=solarex05_0.n indx.imag=solarex05_0.k
out.index=solarex05_0
#material mat=CdS index.file=solarex10.nk
# CIGS
material mat=CIGS PERMITTIVITY=13.6 AFFINITY=3.89 MUN=300 MUP=30 \
          NC300=2.2e18 NV300=1.8e19
#material material=CIGS indx.real=solarex05_1.n indx.imag=solarex05_1.k
out.index=solarex05_1
# Molibdinum
material mat=Molibdinum resistivity=120

trap material=CIGS donor e.level=($bandgap)/2 sign=5e-13 sigp=1e-15
density=1e14 \
     y.max=$Vacuum_thk+$ZnO_thk+$CdS_thk+$CIGS_thk-0.03 degen.fac=1
trap material=CdS acceptor e.level=1.2 sign=1e-17 sigp=1e-12 density=1e18 \
     y.min=$Vacuum_thk+$ZnO_thk+0.03 degen.fac=1

## MODELS ##
models srh temperature=318 bound.trap print
#models BBT.KL
output opt.intens band.param con.band val.band

## LIGHT BEAMS ##
beam num=1 x.origin=0 y.origin=-5 angle=90 am1.5 wavel.start=0.27
wavel.end=1.65 wavel.num=50

## PLOTS
# Plot structure
struct outfile=CIGS_single_bottom.str
tonyplot CIGS_single_bottom.str -set str.set

## SOLVING I-V CURVE ##
solve init
solve previous
solve b1=1
log outfile=CIGS_single_bottom.log
solve previous

extract name="Short Circuit Current" max(i."cathode")
solve vstep=0.01 vfinal=9 name=anode \
      compliance=$"Short Circuit Current" cname=anode
```

```
tonyplot CIGS_single_bottom.log -set IV.set
extract name=“Open Circuit Voltage” x.val from curve (v.”anode,” i.”cathode”) \
        where y.val=0
extract name=“Max Power Current” \
        x.val from curve(i.”cathode,”((v.”anode”)*(i.”cathode”))) \
        where y.val=max((i.”cathode”)*(v.”anode”))
extract name=“Max Power Voltage” \
        x.val from curve(v.”anode,”((v.”anode”)*(i.”cathode”))) \
        where y.val=max((i.”cathode”)*(v.”anode”))
extract name=“Max Power” max((i.”cathode”)*(v.”anode”))
extract name=“FF1” $”Max Power”/($”Short Circuit Current”*$”Open Circuit
Voltage”)
extract name=“Eff1” $”Max Power”/0.100
```

D. TANDEM CELL

```
### CIGS tandem ###
go atlas simflags=“-P 1”
# Top cell
set Vacuum_thk1=0.03
set ZnO_thk1=0.055
set CdS_thk1=0.05
set CIGS_thk1=0.18
set Mo_thk1=0
set x_comp1=0.94
# Bottom cell
set top_thk=$Vacuum_thk1+$ZnO_thk1+$CdS_thk1+$CIGS_thk1+$Mo_thk1
set Vacuum_thk2=0.03
set ZnO_thk2=0.055
set CdS_thk2=0.05
set CIGS_thk2=4
set Mo_thk2=0.4
set x_comp2=0.3
set kelvin=318

# Bandgap of top CIGS
mesh
x.mesh location=-0.1 spacing=0.01
x.mesh location=0    spacing=0.01
x.mesh location=0.1  spacing=0.01
y.mesh location=-0.1 spacing=0.01
```

```
y.mesh location=0    spacing=0.01
y.mesh location=0.1  spacing=0.01
region number=1 material=CIGS x.comp=$x_comp1
electrode number=1 name=cathode top
electrode number=2 name=anode bottom
doping p.type conc=8e16 uniform
models srh
output band.param
method climit=1e-4
solve init
solve previous
save outfile=bandgap1.str
extract init infile="bandgap1.str"
extract name="bandgap1" 2d.max.conc impurity="Eg" material="CuInGaSe"
extract name="max_lambda1" 1.23984/$bandgap1
log off

go atlas simflags="-P 1"
# Bandgap of bottom CIGS
mesh
x.mesh location=-0.1 spacing=0.01
x.mesh location=0    spacing=0.01
x.mesh location=0.1  spacing=0.01
y.mesh location=-0.1 spacing=0.01
y.mesh location=0    spacing=0.01
y.mesh location=0.1  spacing=0.01
region number=1 material=CIGS x.comp=$x_comp2
electrode number=1 name=cathode top
electrode number=2 name=anode bottom
doping p.type conc=8e16 uniform
models srh
output band.param
method climit=1e-4
solve init
solve previous
save outfile=bandgap2.str
extract init infile="bandgap2.str"
extract name="bandgap2" 2d.max.conc impurity="Eg" material="CuInGaSe"
extract name="max_lambda2" 1.23984/$bandgap2
log off
```

```
go atlas simflags="-P 1"
# Define the X-mesh.
mesh width=200000
# X-mesh: surface=500um2=1/200000 cm2
x.mesh loc=-250 spac=50
x.mesh loc=0    spac=10
x.mesh loc=250  spac=50

# Define the Y-mesh
# Top cell
# Vacuum (0.05um)
y.mesh loc=$Vacuum_thk1 spac=0.003
# Zno (0.055um)
y.mesh loc=$Vacuum_thk1+$ZnO_thk1 spac=0.03
# CdS (0.05um)
y.mesh loc=$Vacuum_thk1+$ZnO_thk1+$CdS_thk1 spac=0.003
# CIGS (1.5um)
y.mesh loc=$Vacuum_thk1+$ZnO_thk1+$CdS_thk1+$CIGS_thk1 spac=0.03
# Molibdinum (0.4um)
y.mesh loc=$top_thk spac=0.03

# Bottom cell
# Vacuum (0.03um)
y.mesh loc=$top_thk+$Vacuum_thk2 spac=0.03
# Zno (0.055um)
y.mesh loc=$top_thk+$Vacuum_thk2+$ZnO_thk2 spac=0.03
# CdS (0.05um)
y.mesh loc=$top_thk+$Vacuum_thk2+$ZnO_thk2+$CdS_thk2 spac=0.003
# CIGS (1.5um)
y.mesh loc=$top_thk+$Vacuum_thk2+$ZnO_thk2+$CdS_thk2+$CIGS_thk2 spac=0.03
# Molibdinum (0.4um)
y.mesh loc=$top_thk+$Vacuum_thk2+$ZnO_thk2+$CdS_thk2+$CIGS_thk2+$Mo_thk2
spac=0.03

## REGIONS ##
# Top cell
# Vacuum (0.05um)
region num=1 material=Vacuum x.min=-250 x.max=250 y.min=0 y.max=$Vacuum_thk1
# Zno (0.055um)
region num=2 material=ZnO x.min=-250 x.max=250 y.min=$Vacuum_thk1
y.max=$Vacuum_thk1+$ZnO_thk1 conductor
```

```
# CdS (0.05um)
region num=3 material=CdS x.min=-250 x.max=250 \
                          y.min=$Vacuum_thk1+$ZnO_thk1
y.max=$Vacuum_thk1+$ZnO_thk1+$CdS_thk1
# CIGS (0.18um)
region num=4 material=CIGS x.min=-250 x.max=250 \
       y.min=$Vacuum_thk1+$ZnO_thk1+$CdS_thk1
y.max=$Vacuum_thk1+$ZnO_thk1+$CdS_thk1+$CIGS_thk1 x.comp=$x_comp1
# Molibdinum (0.4um)
region num=5 material=Molibdinum x.min=-250 x.max=250 \
       y.min=$Vacuum_thk1+$ZnO_thk1+$CdS_thk1+$CIGS_thk1 y.max=$top_thk
conductor

# Bottom cell
# Vacuum (0.03um)
region num=6 material=Vacuum x.min=-250 x.max=250 y.min=$top_thk
y.max=$top_thk+$Vacuum_thk2
# Zno (0.055um)
region num=7 material=ZnO x.min=-250 x.max=250 y.min=$top_thk+$Vacuum_thk2 \
                          y.max=$top_thk+$Vacuum_thk2+$ZnO_thk2 conductor
# CdS (0.05um)
region num=8 material=CdS x.min=-250 x.max=250 \
            y.min=$top_thk+$Vacuum_thk2+$ZnO_thk2
y.max=$top_thk+$Vacuum_thk2+$ZnO_thk2+$CdS_thk2
# CIGS (4um)
region num=9 material=CIGS x.min=-250 x.max=250 \
       y.min=$top_thk+$Vacuum_thk2+$ZnO_thk2+$CdS_thk2
y.max=$top_thk+$Vacuum_thk2+$ZnO_thk2+$CdS_thk2+$CIGS_thk2 \
       x.comp=$x_comp2
# Molibdinum (0.4um)
region num=10 material=Molibdinum x.min=-250 x.max=250 \
       y.min=$top_thk+$Vacuum_thk2+$ZnO_thk2+$CdS_thk2+$CIGS_thk2
y.max=$top_thk+$Vacuum_thk2+$ZnO_thk2+$CdS_thk2+$CIGS_thk2+$Mo_thk2  conductor

## ELECTRODES ##
electrode name=cathode1 top
electrode name=anode1 x.min=-250 x.max=250 y.min=$top_thk y.max=$top_thk
electrode name=cathode2 x.min=-250 x.max=250 y.min=$top_thk+$Vacuum_thk2
y.max=$top_thk+$Vacuum_thk2
electrode name=anode2 bottom
```

```
## DOPING ##
# Zno (0.055um)
#doping uniform region=2 n.type conc=5e17
# CdS (0.05um)
doping uniform region=3 n.type conc=1e17
# CIGS (0.18um)
doping uniform region=4 p.type conc=8e16
# Zno (0.055um)
#doping uniform region=7 n.type conc=5e17
# CdS (0.05um)
doping uniform region=8 n.type conc=1e17
# CIGS (4um)
doping uniform region=9 p.type conc=8e16

## MATERIAL PROPERTIES ##
material TAUN=1e-7 TAUP=1e-7 COPT=1.5e-10 AUGN=8.3e-32 AUGP=1.8e-31
# Vacuum
material material=Vacuum real.index=3.3 imag.index=0
# ZnO
material material=ZnO EG300=3.3 PERMITTIVITY=9 AFFINITY=4 MUN=50 MUP=5 \
          NC300=2.2e18 NV300=1.8e19 resistivity=480
#material mat=ZnO sopra=Ito2.nk
# Cds
material material=CdS EG300=2.4 PERMITTIVITY=10 AFFINITY=3.75 MUN=10 MUP=1 \
          NC300=2.2e18 NV300=1.8e19
material material=CdS indx.real=solarex05_0.n indx.imag=solarex05_0.k
out.index=solarex05_0
#material material=CdS index.file=solarex10.nk

# CIGS
material material=CIGS PERMITTIVITY=13.6 AFFINITY=3.89 MUN=300 MUP=30 \
          NC300=2.2e18 NV300=1.8e19
#material material=CIGS indx.real=solarex05_1.n indx.imag=solarex05_1.k
out.index=solarex05_1
# Molibdinum
material material=Molibdinum resistivity=120

trap material=CIGS donor e.level=($bandgap1)/2 sign=5e-13 sigp=1e-15
density=1e14 \
     y.max=$Vacuum_thk1+$ZnO_thk1+$CdS_thk1+$CIGS_thk1–0.03 degen.fac=1
trap material=CdS acceptor e.level=1.2 sign=1e-17 sigp=1e-12 density=1e18 \
```

```
     y.min=$Vacuum_thk1+$ZnO_thk1+0.03 degen.fac=1

trap material=CIGS donor e.level=($bandgap2)/2 sign=5e-13 sigp=1e-15
density=1e14 \
     y.max=$top_thk+$Vacuum_thk2+$ZnO_thk2+$CdS_thk2+$CIGS_thk2–0.03
degen.fac=1
trap material=CdS acceptor e.level=1.2 sign=1e-17 sigp=1e-12 density=1e18 \
     y.min=$top_thk+$Vacuum_thk2+$ZnO_thk2+0.03 degen.fac=1

#trap region=3 acceptor e.level=1.2 sign=1e-17 sigp=1e-12 density=1e18
degen.fac=1
#trap region=4 donor e.level=($bandgap1)/2 sign=5e-13 sigp=1e-15 density=1e14
degen.fac=1
#trap region=8 acceptor e.level=1.2 sign=1e-17 sigp=1e-12 density=1e18
degen.fac=1
#trap region=9 donor e.level=($bandgap2)/2 sign=5e-13 sigp=1e-15 density=1e14
degen.fac=1

## MODELS ##
#models srh temperature=$kelvin bound.trap print
#models srh conmob fermi ni.fermi bgn optr auger print
#models BBT.KL
#models region=3 BGN SRH
#models region=4 BGN
#models region=8 BGN SRH
#models region=9 BGN
#models OPTR print
#contact name=tunnel resist=1e17
output opt.intens band.param con.band val.band photogen

## LIGHT BEAMS ##
beam num=1 x.origin=0 y.origin=-5 angle=90 am1.5 wavel.start=0.27
wavel.end=1.65 wavel.num=50

## PLOTS
# Plot structure
#solve b1=1 vanode=$”Max Power Voltage”
#save outfile=Taiwan_paper.str
#struct outfile=Taiwan_paper.str
#tonyplot Taiwan_paper.str -set str.set
save outf=CIGS_tandem.str
```

```
tonyplot CIGS_tandem.str

## SOLVING I-V CURVE ##
# Top cell
solve init
#solve previous
solve b1=1
log outfile=CIGS_tandem_top.log
solve previous

extract name="Short Circuit Current1" max(i."cathode1")
solve vstep=0.01 vfinal=9 name=anode1 \
      compliance=$"Short Circuit Current1" cname=anode1

tonyplot CIGS_tandem_top.log -set IV.set
extract name="Open Circuit Voltage1" x.val from curve (v."anode1,"
i."cathode1") \
        where y.val=0
extract name="Max Power Current1" \
        x.val from curve(i."cathode1,"((v."anode1")*(i."cathode1"))) \
        where y.val=max((i."cathode1")*(v."anode1"))
extract name="Max Power Voltage1" \
        x.val from curve(v."anode1,"((v."anode1")*(i."cathode1"))) \
        where y.val=max((i."cathode1")*(v."anode1"))
extract name="Max Power1" max((i."cathode1")*(v."anode1"))
extract name="FF1" $"Max Power1"/($"Short Circuit Current1"*$"Open Circuit
Voltage1")
extract name="Eff1" $"Max Power1"/0.100
log off

# Bottom cell
solve init
#solve previous
solve b1=1
log outfile=CIGS_tandem_bottom.log
solve previous

extract name="Short Circuit Current2" max(i."cathode2")
solve vstep=0.01 vfinal=9 name=anode2 \
      compliance=$"Short Circuit Current2" cname=anode2
```

```
tonyplot CIGS_tandem_bottom.log -set IV.set
extract name=“Open Circuit Voltage2” x.val from curve (v.”anode2,”
i.”cathode2”) \
        where y.val=0
extract name=“Max Power Current2” \
        x.val from curve(i.”cathode2,”((v.”anode2”)*(i.”cathode2”))) \
        where y.val=max((i.”cathode2”)*(v.”anode2”))
extract name=“Max Power Voltage2” \
        x.val from curve(v.”anode2,”((v.”anode2”)*(i.”cathode2”))) \
        where y.val=max((i.”cathode2”)*(v.”anode2”))
extract name=“Max Power2” max((i.”cathode2”)*(v.”anode2”))
extract name=“FF1” $”Max Power2”/($”Short Circuit Current2”*$”Open Circuit
Voltage2”)
extract name=“Eff1” $”Max Power2”/0.100
log off
```

THIS PAGE INTENTIONALLY LEFT BLANK

APPENDIX B. MATLAB SCRIPT

```
%% Prepare the Workspace
clc
load datatop.txt
data1=datatop;
load databottom.txt
data2=databottom;

%% Plain Cell
% Load in Silvaco Data
%Top of Cell
Tripletop_V=data1(:,15);
Tripletop_I=(data1(:,14));
%plot(Tripletop_V,Tripletop_I);
%Bottom of Cell
Triplebottom_V=data2(:,21);
Triplebottom_I=(data2(:,20));
%plot(Triplebottom_V,Triplebottom_I);

%% Combine Data to Create Overall I-V Curve
% Add Voltages Together
Total_V1=Tripletop_V+Triplebottom_V;
I_Matrix=[Tripletop_I,Triplebottom_I];
%Use Lowest Current
Total_I1=min(I_Matrix,[],2);
%%Plot Overall I-V Curve
plot(Total_V1,Total_I1,'k')
grid on
%set(gca,'fontsize',18,'fontweight','demi')
xlabel('Anode Voltage (V)')
ylabel('Cathode Current (A)')
%title('Overall Triple Junction Cell I-V Curve')
legend('Tandem CIGS Solar Cell I-V Curve')
hold all
%Calculate Important Characteristics
Voc=Total_V1(115)
Isc=Total_I1(1)
Pmax=max(Total_V1.*Total_I1)
FF=Pmax/(Voc*Isc)
eff=Pmax/.100
```

THIS PAGE INTENTIONALLY LEFT BLANK

LIST OF REFERENCES

[1] M. Nagaich, S. Campbell, E. Aydil, "Wide band-gap $CuIn_{1-x}Ga_xSe_2$ based chalcopyrite absorbers for tandem cell application," *37st IEEE Photovoltaic Specialists Conf.*, Seattle, WA, June 19–24, 2011.

[2] A. R. Jeong et al., "Synthesis and physical properties of $Cu(In,Ga)Se_2$ nanoparticles and $CuGaSe_2$ thin-films for tandem cell photovoltaic applications," *35th IEEE Photovoltaic Specialists Conf.*, Honolulu, HI, June 20–25, 2010.

[3] J. Song et al., "Modeling and simulation of a $CuGaSe_2/Cu(In,Ga)Se_2$ tandem solar cell," *Proc. of 3rd World Conf. on Photovoltaic Energy Conversion*, Osaka, Japan, May 18, vol. 1, pp. 555–558, 2003.

[4] Y. G. Xiao et al., "Modeling of CdZnTe nad CIGS and tandem solar cells," *35th IEEE Photovoltaic Specialists Conf.*, Honolulu, HI, June 20–25, 2010.

[5] Z. Beiley, A. Bowring, M. D. McGehee, "Modeling low-cost hybrid tandem photovoltaics with power conversion efficiencies exceeding 20%," *38th IEEE Photovoltaic Specialists Conf.*, Austin, TX, June 3–8, 2012.

[6] S. Seyrling et al., "Development of multijunction thin film solar cells," *34th IEEE Photovoltaic Specialists Conf.*, Philadelphia, PA, June 7–12, 2009.

[7] T. Nakada et al., "Chalcopyrite thin-film tandem solar cells with 1.5V open-circuit-voltage," *2006 IEEE 4th World Conf. on Photovoltaic Energy Conversion*, Waikoloa, HI, May 7–12, 2006.

[8] D. Leadley. (2010, Jul. 15). "Electronic band structure" [Online]. Available: http://www2.warwick.ac.uk/fac/sci/physics/current/postgraduate/regs/mpags/ex5/bandstructure/energy_band_gaps_in_materials.jpg.

[9] "Compound semiconductors"(n.d.). [Online]. Available: http://www-opto.e-technik.uni-ulm.de/lehre/cs/III_V_map_a.jpg.

[10] Rolf E. Hummel, *Electronic Properties of Materials*, 4th ed. NJ: Springer, pp. 457, 2011.

[11] A.Luque and S.Hegedus, *Handbook of Photovoltaic Science and Engineering*, 1st ed. NJ: Wiley, pp. 71–72, 2003.

[12] Rolf E. Hummel, *Electronic Properties of Materials*, 4th ed. NJ: Springer, pp. 63–65, 2011.

[13] A. Carpi. “Atomic Theory II” [Online]. Available: http://www.visionlearning.com/library/module_viewer.php?mid=51, 2003.

[14] “p-n junction” [Online]. Available: http://en.wikipedia.org/wiki/File:Pn-junction-equilibrium.png.

[15] B. Zeghbroech. “P-N Junctions” [Online]. Available: http://ecee.colorado.edu/~bart/book/book/chapter4/gif/fig4_2_3.gif, 2011.

[16] Technical Information Office, *Basic photovoltaic principles and methods*, NJ: Springer, pp. 14, 1982.

[17] Australian CRC for renewable energy. [Online]. Available: http://www.esdalcollege.nl/eos/vakken/na/zonnecel.htm.

[18] “Solar Cell Voltage-Current Characterization” [Online]. Available: http://www.californiascientific.com/resource/Solar%20Cell.pdf.

[19] P. Michalopoulos, “A novel approach for the development and optimization of state-of-the-art photovoltaic devices using Silvaco,” M.S. thesis, Naval Postgraduate School, Monterey, California, 2002.

[20] M. Cooke, “Lighting up CIGS PVs,” *Semiconductor today, compounds & advanced Silicon*, Vol. 3, Issue 1, pp. 56, Feb. 2008. [Online]. Available: http://www.semiconductor-today.com/features/SemiconductorToday%20-%20Lighting%20up%20CIGS%20PVs.pdf.

[21] Z.X. Ong, “Transport imaging of multi-junction and CIGS solar cell materials,” M.S. thesis, Naval Postgraduate School, Monterey, California, 2011.

[22] K. L. Chopra, P. D. Paulson, V. Dutta, “Thin Film Solar Cells: An Overview,” *Progress in Photovoltaics: Research and Applications*, Vol. 12, pp. 69–92, 2004. [Online]. Available: http://nano.teicrete.gr/Microelectronics/Thin-Film%20Solar%20Cells%20An%20Overview.pdf.

[23] A. Goetzberger, C. Hebling, H. W. Schock, “Photovoltaic materials, history, status and outlook,” *Materials Science and Engineering*, R 40, pp. 1–46, 2003. [Online]. Available: http://nano.teicrete.gr/Microelectronics/Photovoltaic%20materials,%20history,%20status%20and%20outlook.pdf.

[24] “Efficiency and band gap energy” [Online]. Available: http://www.grc.nasa.gov/WWW/RT/RT1999/images/5410hepp-f3.jpg.

[25] "Absorption coefficient" [Online]. Available: http://ars.els-cdn.com/content/image/1-s2.0-S0360319906004435-gr1.gif.

[26] U.S. Department of Energy. "2010 Solar Technologies Market Report" [Online]. Available: http://www.nrel.gov/docs/fy12osti/51847.pdf, Nov. 2011.

[27] "CIS/CGS/CIGS layers" [Online]. Available: http://www.nanocotechnologies.com/Resources/Images/5ecf8e17-beae-4c1d-b399-ff99e68037aa.jpg.

[28] A.Luque and S.Hegedus, *Handbook of Photovoltaic Science and Engineering*, 1st ed. NJ: Wiley, pp. 572, 2003.

[29] S. R. Kodigala, *Thin Films and Nanostructures: $CuIn_{(1-x)}Ga_xSe_2$ Based Thin Film Solar Cells*, Vol. 35. MA: Elsevier, pp. 561, 2010.

[30] "CIGS cell" [Online]. Available: http://ssd.phys.strath.ac.uk/images/8/81/CIGS_solar_cell.gif.

[31] M. Contreras et al., "Improved Energy Conversion Efficiency in Wide-Bandgap Cu(In,Ga)Se2 Solar Cells," *37st IEEE Photovoltaic Specialists Conf.*, Seattle, WA, June 19–24, 2011, pp. 2. [Online]. Available: http://www.nrel.gov/docs/fy11osti/50669.pdf.

[32] A.Luque and S.Hegedus, *Handbook of Photovoltaic Science and Engineering*, 1st ed. NJ: Wiley, pp. 574, 2003.

[33] D. S. Albin et al., "A study on the optical and microstructural characteristics of quaternary Cu(In,Ga)Se_2 polycrystalline thin films," *21st IEEE Photovoltaic Specialists Conf.,* , Kissimmee, FL, May 21–25, pp. 562, 1990.

[34] "Valence and conduction band for cigs " [Online]. Available: http://ars.els-cdn.com/content/image/1-s2.0-S004060900401569X-gr1.jpg.

[35] K. Ramanathan et al., "High Performance CIGS Thin Film Solar Cells: A Laboratory Perspective," *2005 DOE Solar Energy Technologies Program Review Meeting*, Denver, CO, November 7–10, 2005, [Online]. Available: http://www.nrel.gov/docs/fy06osti/38987.pdf.

[36] K. Ramanathan et al., "Processing and Properties of Sub-Micron CIGS Solar Cells," *2006 IEEE 4th World Conf. on Photovoltaic Energy Conversion*, Waikoloa, HI, May 7–12, 2006.

[37] O. Lundberg, M. Bodegard, J. Malmstrom, L. Stolt "Influence of the Cu(In,Ga)Se_2 thickness And Ga grading on solar cell performance," *Progress in*

Photovoltaics: Research and Applications, Vol. 11, Is. 2 pp. 77–88, Mar. 2003. [Online]. Available: http://nano.teicrete.gr/Microelectronics/Thin-Film%20Solar%20Cells%20An%20Overview.pdf.

[38] *ATLAS User's Manual*, vols. 1–2, software version 5.6.0.R, Silvaco International, Santa Clara, CA, 2012.

[39] M. Y. Hsieh et al., "Optimization of CdS buffer layer on the performance of copper indium gallium selenide solar cells," [Online]. Available: http://research.cgu.edu.tw/ezfiles/14/1014/img/651/1138P.pdf.

[40] N. Amin, M. Tang, K. Sopian "Numerical modeling of the copper-indium-selenium (CIS) based solar cell performance by AMPS-1D," *2007 SCOReD 54th Student Conf. on Research and Development*, Malaysia, December 11–12, 2007.

[41] F. Troni, F. Dodi, G. Sozzi, R. Menozzi, "Modeling of thin-film Cu(In,Ga)Se_2 Solar Cells," *2010 Int. Conf. on Simulation of Semiconductor Processes and Devices*, Bologna, Italy, September 6–8, 2010. [Online]. Available: http://in4.iue.tuwien.ac.at/pdfs/sispad2010/pdfs/03-A.2.pdf.

INITIAL DISTRIBUTION LIST

1. Defense Technical Information Center
   Ft. Belvoir, Virginia

2. Dudley Knox Library
   Naval Postgraduate School
   Monterey, California

3. Dr. Clark Robertson, Chairman
   Department of Electrical and Computer Engineering
   Naval Postgraduate School
   Monterey, California

4. Dr. Sherif Michael
   Department of Electrical and Computer Engineering
   Naval Postgraduate School
   Monterey, California

5. Dr. Todd Weatherford
   Department of Electrical and Computer Engineering
   Naval Postgraduate School
   Monterey, California

6. Embassy of Greece
   Office of Naval Attaché
   Washington, District of Columbia

7. LT Konstantinos Fotis
   Hellenic Navy General Staff
   Athens, Greece